DISSOLUTION KINETICS OF MONEL ALLOY 400 IN AQUEOUS SOLUTIONS

By

JOSEPH ABUNE AGEJE ALI

A DISSERTATION PRESENTED TO THE GRADUATE SCHOOL
OF THE UNIVERSITY OF FLORIDA IN
PARTIAL FULFILLMENT OF THE REQUIREMENTS
FOR THE DEGREE OF DOCTOR OF PHILOSOPHY

UNIVERSITY OF FLORIDA

1983

DEDICATION

Dedicated to my wife, Lucy Ige and my children, Shaibu Unekuojo, Omitenwuojo Ajanigo and Eleoje Unubi.

ACKNOWLEDGEMENTS

I would like to express my profound gratitude to Dr. John R. Ambrose, the chairman of my supervisory committee, and to Dr. Ellis D. Verink, Jr. for giving me the opportunity and for their guidance and inspiration throughout the course of my studies and research. I would like to thank Dr. R.T. DeHoff, Dr. P.H. Holloway, Dr. R.E. Reed-Hill and Dr. G.M. Schmid, for serving as members of my supervisory committee.

My special thanks to Dr. C. Batich for providing guidance on the use of and interpretation of results from x-ray photoelectron spectroscopy. I am grateful to Mr. M.A. Kosinski, Dr. A.D. Buonaquisti, S.K. Hofmeister and Mr. N.J. Bailer for their technical assistance. Diane Quirin's patience and understanding in typing this dissertation is gratefully appreciated.

The author is grateful to his parents for their foresight, courage and sacrifice. He is also grateful to his wife and children who have borne the brunt of the frustration associated with the Ph.D. program, and to his brother for his sacrifice and encouragement.

TABLE OF CONTENTS

PAGE

ACKNOWLEDGEMENTS iii

LIST OF TABLES vi

LIST OF FIGURES viii

ABSTRACT xvi

CHAPTER I
INTRODUCTION 1

CHAPTER II
LITERATURE REVIEW 5

- 2.1 Nickel 5
- 2.2 Nickel-Copper Alloys 16
- 2.3 Alloy Dissolution 45

CHAPTER III
EXPERIMENTAL PROCEDURE 52

- 3.1 Equipment and Materials 52
- 3.2 Experimental Procedure 52
  - 3.2.1 Potentiokinetic Polarization Experiments 52
  - 3.2.2 Potentiostatic Polarization 54
  - 3.2.3 Atomic Absorption Spectrophometric Experiments 54
  - 3.2.4 E.S.C.A. Analysis of Insoluble Dissolution Products 55
  - 3.2.5 Auger Electron Spectroscopic Analysis 56
  - 3.2.6 Scanning Electron Microscopic Characterization (SEM) of the Corrosion Product Morphology 57

CHAPTER IV
RESULTS AND DISCUSSION 60

- 4.1 Anodic Polarization in Deaerated Na_2SO_4 Solutions 60
  - 4.1.1 Linear Sweep Voltammetry 60
  - 4.1.2 Characterization of Soluble Reaction Products 62

4.1.3 Effect of Electrode Rotation Speed 79
4.1.4 X-ray Photoelectron Spectroscopic Analysis of Passive Films on Monel-400 Alloy 88
4.1.5 Auger Electron Spectroscopic Analysis of Passive Films on Monel-400 Alloy 101
4.2 Anodic Polarization in Deaerated 0.5 M NaCl Solution 109
4.2.1 Linear Sweep Voltammetry 109
4.2.2 Characterization of Soluble Reaction Products 111
4.2.3 Effect of Electrode Rotation Speed 126
4.2.4 Effect of Chloride Ion Concentration 131
4.2.5 Effect of Temperature 138
4.2.6 Behavior in the Presence of Oxygen 142
4.2.7 E.S.C.A. Analysis of Insoluble Dissolution Products 157
4.2.8 SEM/EDX Analysis of the Corroded Monel-400 Alloy Surface 162

CHAPTER V

CONCLUSION 181

CHAPTER VI

RECOMMENDATION FOR FURTHER STUDIES 183

BIBLIOGRAPHY 186

APPENDICES

1 List of Equipment 200

2 Sample Characterization and Preparation 201

3 Electrochemical Equipment 208

4 Test Solutions and Preparation 218

5 X-ray Photoelectron Spectroscopy 221

6 Auger Electron Spectroscopy 224

7 Determination of "Redox" Potentials for Nickel, Copper and Iron Soluble Reaction Products 228

BIOGRAPHICAL SKETCH 235

LIST OF TABLES

Table		Page
1	Results of Laboratory Tests on A Nickel Copper Series In Aerated 3 Per Cent Sodium Chloride	18
2	Redox Potentials of Possible Soluble Anodic Corrosion Products of Monel Alloy 400	65
3	Atomic Absorption Data From Potentiostatic Tests in Na_2SO_4 Solution at 298 K (25°C)	78
4	Binding Energy Data For Copper and Copper Compounds	92
5	Binding Energy Data for Nickel and Nickel Compounds	93
6	Atomic Absorption Data From Potentiostatic Tests in 0.5M NaCl Solution at 298 K (25°C)	121
7	Binding Energy Data for Ni (2p) Obtained in 0.5 M NaCl, pH 8.2, 298 K (25°C)	152
8	Binding Energy Data for Cu (2p) Obtained in 0.5 M NaCl, pH 8.2, 298 K (25°C)	153
9	Semiquantitative Elemental Ratios Obtained at Three Locations On Anodized Monel-400 Alloy Surface Air-saturated 0.5M NaCl	177
10	Composition of Monel-400 Alloy	202
11	Diffusion Currents for the Reduction of $Fe(CN)_6^{-3}$ at the Monel-400 Inner Ring (I_{RI}) and the Oxidation of $Fe(CN)_6^{-4}$ at the Glassy Carbon Outer Ring and the Collection Efficiency, N, for the Ring-Ring Electrode	214

Table Page

12 Diffusion Currents for the Reduction of $Fe(CN)_6^{-3}$ at the Disc (I_D) and the Oxidation of $Fe(CN)_6^{-4}$ at the Ring (I_R) and the Collection Efficiency, N, for the Glassy Carbon Ring - Monel-400 Disc Electrode . . . 215

13 Impurity Levels of Prepurified Nitrogen . . . 219

LIST OF FIGURES

Page

1 Anodic potentiostatic current(i)-potential(V) profile for a previously oxide free nickel electrode in pH 8.4 Na_2SO_4 solution with potential increments of 0.05V every 60 sec Measured current is that registered at the end of 60 sec. 6

2 Stationary potential current curve of nickel obtained by a potentiostatic method Electrolyte: 1n H_2SO_4. Temperature: 25°C 7

3 Effect of nickel content on the weight loss of Cu-Ni alloys in flowing seawater (8"x24" specimens, 2/3 immersed in seawater for 497 days, flow velocity 1.5 - 0.3 fps) 19

4 Potentiostatic anodic polarization curves for nickel and nickel-copper alloys in deaerated 1N H_2SO_4 at 25°C (77°F) 20

5 Critical and passive current densities for Cu-Ni alloys obtained from potentiostatic polarization curves (noble and active) in N_2-deaerated in H_2SO_4 at 25°C 21

6 Effect of copper concnetration on the corrosion behavior of Ni-Cu alloys 23

7 Steady state potentials of binary Cu-Ni alloys exposed to aerated 4% NaCl 24

8. Potentiodynamic anodic polarization curves for nickel 200 and Monel alloy 400 in aerated and deaerated 5N H_2SO_4 at room temperature 27

9 Effect of oxygen concentration of seawater on the corrosion of copper, nickel and Monel-400 alloy after 1 year of exposure 28

10 Effect of iron content on corrosion resistance of 70-30 cupronickel condenser tubes (velocity 20 fps, 90°F) 35

Page

11 Effect of iron content on corrosion rate of 90-10 cupronickel in seawater (velocity 0-4 fps, 300 day exposure) ... 37

12 Effect of iron content on the corrosion rate of 90-10 cupronickel alloys rotated in seawater (73°F) at 15 and 30 fps for 55 days. Heat treatment-quenched from 900°C ... 39

13 Effect of iron content on the corrosion rate of 90-10 cupronickel alloys rotated in seawater (73°F) at 15 and 30 fps for 55 days. Heat treatment-quenched from 900°C, 0.01-0.95% Fe held at 550°C for 2 hours. 1.19-1.96% Fe held at 600°C for 2 hours ... 40

14 Anodic potentiokinetic polarization curve for Monel-400 alloy in deaerated Na_2SO_4 at 298K (25°C), pH 8.2. Sweep rate (S) = 8.33mV 1 sec; electrode rotation speed (w) = 0rpm ... 61

15 Potentiokinetic polarization curve for glassy carbon collector electrode showing potential regions where soluble reaction products could be monitored, Monel-400 electrode held at +150mV. Deaerated Na_2SO_4, pH 8.2, 298K (25°C). S = 8.33mV/sec; w = 1600rpm ... 64

16. Potentiokinetic polarization curve for Monel-400 alloy in deaerated 0.5M Na_2SO_4, pH 8.2 at 298K (25°C). a) central electrode current, b) collector ring current; S = 8.33mV/sec; w = 1600rpm. Absence of structure in collector ring current confirms absence of Cu^+, Fe^{2+} and Fe^{3+} ions ... 67

17 Potentiokinetic polarization curve for Monel-400 in deaerated 0.5M Na_2SO_4, pH 8.2 at 298K (25°C). a) Monel-400 current; b) collector ring current, collector electrode -150mV. S = 8.33mV/sec; w = 1600rpm ... 69

18. Cathodic reduction of Cu(II) ions on a rotating carbon disc electrode. Deaerated 0.5M Na_2SO_4 solution, pH 8.2, containing $10^{-3}M$ Cu^{2+} ions. S = 20mV/sec ... 71

19 Current-time behavior; top: cathodic reduction of Cu(II) ions at -50mV (Ag/AgCl); bottom: oxidation of Cu(I) ions at +600mV (Ag/AgCl). w = 1600rpm ... 73

20 Potentiokinetic polarization curve for Monel-400 alloy in deaerated 0.5M Na_2SO_4, pH 8.2, at 298K (25°C); a) Monel-400 ring current. b) collector ring current S = 8.33mV/sec., w = 1600rpm ... 75

Page

21 Potentiokinetic polarization curves for Monel-400 in deaerated 0.5M Na_2SO_4, pH 8.2, at various electrode rotation speeds; 298K (25°C) S = 8.3mV/sec 80

22 Anodic peak current as a function of the square root of rotation speeds. Deaerated 0.5M Na_2SO_4 solution, pH 8.2 at 298K (25°C); S = 8.33mV/sec 81

23 Normalized collector ring current as a function of electrode rotation speed; E_R = -150mV. Deaerated 0.5M Na_2SO_4, pH 8.2, at 298K (25°C); S = 8.33mV/sec 83

24. Cu (2p) x-ray photoelectron spectrum for Monel-400 alloy surface exposed to deaerated 0.5M Na_2SO_4, pH 8.2, at 298K (25°C) for 0.5 hour 90

25 Ni (2p) x-ray photoelectron spectrum for Monel-400 alloy surface exposed to deaerated 0.5M Na_2SO_4, pH 8.2, at 298K (25°C) for 0.5 hour 91

26. Cu ($L_3M_{4,5}M_{4,5}$) Auger spectrum for Monel-400 alloy surface exposed deaerated 0.5M Na_2SO_4, pH 8.2, at 298K (25°C) 94

27. O (1S) x-ray photoelectron spectrum for Monel-400 alloy surface exposed to deaerated 0.5M Na_2SO_4, pH 8.2, at 298K (25°C) 97

28 Potential pH equilibrium diagram for the system copper-water at 25°C [Considering the solid substances Cu, Cu_2O and Cu $(OH)_2$] 98

29. Typical surface scan Auger spectrum from the surface of Monel-400 alloy exposed to deaerated 0.5M Na_2SO_4 solution, pH 8.2 at 298K (25°C) 102

30. Typical Auger spectrum from sputtered Monel-400 alloy surface exposed to deaerated 0.5M Na_2SO_4 solution, pH 8.2 at 298K (25°C) 103

31. Auger composition profile obtained from Monel-400 alloy exposed to deaerated 0.5M Na_2SO_4, pH 8.2, at 298K (25°C) 105

32. Auger composition profile in terms of Cu/Ni peak-to-peak ratio. Deaerated 0.5M Na_2SO_4, pH 8.2 at 298K (25°C) 107

33. Potentiokinetic polarization curve for Monel-400 alloy in deaerated 0.5M NaCl, pH 8.2, at 298K (25°C); S = 5mV/sec., w = 1600rpm 110

Page

34. Collector ring current density as a function of applied potential in deaerated 0.5M NaCl solution, pH 8.2 at 298K (25°C) S = 5mV/sec , w = 1600rpm ... 112

35 Cu(II) current density as a function of applied Monel-400 electrode potential Deaerated in 0.5M NaCl solution, pH 8.2 at 298K (25°C) S = 5mV/sec , w = 1600rpm ... 116

36 Normalized Cu(II) current density as a function of applied Monel-400 electrode potential in deaerated 0.5M NaCl solution, pH 8.2 at 298K (25°C) S = 5mV/sec , w = 1600rpm ... 118

37 Normalized Cu(II) current density as a function of applied Monel-400 electrode potential. Deaerated 0.5M NaCl solution, pH 8.2 at 298K (25°C) S = 5mV/sec , w = 1600rpm ... 119

38. Ratio of Cu(II) current density to Cu(I) current density as a function of applied Monel-400 electrode potential, 0.5M (deaerated) solution, pH 8.2 at 298K (25°C) S = 5mV/sec , w = 1600rpm ... 120

39 Normalized total copper current density as a function of Monel-400 applied potential. Deaerated 0.5M NaCl, pH 8.2, at 298K (25°C) S = 5mV/sec , w = 1600rpm. ... 123

40 Total copper current density as a function of applied Monel-400 electrode potential Deaerated NaCl, pH 8.2, at 298K (25°C) S = 5mV/sec., w = 1600rpm ... 124

41. Anodic potentiokinetic polarization curves for Monel-400 alloy in deaerated 0.5M NaCl, pH 8.2, at various rotation speeds; 298K (25°C) S = 5mV/sec ... 127

42. Normalized copper(I) current density as a function of applied Monel-400 electrode potential at various electrode rotation speeds Deaerated 0.5M NaCl, pH 8.2 at 298K (25°C) S = 5mV/sec ... 129

42 Normalized copper(I) current density as a function of applied Monel-400 electrode potential at various electrode rotation speeds. Deaerated 0.5M NaCl, pH 8.2 at 298K (25°C) S = 5mV/sec ... 120

44. Ratio of Cu(II)/Cu(I) current densities as a function of electrode potential at various rotation speeds. Deaerated 0.5M NaCl, pH 8.2 at 298K (25°C) S = 5mV/sec ... 132

Page

45. Normalized total copper current density as a function of Monel-400 electrode potential at various electrode rotation speeds. Deaerated 0.5M NaCl, pH ≅ 2 at 298K (25°C). S = 5mV/sec 133

46. Anodic potentiokinetic polarization curves for Monel-400 alloy at various chloride ion concentrations, pH ≅ 2, 298K (25°C). S = 5mV/sec., w = 1600rpm 134

47. Collector ring current density as a function of Monel-400 electrode potential at various chloride ion concentrations. pH ≅ 2 at 298K (25°C). S = 5mV/sec , w = 1600rpm. 135

48. Ratio of Cu(II)/Cu(I) current densities as a function of chloride ion concentration. pH ≅ 2 at 298K (25°C). S = 5mV/sec., w = 1600rpm 137

49. Logarithmic plot of Monel-400 dissolution current as a function of chloride ion concentration. pH ≅ 2 at 298K (25°C). S = 5mV/sec , w = 1600rpm 138

50. Anodic polarization curves for Monel-400 alloy in deaerated 0.5M NaCl. pH ≅ 2, at various temperatures. S = 5mV/sec , w = 1600rpm 140

51. Arrhenius plot of Monel-400 alloy current in deaerated 0.5M NaCl. pH ≅ 2. S = 0mV/sec., w = 1600rpm 141

52. Arrhenius plot of collector ring current in deaerated 0.5M NaCl. pH ≅ 2. S = 0mV/sec., w = 1600rpm 143

53. Comparison of anodic polarization curves for Monel-400 alloy in deaerated and air-saturated NaCl, pH ≅ 2, at 298K (25°C). S = 5mV/sec., w = 1600rpm 144

54. Comparison normalized collector ring current densities obtained in deaerated and air-saturated 0.5M NaCl, pH ≅ 2, at 298K (25°C). S = 5mV/sec , w = 1600rpm 146

55. Collector electrode current density as a function Monel-400 electrode potential in air-saturated 0.5M NaCl, pH ≅ 2, at 298K (25°C). S = 5mV/sec , w = 1600rpm 147

56. Ratio of Cu(II) - Cu(I) current densities as a function of Monel-400 electrode potential in air-saturated 0.5M NaCl pH ≅ 2, at 298K (25°C). S = 5mV/sec , w = 1600rpm 148

57. Anodic polarization for Monel-400 alloy in air-saturated 0.5M NaCl, pH ≅ 2, at various rotation speeds. S = 5mV/sec 149

Page

58. Ratio of Cu(II) to Cu(I) current densities as a function of Monel-400 electrode potential in air-saturated 0.5M NaCl, pH 8.2, at various electrode rotation speeds. S = 5mV/sec 151

59. Ni ($L_3M_{4,5}M_{4,5}$) Auger spectrum for Monel-400 alloy surface exposed to deaerated 0.5M NaCl, pH 8.2, at 298K (25°C) 154

60. Ni (2p) x-ray photoelectron spectrum for Monel-400 alloy surface exposed to deaerated 0.5M NaCl, pH 8.2, at 298K (25°C). E_{appl} = 0V 155

61. O (1s) x-ray photoelectron spectrum obtained from the surface of Monel-400 alloy exposed to deaerated 0.5M NaCl, pH 8.2, at 298K (25°C), E_{appl} = 0V 156

62. Cu (2p) x-ray photoelectron spectrum for Monel-400 alloy exposed to deaerated 0.5M NaCl, pH 8.2, at 298K (25°C); E_{appl} = 0V 159

63. Cu ($L_3M_{4,5}M_{4,5}$) Auger spectrum for Monel-400 alloy surface exposed to deaerated 0.5M NaCl, pH 8.2, at 298K (25°C); E_{appl} = 0V 160

64. Ni (2p) x-ray photoelectron spectrum for Monel-400 alloy surface exposed to air-saturated 0.5M NaCl, pH 8.2, at 298K (25°C); E_{appl} = 0V 161

65. Cu (2p) x-ray photoelectron spectrum for Monel-400 alloy exposed to air-saturated 0.5M NaCl, pH 8.2, at 298K (25°C); E_{appl} = 0V 163

66. Cl (2p) x-ray photoelectron spectrum exposed to air-saturated 0.5M NaCl, pH 8.2 at 298K (25°C); E_{appl} = 0V 164

67a. Scanning electron micrograph of a corroded Monel-400 alloy sample exposed to air-saturated 0.5M NaCl, pH 8.2 at 298K (25°C) for 24 hours at 0V (Ag/AgCl). Micrograph obtained before washing the sample 165

67b. Scanning electron micrograph of a corroded Monel-400 alloy sample exposed to air-saturated 0.5M NaCl, pH 8.2 at 298K (25°C) for 24 hours at 0V (Ag/AgCl). Micrograph obtained after washing the sample 166

68a. Scanning electron micrograph of a corroded Monel-400 alloy sample exposed to air-saturated 0.5M NaCl, pH 8.2 at 298K (25°C) for 24 hours at 0V (Ag/AgCl). Micrograph obtained at higher magnification and before washing. Star-like crystals are NaCl crystals 169

Page

68b. Scanning electron micrograph of a corroded Monel-400 alloy sample exposed to air-saturated 0.5M NaCl, pH 8.2 at 298K (25^{o}C) for 24 hours at OV (Ag/AgCl). Micrographs showing pits was obtained at higher magnification after washing the sample 170

69. Scanning electron micrograph of a corroded Monel-400 alloy sample exposed to air-saturated 0.5M NaCl, pH 8.2 at 298K (25^{o}C) for 24 hours at OV (Ag/AgCl). Micrograph obtained after washing 171

70. EDX spectrum for the star-like crystals found on the surface or corroded Monel-400 alloy 172

71. EDX spectrum obtained from the surface of a corroded Monel-400 alloy 173

72. EDX spectrum of the dendrite-like structure on the surface of a corroded Monel-400 alloy 174

73. EDX spectrum obtained inside a pit on a corroded Monel-400 alloy 175

74. Microstructure of Monel-400 alloy 200X 202

75. Copper-nickel equilibrium phase diagrams; top (207); bottom (208) 205

76. Schematic drawing of the sectioned polished jib 207

77. Schematic drawing of the tip section of the rotating ring-ring electrode 210

78. Rotating ring-disc electrode assembly attached to the motor drive 211

79. Original and modified rotating ring-ring electrode 213

80. Electrochemical cell 216

81. Energy level diagrams and energy distribution N (E) and dN/dE for a silver target 222

82. Operation of XPS spectrometer (From class note) 225

83. Operation of a cylindrical mirror analyser as an Auger spectrometer (177) 227

84. Reduction of nickel on a rotating glassy carbon disc electrode at various rotation speeds. Deaerated 0.5M Na_2SO_4 solution, pH 8.2 containing 10^{-3}M Ni^{2+} ions at 298K (25^{o}C) 229

Page

85. Reduction of copper on a rotating glassy carbon disc electrode at various rotation speeds. Deaerated 0.5M Na_2SO_4, pH 8.2 containing 10^{-3}M Cu^{2+} ions at 298K (25°C). 230

86. Oxidation of Cu(I) ions on a rotating glassy carbon ring electrode at various rotation speeds. Deaerated 0.5M Na_2SO_4, pH 8.2 at 298K (25°C) 231

87. Oxidation of ferrous ions on a rotating glassy carbon disc electrode at various rotation speeds. Deaerated Na_2SO_4 solution, pH 8.2 containing 10^{-3}M Fe^{2+} ions at 298K (25°C) 232

88. Reduction of ferric ions on a rotating glassy carbon ring electrode at various rotation speeds. Deaerated 0.5M Na_2SO_4, pH 8.2 at 298K (25°C) 233

Abstract of Dissertation Presented to the Graduate School of the University of Florida in Partial Fulfillment of the Requirements for the Degree of Doctor of Philosophy

DISSOLUTION KINETICS OF MONEL ALLOY 400 IN AQUEOUS SOLUTIONS

By

JOSEPH ABUNE AGEJE ALI

December 1983

Chairman: Dr. John R. Ambrose
Major Department: Materials Science and Engineering

This study has been carried out with a view to characterizing the electrodissolution behavior of Monel-400 alloy with respect to the dissolution products (soluble and insoluble). The study has been conducted in sodium sulfate (Na_2SO_4) and sodium chloride (NaCl) solutions. The Rotating Ring-Disc Electrode (RRDE) and Ring-Ring Electrode (RRRE) have been used in combination with linear sweep voltammetry as major techniques for characterizing the soluble reaction products. The insoluble reaction products have been analyzed using x-ray Photoelectron Spectroscopy (XPS) and Auger Electron Spectroscopy (AES).

Dissolution of copper from nickel-copper alloys in Na_2SO_4 solution proceeds directly to Cu(II) species without generation of Cu(I) intermediates. Anodic reaction of Monel-400 alloy has been found to be strongly mass transport dependent with the reaction showing different behaviors below and above 1600 revolutions per minute (rpm). A model has been proposed that provides an explanation of the behavior under different fluid flow conditions.

In addition to Cu(II) and nickel ions, Cu(I) ions (mainly $CuCl_2^-$) are generated in the presence of chloride ions of concentration $5 \times 10^{-2}M$ or higher. The distribution of both copper species as a function of applied electrode potential is such that in deaerated NaCl solutions Cu(I) species predominate in the low over-potential region while Cu(II) species dominate in the high over-potential region. This distribution is reversed in the presence of oxygen.

There are strong indications linking the corrosion behavior of Monel-400 alloy in both solutions to dissolution kinetics of copper in the alloy. Precipitation of atacamite ($CuCl_2 \cdot 3Cu(OH)_2$) on the surface of the alloy has been associated with pit initiation on Monel-400 alloy.

CHAPTER 1
INTRODUCTION

The level of scientific exploration and technological exploitation of the hydrospace has reached new highs. The reasons are not difficult to find. First is the realization that the world's traditional sources of industrial minerals and food may no longer sustain expanded future demands because of increasing world population. Second, there is a quest of the industrialized nations to reduce their overdependence on the less technologically developed nations for their vital mineral needs. The future trend is toward greatly accelerated pace of activities in this environment as more and more nations strive to attain industrial status.

While considerable interest is centered around off-shore minerals development and seawater extraction of minerals, attention is increasingly being focused upon food production and the extraction of fresh water from seawater. These technological activities require the construction and use of installations which are partially or wholly immersed in the environment. Seawater is complex and very aggressive to most metals. These characteristics are due primarily to its salt content but also to its high biological activity. A consequence of this is that seawater supports certain organisms which attach themselves to structures immersed in it (biofouling). Most existing materials of construction are attacked by seawater and/or are susceptible to biofouling at least to some extent. The role of a materials engineer in these engineering ventures is [illegible] difficult and, as always, an important one.

To meet the increased demand for materials application in hydrospace environments, both in performance and reliability, the development of new materials, and the improvement in the properties of the materials which have found use in this environment, are desirable. As part of any materials development program, the need exists for increased activity in both basic and applied corrosion research in order to advance our understanding of the characteristic properties of the materials which are responsible for their corrosion resistance or lack thereof. Such a study would necessarily include, among other things, a determination of properties of the environment which tend to undermine or enhance the corrosion resistance of these materials. The knowledge thus acquired would help set the direction and establish guidelines for further materials development programs. These programs would focus not only upon the development of new materials but also on the improvement of the properties of the currently used materials as well as the development of other corrosion control measures.

Alloys of nickel and copper have long enjoyed popularity in seawater applications largely because of their good corrosion resistance. Copper-nickel alloys (copper-base) such as 90 Cu-10 Ni (CDA 706) and 70 Cu-30 Ni (CDA 715) are widely used for flowing seawater applications such as heat exchange tubes and condensers. However, their susceptibility to impingement attack resulting from high fluid velocity limits their application to seawater velocities below about 15 feet per second (f.p.s.). One important advantage of these alloys is that because of their high copper content they suffer little or no biofouling. This makes them suitable for applications in low velocity and/or stagnant seawater environments.

Nickel-copper alloys (nickel-base) such as Monel-400, on the other hand, are more resistant to impingement effects and are therefore more widely preferred for high seawater velocity applications as for pump impellers, propellers and in hydrofoils. However, performance of Monel-400 alloy could be seriously compromised when exposure conditions are such that seawater velocities drop below about 6 feet per second. Under the stated conditions, the material becomes susceptible to severe pitting attack. Although a great deal is known regarding empirical limits between which adequate performance is achieved, especially with respect to oxygen concentration, seawater flow velocities and galvanic couples, little is known regarding the mechanisms by which the attack initiates and propagates.

A program has been initiated in the Department of Materials Science and Engineering at the University of Florida to study the general corrosion behavior of nickel-copper alloys with emphasis on the mechanisms of pit initiation and propagation on Monel-400 in natural seawater. It is well known that the presence of a protective film is a necessary condition for pitting to occur in metals and alloys that exhibit passivity. The reactions occurring in the active or low overvoltage region, in effect, control the onset and maintenance of the passive condition and consequently the pitting behavior of a metallic material. Therefore, understanding the detailed mechanism of dissolution in the active region is a logical and necessary step before venturing into the determination of mechanisms of pit initiation and propagation

The present investigation, which is the initial phase of the overall program, is, accordingly, confined to characterizing the electrodissolution behavior of this alloy with respect to the dissolution products (soluble and insoluble). This initial study has been conducted in sodium sulfate (Na_2SO_4) and sodium chloride (NaCl) solutions. While the emphasis of this study has been in NaCl solutions because of the high concentration of chloride ions in seawater, a study in Na_2SO_4 was necessary to determine behavior in a non-complexing environment Among the general objectives of this phase of the program was to generate data that would contribute to future decisions regarding the direction of the overall program The results were also used to define areas of emphasis in subsequent studies of pitting behavior in seawater both in the laboratory and in the natural environment.

CHAPTER II
LITERATURE REVIEW

2.1 Nickel

Since this is a study of Monel-400, a nickel base alloy, a brief review of studies of nickel in aqueous solutions will provide a useful basis for understanding the behavior of this alloy. This review emphasizes only those points concerning nickel electrochemistry that are still in controversy.

The electrochemical behavior of nickel in both acidic and alkaline aqueous solutions is well documented. There is unanimity among the investigators that nickel, under passivating conditions, exhibits three regions, active, passive and transpassive, in its anodic current potential relationship as shown in Fig. 1. However, as shown in Fig. 2, a fourth behavior in the transpassive region, generally referred to as secondary passivity has been observed[1-3]. This region is characterized by a current maximum followed by a minimum. It is generally agreed that dissolution in the active region is by oxidation to Ni(II) ions or their soluble intermediates. But Weininger and Breiter[3] have suggested that the formation of nickel hydroxide ($Ni(OH)_2$) may well be the only reaction in the active region. Most literature reports indicate that dissolution in the transpassive region, also to Ni(II) products, occur in parallel

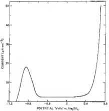

Figure 2 Anodic potentiostatic current(i)-potential(V) profile for a previously oxide free nickel electrode in pH 8.4 Na_2SO_4 solution with potential increments of 0.05V every 60 sec Measured current is that registered at the end of 60 sec. (6)

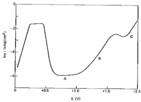

Figure 2 Stationary potential current curve of nickel obtained by a potentiostatic method Electrolyte: 1n H_2SO_4 Temperature: 25°C.

with water oxidation (oxygen evolution). Dissolution in this region is reported to occur preferentially at grain boundaries. At potentials above the secondary passivity region dissolution of nickel to Ni(III) has been reported.[1,2,4,5] Dissolution in this region is reported also to take place preferentially at grain boundaries.

Despite the extensive investigation of the passivity of nickel, there is still controversy about the nature of the film present and the mechanisms by which the film forms. Several species of nickel oxides have been suggested as causing the passivation of this metal either singly or in combinations.

MacDougall and Cohen[6-8] and MacDougall et al.[9] have studied the anodic behavior of nickel in Na_2SO_4 solutions of various pH values ranging from 2.0 to 8.4. They concluded that NiO is the passivating film on nickel in sulfate solutions. Cowan and Staehle[10] found both NiO and Ni_3O_4 in acidic sulfate solutions. They, however, suggested that the passive oxide film was probably Ni_3O_4. Okamoto and Sato[1,2,4] observed that NiO is not responsible for the passivity of nickel and that either Ni_3O_4 or a duplex oxide film of Ni_3O_4 and NiO causes passivity of nickel in sulfate solutions. J. O'M. Bockris et al.[11] studied the mechanisms of anodic passivity of nickel in acidic sulfate solutions using ellipsometry. They identified the film that forms at potentials cathodic to the passivation potential (prepassive film) to be $Ni(OH)_2$. They reported that this precursor film converts at potentials anodic to the passivation potential to a passive layer of composition $NiO_{1.5-1.7}$. They cited the results of earlier investigation by Briggs and Wynne-Jones[12] to support their own results. In that investigation Briggs et al. studied the conversion of $Ni(OH)_2$ to a nonstoichiometric oxide using a combination of x-ray diffraction and electrochemical measurements. They found $NiO_{1.7}$ to be the final product of conversion. DeGromoboy and Shreir[13] studied the formation of oxides during the passivation of nickel in solutions of sulfuric acid and acetic-acetate buffers at various pH values. They showed that the potential arrests which correspond to the reversible metal oxide/metal electrode potentials have a linear relationship with pH. They concluded from their studies that passivity of nickel could be due to either NiO, Ni_3O_4, Ni_2O_3 or NiO_2.

D. E. Davis and W. Barker[14] studied the passivation of nickel in sodium carbonate and sodium borate solutions using a galvanostatic technique. They concluded that passivation of nickel is caused by the formation of a monolayer of $Ni(OH)_2$ in alkaline solutions and by 1-2 molecular layers in borate solutions. Weininger et al.[3] using electron diffraction and microscopy also identified $Ni(OH)_2$ on nickel polarized in 0.2N KOH.

Two general theories of passive film formation on nickel have been proposed. These are dissolution-precipitation[1,2,4,11] and solid state oxidation (direct oxidation of metal surface).[3,6-9,13-15] In the dissolution-precipitation mechanism first proposed by Muller,[16] nickel dissolves into a soluble intermediate (Ni^{++} or $NiOH^{+}$). The dissolved species accumulates at the interface until the solubility limit of a nickel compound (oxide or hydroxide) is exceeded. The compound then precipitates onto the surface of dissolving nickel specimen, forming a barrier between the surface and the electrolyte. The deposited film may cause passivation, or undergo further reaction and be finally transformed to a form that causes passivation. The precipitate is generally believed to be either an oxide or a hydroxide of nickel. Bockris et al.[11] and Sato and Okamoto[1,2,4] have reported that the soluble intermediates formed during anodic dissolution of nickel is $NiOH^+$. The two steps however, have disagreed on the type of precipitate formed. According to Bockris et al[11] $Ni(OH)_2$ is the precipitate formed from the supersaturated solution of $NiOH^+$. They offered the following mechanism of dissolution

$$Ni + OH^- \rightleftarrows NiOH_{ads} + e \qquad [1a]$$

$$NiOH_{ads} \rightarrow NiOH^+ + e. \qquad [1b]$$

The $NiOH^+$ accumulates at the interface until its solubility limit is reached; then it precipitates out as $Ni(OH)_2$. Sato and Okamoto, on the other hand, have suggested that the precipitation of supersaturated solution of $NiOH^+$ is either to NiO at potentials cathodic to the passivation potential or to Ni_3O_4 at the passivation potential. They proposed the following mechanism:

$$Ni + OH^- \rightarrow NiOH^+ + 2e; \qquad [2a]$$

At potentials cathodic to the passivation potential, the $NiOH^+$ precipitates thus

$$NiOH^+ \rightarrow NiO + H^+; \qquad [2b]$$

the NiO being further converted at the passivation potential according to the following reaction

$$3NiO + OH^- \rightarrow Ni_3O_4 + H^+; \qquad [2c]$$

$NiOH^+$ may also precipitate directly to Ni_3O_4 at the passivation potential or at nobler potentials as shown

$$3NiOH^+ \rightarrow Ni_3O_4 + 4H^+ \qquad [2d]$$

These mechanisms suggest that both anodic dissolution and the onset and maintenance of passive condition should depend strongly on the concentration of OH^- ions in solution. In fact, Sato and Okamoto in another study[17] proposed that the anodic dissolution of nickel in acidic solutions is catalyzed by OH^- and that the overall rate of the reaction is controlled by the concentration of OH^-. While this mechanism may provide the basis for accounting for the slow anodic dissolution of nickel in acidic media, it may not completely explain the passive behavior of nickel observed in concentrated acidic solutions.

In the solid state mechanism, there is a direct electrochemical reaction between the nickel electrode and water from the solution to form an oxide or a hydroxide by the process of two-dimensional nucleation and growth. MacDougall and Cohen[6] postulated the following mechanism:

$$Ni + H_2O \rightarrow NiO + 2H^+ + 2e^- . \qquad (3)$$

Gavle and Barker,[14] however, indicated that direct oxidation of nickel during anodic polarization results in the formation of $Ni(OH)_2$ according to the following reaction:

$$Ni + 2H_2O \rightarrow Ni(OH)_2 + 2H^+ + 2e^- \qquad (4)$$

This is in agreement with the mechanism proposed by Weininger et al [3]

Cowan and Staehle[10] investigated the influence of temperature on the thermodynamics and electrode kinetic behavior of nickel The study was conducted in sulfate solutions of pH 1.3, 3 4 and 6 3 using potentiostatic, potentiodynamic and potential decay techniques. They observed that the active passive transition behavior of nickel observed at room temperature was absent at temperatures above 373K (100°C).

Even though they found evidence of oxide film formation above 523K (250°C), no passivity was observed above this temperature

Kronenberg et al.[18] also studied the mechanism of anodic dissolution of nickel as a function of temperature, in acidified chloride, sulfate and perchlorate solutions. They determined the heat of activation in chloride solution to be 15 Kcal/mole. The Tafel slopes determined at 318K (45°C) were 85, 115 and 120 mV/dec in chloride, sulfate and perchlorate solutions, respectively. They attributed the lower value of Tafel slope in chloride solution to specific absorption of the ion.

A. Bengali and K. Nobe[16] studied the effect of chloride ion concentration on the dissolution kinetics of nickel in acidic chloride solutions of constant ionic strengths of 1 and 5M. They found the Tafel slope to be 2.303RT/F (60 mV/dec). The anodic dissolution in low $[H^+]$-chloride solutions was observed to be accelerated by both OH^- and Cl^-. In highly acidic concentrated chloride solution, the dissolution was accelerated by both Cl^- and H^+ with first order dependence on both species. They offered the following mechanism for nickel dissolution in acidic chloride media for low H^+ and Cl^- concentration (each < 1M) of both ionic strength solutions (1 and 5M) the steps are

$$Ni + H_2O + Cl^- = NiClOH^-_{ads} + H^+ + e^- \qquad [5a]$$

$$NiClOH^{-}_{ads} \;\underset{=}{\underline{r\ d\ s}}\; NiClOH + e^{-} \qquad [5b]$$

$$NiClOH + H^{+} = Ni^{++} + Cl^{-} + H_2O; \qquad [5c]$$

In the highly acidic chloride solution ($[H^{+}]>1M$) of 5M ionic strength solution, the dissolution steps are as follows

$$Ni + Cl^{-} = NiCl_{ads} + e^{-} \qquad [6a]$$

$$NiCl_{ads.} + H^{+} \;\underset{=}{\underline{r\ d\ s}}\; NiClH^{+} \qquad [6b]$$

$$NiClH^{+} + Cl^{-} = NiCl_2 + H^{+} + e^{-} \qquad [6c]$$

$$NiCl_2 = Ni^{++} + 2Cl^{-} \qquad [6d]$$

As they observed in their conclusion, nickel-chloro complexes are important dissolution intermediates in the dissolution of nickel in chloride solutions

Ives and Zamin[20] investigated the effect of grain size and cold work on the anodic polarization behavior of nickel in acidic chloride solutions using a potentiostatic technique in combination with in-situ microscopic examinations. They reported that a variation of grain size from 0.025 to 0.330 mm and cold working to 40% did not affect the critical breakdown potential They, however, observed that at smaller grain sizes, pits formed preferentially at grain boundaries, at larger grain sizes the pits formed within the grains, and with an increase in concentration. They noted that most of the surface attack and nucleation of pits occurred in the active region, i.e., before the onset of passivity. This is especially interesting since pitting has traditionally been associated with the presence of a passivating film. The fact that they conducted their experiments with electropolished samples did not rule out the presence of a resistant film on their samples.

The influence of composition and structure on the electrochemical reactivity of nickel in 1N $NiSO_4$ solutions containing less than 3 millimoles per liter chloride has been reported.[21] The electrochemical reactivity of nickel was determined in terms of corrosion potential, corrosion currents, Tafel slope, passivation potential, critical current density for passivity, passive potential region and passive current. The additives studied included carbon, silicon, sulfur, selenium, tellurium and phosphorus. With the possible exception of tellurium and selenium, the other additives are often found in Monel-400. It was reported that sulfur, tellurium, phosphorus and selenium significantly restrict the passivity of nickel and thus tend to make nickel more reactive. It was reported that the relative effectiveness of these elements in restricting passivity was in the order of their electronegativities as shown

$$S > P > C > Si$$

with the electronegativities of tellurium and selenium reported to be between those of sulfur and phosphorus.

The corrosion resistance of nickel in marine environments varies depending on the condition of exposure. In fast flowing seawater its uniform corrosion rate is very low, ranging up to 5 mils per year (mpy).[22,23] This is because the flow of water ensures adequate supply of oxygen needed to maintain the passivity to which nickel owes its corrosion resistance. On the other hand, in moderately flowing or stagnant seawater, nickel loses some of its passivity at local sites resulting in serious localized corrosion attack. The low velocity and/or stagnant conditions not only cause an inadequate supply of oxygen needed to maintain the protective properties of the passive film but also create conditions favorable to biological fouling. The susceptibility of nickel to biofouling under these conditions has been widely reported.[24-31] The attachment of marine organisms leads to insufficient supply of oxygen to areas under the organisms. This condition leads to two consequences detrimental to the performance of this metal. First, because of lack of supply of oxygen, the passive properties are not fully maintained beneath the organisms. Secondly, localized oxygen concentration cells are created under the deposit. The combination of local breakdown of passivity and oxygen concentration cells creates appropriate conditions for pitting and crevice corrosion attack.

2.2 Nickel-Copper Alloys

Nickel forms a series of solid solution alloys with copper, including Monel-400 alloy, which are resistant to marine environments. It has been determined that the overall corrosion resistance of nickel-copper alloys increases as the nickel content of the alloy increases.[26,27] This effect of nickel is clearly demonstrated in Table 1 and Fig. 3. Osterwald and Uhlig[30] have investigated the anodic polarization and passivity of nickel and nickel-copper alloys in deaerated sulfuric acid using a potentiostatic method. The effect of copper additions, clearly illustrated in Fig. 4, is to shift the whole polarization curve to more noble values. The presence of copper also has the effect of contracting the passive region. In addition, and as can be seen in Fig. 5, the values of the critical current density for passivity (P_1) and the passive current density (P_3) increase as the amount of copper in the alloy increases. It can also be seen from the curves that above a certain value of copper content, the alloy does not exhibit passive behavior. According to this and other studies,[31,32] passivity of some nickel-copper alloys is not a property of copper but of nickel. A critical copper composition above which passivity is no longer observed has been reported to fall between 60 and 70% Cu. The loss of passivity above the critical copper composition has been explained by Uhlig.[33] The explanation was based on electron-configuration theory of passivity first proposed by himself and Wulff.[34] According to this theory, metals or alloys which exhibit passive behavior contain unfilled d-bands. The empty d-bands favor chemisorption of oxygen of less than a monolayer to multilayer dimensions. He considers this chemisorbed film to cause passivation of these metals and alloys.

The d-band of energy levels in nickel contains 0.6 vacancy per surface atom. Alloying copper with nickel increases the electron density

Table 1. Results of Laboratory Tests on A Nickel Copper Series In Aerated 3 Per Cent Sodium Chloride

Temperature: 86 degrees F.
Agitation: Specimens moved at a velocity of 15 feet per minute
Duration of Tests: 20 hours.

Approximate Composition of Alloy	Rate of Corrosion in mg./sq. dm /day
100% Copper	76
70% Copper, 30% Nickel	28
55% Copper, 45% Nickel	28
30% Copper, 70% Nickel	2
100% Nickel	2

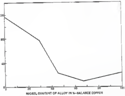

Figure 3 Effect of nickel content on the weight loss of Cu-Ni alloys in flowing seawater (8"x24" specimens, 2/3 immersed in seawater for 497 days, flow velocity 1.5 - 3.0 fps). (28)

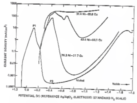

Figure 4. Potentiostatic anodic polarization curves for nickel and nickel-copper alloys in deaerated 1N H_2SO_4 at 25°C (77°F). (23)

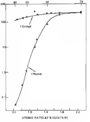

Figure 5 Critical and passive current densities for Cu-Ni alloys obtained from potentiostatic polarization curves (noble to active) in N_2 -deaerated 1N H_2SO_4 at 25°C. (35)

since copper has one electron more than nickel. The electrons supplied by copper are used to fill up the vacant 3 d-band of nickel. The critical composition of 60-70% Cu corresponds to approximate filling of the vacant d-band of nickel. On this basis he concluded that nickel-copper alloys containing more than the critical composition of copper do not possess passive properties. By the same reasoning he noted that other solid solution alloying additions such as Al, Zn, Ga which have more than one electron per atom than nickel will shift the critical copper composition to lower values. On the other hand, as has been reported,[35-39] alloy additions which have fewer electrons per atom than nickel will contribute electron vacancies, thus shifting the critical composition of copper to higher values. As Koizumi and Uhlig[31] have observed, the critical composition is also influenced by environment composition. They reported that SO_4^{2} and OH^- ions added to NaCl solution displace the critical composition of the nickel-copper alloys to higher copper composition.

The corrosion behavior of nickel-copper alloys ranging in composition from 100% Ni to 100% Cu has also been investigated by others.[40] As can be seen from Fig. 6, a minimum occurs in the corrosion rate in the composition range between 20 and 40% Cu. This is similar to the behavior shown in Fig. 3. It is noteworthy that the composition of Monel-400 falls in the composition range for minimum corrosion rate. It is also noteworthy that the composition of copper in the region of minimum corrosion rate is below the critical composition. This means that the alloy composition in the region of minimum corrosion rate owes its corrosion resistance to the presence of passive film(s). As Fig. 7 shows, the open-circuit or steady state potential determined in aerated 4% NaCl solution at 25°C displays

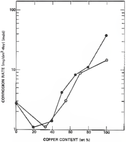

Figure 6   Effect of copper concentration on the corrosion behavior of Ni-Cu alloys (40)

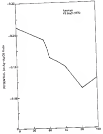

Figure 7: Steady state potentials of binary Cu-Ni alloys exposed to aerated 4% NaCl. (40)

similar dependence on nickel as the corrosion rate. Hence, increasing nickel content increases the steady-state potential in the noble direction up to about 80% nickel. Above 80% nickel, the steady-state potential shifts in the more active direction.

Since its incidental discovery 78 years ago (1905) Monel metal has been the most widely used nickel-copper alloy in marine environments. Monel is a solid solution alloy of approximately 70% Ni and 30% Cu. This alloy has seen a multiplicity of applications not only in seawater but also in chemical industries such as petrochemical industries, food processing industries, etc. Given the importance of this alloy and its prevalent use in marine environments, it is surprising that most literature reports concerning the corrosion behavior of this alloy have been based on open-circuit exposure tests in natural environments such as in seawater. Only a handful of publications relevant to fundamental electrochemical corrosion studies are available[30,31, 41-46]. This is not to say that open-circuit exposure tests are not important. As a matter of fact, they are the most critical and the ultimate in applied research. But as Cohen aptly put it[47]:

> When a metal is placed in contact with a corrosive solution a very complex set of reactions occurs. It is the function of corrosion research to separate the various processes which take place and evaluate the effect of each on the overall corrosion reaction. A complete understanding of each individual process requires the solution of problems in mechanism (including chemical thermodynamics), kinetics, and because the reactions are heterogeneous, some knowledge of structural and topographical factors. Although a single technique may yield information regarding more than one of these problems, in general the use of a number of techniques is required to obtain a complete understanding of the total corrosion process. (page 2)

Separating the various processes in order to study the influence of each on the overall corrosion reaction is not always practical in studies involving direct exposure to practical environments since, most of the time, we cannot change the environmental variables.

In neglecting fundamental laboratory tests, advantage is not taken of the most significant attribute of these tests, i.e., the ability to separate and investigate the influence of individual experimental variables; deduction of mechanisms becomes more difficult. As a result, and as will be pointed out later, despite a long history of usage, many fundamental questions regarding the corrosion behavior of this alloy remain unanswered.

It has been demonstrated[25,41] (see Fig. 8) that Monel alloy is superior to nickel in corrosion resistance in the active region but inferior to nickel in the passive region. As can also be seen from Fig. 8, the presence of oxygen causes an increase in the reactivity of Monel in all ranges of potential. This effect of oxygen was also investigated by Reinhart and others[48] who showed a linear relationship between the corrosion rate of Monel-400 and oxygen concentration in seawater (see Fig. 9). Monel, like nickel, owes its corrosion resistance to the presence of a passivating film on its surface. A notable feature of this film that is of great engineering significance is its ability to maintain its passive property even in highly turbulent and erosive conditions. This may explain its resistance to impingement attack in high velocity flowing seawater.

Monel suffers little or no general corrosion in seawater. But in slow-flowing or quiet seawater, it, like nickel, has been reported to

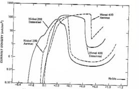

Figure 8. Potentiodynamic anodic polarization curves for nickel 200 and Monel alloy 400 in aerated and deaerated 5N H_2SO_4 at room temperature (23)

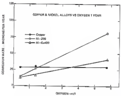

Figure 9. Effect of oxygen concentration of seawater on the corrosion of copper, nickel and Monel-400 alloy after 1 year of exposure (redrawn from reference 48).

suffer severe pitting attack.[24-28,45,48-52] As with nickel, the pitting is believed to be caused by oxygen starvation which hinders the self-healing ability of the film. It has been determined that a minimum effective seawater flow velocity of approximately 2 m/sec (6 fps) is necessary to assure this ability.[49] Monel also suffers from biofouling which tends to compound the effect of oxygen deficiency in quiet seawater. It has been reported that the amount of cuprous ions released during the corrosion of Monel in seawater is insufficient to poison biological organisms that cause biofouling.[26,29] According to LaQue,[26] fouling is less likely to occur where the copper content of nickel-copper alloys exceeds 60% by weight. Below 50% copper the tendency to foul exists; the extent of fouling varies in the composition range between 50 and 60% depending on the conditions of exposure. It should be noted that this observation tends, in a way, to confirm Uhlig's hypothesis. As discussed earlier, above 60% copper, the alloy has lost its passivating ability. Thus the corrosion rate may be high enough to generate sufficient cuprous ions to inhibit fouling.

An interesting feature of pits on Monel is that most of these pits are not deep. As has been reported,[25,26,53] after initial rapid penetration, most pits on Monel propagate in two dimensions thus leaving a shallow trenched structure on the surface. Except in situations where a part made of Monel is subjected to cyclic loading, as in propellers, this pit morphology does not pose serious problems and is therefore more desirable. As can be seen from reference 53, pit propagation on Monel does not always arrest at limiting depth.

On occasions the pits perforate the material. It is the latter behavior that limits the performance of this alloy. No satisfactory theory has yet been offered to explain the pitting behavior in Monel-K. May[54] observed similar pit morphology on cupro-nickels and suggested that the pits widen rather than deepen because their propagation is stifled by formation of a new protective film. Hettiarachchi et al.[42] examined the morphology of high nickel alloys, including Monel, in the region of breakdown of passivity and found pale green corrosion products covering some of the pits. This observation tends to support May's theory of the pit morphology.[54] While the presence of film may explain the fact that pit propagation tends to slow down with time, it is doubtful whether it explains the widening of the pits.

May's observation may be significant in some other way. The fact that this pit morphology also occurs on a copper base alloy may suggest that copper in Monel plays a role in pitting behavior. In fact, Fink and Boyd[25] have reported that copper additions provide some improvement in the pitting resistance of Monel over that of nickel. The mechanism by which copper accomplishes this is yet to be determined. It is generally believed that initiation and perhaps propagation of pits in freely corroding materials frequently involves the operation of concentration cells (oxygen and/or metal ion). As has been observed,[25,26,28] nickel and its alloys are more susceptible to differential aeration cells while copper and its alloys are more affected by metal ion concentration cells. Since the direction of current flow in both types of concentration cells is such that they oppose each other, it follows, as LaQue[26] has suggested, that with an appropriate composition of alloy the opposing corrosive forces should tend to balance each other and thereby reduce or eliminate, localized corrosion resulting from concentration cells. There is little doubt that the initial stage of pitting on Monel is under the control of the action of oxygen concentration cell. In time, the accumulated concentration of dissolved copper ions in the pit or under the deposit may be such that the corrosive force of metal ion concentration cell predominates. This necessarily may cause high dissolution around the periphery of the pits while at the same time slowing down the reaction inside the pit. This may explain the shallow trenched structure found on Monel. But it does not throw any more light on the conditions under which the shallow pits form in preference to the deep pits.

There is as yet no agreement on the mechanism of dissolution of Monel in aqueous environments. This may be the consequence of there having been few or no systematic studies of the dissolution mechanism of this alloy in aqueous solutions. LaQue[26] has discounted the dissolution redeposition type reaction mechanism in seawater on the grounds that redeposition of copper is not favored because nickel-copper alloys are slightly more noble than copper in seawater. He cited the work of C.F. Nixon[55] to support this point of view. In that study, Nixon subjected Monel specimens to tests used in studying dezincification of brass and found no evidence of selective dissolution.

LaQue's argument ignores changes in environmental variables such as flow rate, composition, temperature, etc., and hence ignores kinetic factors which may bring about slight changes in the scale of potentials. Denickelization of Monel has been reported[52,56,57] in other environments. Urgansky[56] analyzed the corrosion of Monel-400 alloy well screen in high CO_2 well water using electron probe microanalysis. They identified a second phase in the grain boundaries to be essentially pure copper with little or no nickel. Their conclusion, therefore, was that Monel-400 may be susceptible to dealloying (denickelization) when used in certain environments. Takasu et al.[52] analysed the surface of electropolished Cu-Ni alloys using Auger Electron Spectroscopy (AES) and X-ray Photoelectron Spectroscopy (XPS or ESCA). AES analysis showed that the surface content ratio of nickel to copper on specimens electropolished at potentials below the pitting potential was close to the bulk ratio. But the ratio at potentials where pitting was observed revealed slight enrichment of copper. They suggested that the enrichment probably resulted from preferential dissolution of nickel.

In another analysis of failures of a number of cupro-nickel and Monel exchangers exposed to brackish cooling water from the Delaware River, Bird and Moore[57] found evidence of denickelization in Monel condenser tubes. As with the failed cupro-nickel tubes in the same system, their analysis revealed copper plugs in the corrosion pits on Monel. The above observations may indicate that the dissolution mechanisms of Monel during pitting may be different from that occurring during general corrosion.

McIntyre et al.[46] employed XPS to study the aqueous oxidation of Monel-400 at 558K (285°C). They exposed the alloy to both oxidizing and reducing conditions in the pH range between 10 and 14. They reported that the aqueous oxidation of Monel was, under their experimental conditions, partly controlled by a dissolution precipitation mechanism.

Commercial Monel alloy is not just a binary alloy of nickel and copper. Other elements such as manganese (up to 2 w/o), iron (2% max.), carbon and silicon may also be present. Available literature gives no indication of whether these elements are merely incidental elements or whether they are deliberately added to improve mechanical and/or some physical properties of the alloy. As for their influence on the corrosion behavior on Monel, nothing of significance could be found regarding the presence of carbon and silicon. The beneficial effect of iron on the corrosion resistance of copper-rich copper-nickel alloys is well established.[26, 58-63] This effect was first reported in England[58] in a publication issued by the British Non-Ferrous Metal Research Association. In this report it was indicated that increasing the iron and manganese content of 70% Cu - 30% Ni alloy produced a corresponding increase in the resistance of this alloy to impingement corrosion. The report noted that, for optimum performance, increasing the manganese content required corresponding decrease in iron content such that the sum of the iron and one-fifth the manganese content should be equal to or greater than 0.5%. An iron content of between 0.3 and 1% and a manganese content of between 0.2 and 2% were quoted as needed to provide the observed effect.

To check the conclusions of this publication, LaQue[26, 59] and his co-workers investigated the effect of minor constituents on the behavior of cupro-nickel alloys in seawater. Their findings confirmed the British report. They found in addition that the amount of iron needed to improve resistance to impingement corrosion was not detrimental to the resistance of the alloy to corrosion by seawater under other conditions of exposure. Figure 10 shows their data on the effect of iron content. As can be seen from the figure, iron showed its strongest influence as its content was increased to 0.20%. Thereafter its effect was more gradual. Manganese was observed to show general improvement but its effect was less pronounced than that of the iron.

Tracy and Hungerford[60] also studied the effect of iron additions to cupro-nickels in a 3% solution of Turk's Island sea salt. The beneficial effect of iron was also proven in their tests. The tests were conducted in a vertical and horizontal-shaft impingement testers. Their data indicated that decreasing the amount of nickel in the alloy required increasing iron content for optimum performance of the alloy. Bailey[61] used a different form of impingement test to investigate the effect of iron content. In this test, jets of recirculated seawater containing 3 volume % entrained air flowing at a velocity of 15 fps were allowed to impinge on the specimens. Oxygen deficient conditions were simulated in some of these tests by burying the specimens under loose deposits of sand in quiescent seawater. In addition to confirming the beneficial effect of iron as reported in earlier studies, his results also indicated that iron contents of the order of 1.0% or more increased the susceptibility of 70-30 cupro-nickel alloy to pitting attack at shielded areas. He also noted that the higher the iron content in solid solution the greater is the increased corrosion resistance of the alloy to aerated seawater. He observed, however, that the maximum concentration of iron

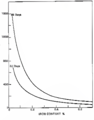

Figure 10 Effect of iron content on corrosion resistance of 70-30 cupronickel condenser tubes (velocity 20 fps, 50°F) (59)

needed to confer optimum beneficial effect in aerated seawater may be detrimental to the performance of 70-30 cupro-nickel alloy if conditions of exposure are such that local oxygen deficiencies exist. Under these conditions local film breakdown occurs and rapid pitting ensues.

In another study Stewart and LaQue[62] studied the corrosion resisting characteristics of iron modified 90:10 cupronickel alloy. In this investigation, specimens previously subjected to various heat treatments to either retain iron in complete solid solution or to precipitate iron-rich phases were exposed to salt water. The objectives of this study were, among other things, to determine whether iron is more beneficial in solutionized form or in a precipitated form. Annealing treatments were carried out at 978 K (705°C) to precipitate out iron-rich phases and a quench after holding at 1203 K (930°C) for 8 hours to retain Fe in solution. The results of exposure tests at Wrightsville Beach, NC, for 300 days are shown in Fig. 11. Other than the fact that for the standard annual, a minimum corrosion is observed within the range of iron contents between 0.8% and 2.2%, all alloys showed good resistance. They reported that only in the case of 3.5% iron alloy did the quench to retain iron in solution conferred a slight beneficial effect as determined by weight loss. They also observed as did Bailey[61] that heat treatment had a definite effect on the color of corrosion product film on alloys containing 1.5% or more Fe. When Fe was in solid solution, a golden brown film typical of cupronickels in seawater was noticed; however, when iron-rich phase was allowed to precipitate out in the alloy, an outer black magnetic and non-adherent film that made the alloy magnetic, was found on the corrosion product

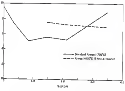

Figure 11 Effect of iron content on corrosion rate of 90-10 cupronickel in seawater (velocity 0-4 fps, 300 day exposure). (62)

For jet impingement tests, they reported no difference in resistance to impingement attack of alloys containing 1.5% Fe whether the Fe was in solution or in high iron content precipitate. For 2.0% Fe alloy quench annealing to solutionize showed improved resistance over the alloy that contained precipitated phases. They indicated that quench annealing was necessary to retain good resistance to impingement corrosion for iron content at the 3.5% level.

Figures 12 and 13 show the results of their test on the effect of the content and heat treatment on the resistance to conditions of a series of iron modified 90:10 cupronickels alloys. The tests were conducted at high velocities using rotating disc corrosion apparatus in seawater. As can be seen from the two figures, a continuous improvement in erosion resistance as the iron content was increased was observed. In both the tests done at 15 fps and 30 fps it was determined that alloys containing Fe in solid solution (Fig. 12) showed greater resistance to erosion corrosion above about 1% iron content than alloys heat treated to precipitate iron-rich phase (Fig. 13). The observed beneficial effect of solutionized Fe was in agreement with the result of later study by Swartzendruber and Bennett.[63]

According to this and the work of Bailey[61] there appears to be a suggestion that the beneficial effect of iron is in the protective film that forms on the alloys. However, others have provided a different explanation of the role of iron content in the increased corrosion resistance of Fe modified cupronickel alloys. North[64] first suggested that ferrous ions in solution were oxidized to hydrated ferric oxide or lepidocrocite (FeOOH), which electrophoretically deposited at cathodic sites.

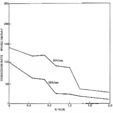

Figure 12. Effect of iron content on the corrosion rate of 90-10 cupronickel alloys rotated in seawater (73°F) at 15 and 30 fps for 55 days Heat treatment-quenched from 900°C. (62)

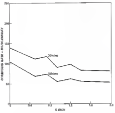

Figure 13 Effect of iron content on the corrosion rate of 90-10 cupronickel alloys rotated in seawater (73°F) at 15 and 30 fps for 55 days. Heat treatment-quenched from 900°C, 0.01-0.95% Fe held at 550°C for 2 hours, 1.19-1.96% Fe held at 600°C for 2 hours. (62)

The deposited film provided the increased corrosion resistance by polarizing or decreasing oxygen reduction reactions. Later studies by North and Pryor[65,66] and Gasparini et al.[67] led to the same conclusion.

However, this interpretation neither explains the iron composition requirement nor the observed difference in the beneficial effects of solutionized Fe versus precipitated iron-rich phase. This suggests that another mechanism may be operative under some other conditions. In a later paper, North and Pryor[68] proposed another mechanism based on the doping of defective Cu_2O by alloy additions. They indicated that incorporation of nickel into the defective Cu_2O lattice effectively dopes the Cu_2O film. The corrosion film thus doped, they suggested, had increased resistance to ionic transport at anodic sites and electronic transport at cathodic sites. They pointed out that Fe could show similar doping effect.

Popplewell et al.[69] carried out an investigation to clarify the role of Fe in the improved corrosion resistance of iron modified 90/10 cupronickel alloys. They corroded their samples in glass beakers containing air-saturated 3.4% by weight NaCl solution at 298 K (25°C). They performed weight loss and linear polarization measurements. Standard x-ray and electron diffraction techniques for corrosion product film analysis were used. They also found that in quiescent 3.4% NaCl solution, corrosion rate decreased with increasing Fe content and that both precipitated and solutionized Fe were effective. In their film analysis, they found that Cu_2O was present on all alloys. Overlying this film was another film identified to be $Cu_2(OH)_3Cl$. They explained that the presence of Fe ions provided additional doping of Cu_2O film which led to increased corrosion resistance of the alloys containing Fe in solid solution. They concluded that alloys containing 1.5% Fe in precipated form derived their increased corrosion resistance from the presence of a complex Fe phase overlaying the Cu_2O film.

Recently, Pickering and others[70] studied the mechanism of corrosion of Cu-9.4Ni-1.7 Fe alloy in air-saturated 3.4 wt% NaCl solution at room temperature. Before and after the corrosion period, they measured the weight of the specimens, the weight of the corrosion film as well as the cathodic and anodic polarization curves. They attributed the observed decreased overall corrosion rate largely to a decrease in the reduction of oxygen on the protective corrosion product layer on the alloy. They reported that the film consisted of two layers, a strongly adherent inner layer and a thicker porous outer layer. According to these authors, the oxygen reduction reaction occurred almost entirely on the thin inner layer with the transport of electron through this film the rate-determining step.

In continuation of this study, Pickering et al.[71] determined the composition of the protective surface both under natural corrosion and potentiostatic conditions. ESCA (or xps) Scanning Electron Microscopy (SEM) and x-ray diffraction were utilized in this later investigation. They[71] identified a thick outer layer to comprise essentially of $Cu_2(OH)_3Cl$ and a thin inner layer containing appreciable amounts of chloride, oxygen, copper and some nickel. They found the inner layer to be poorer in nickel and iron than the outer layer. If, as they concluded in their earlier paper,[70] the decrease in the overall corrosion rate is due essentially to the decrease in oxygen reduction kinetics on the inner layer of the protective film, and if, as they have observed in the later study,[71] this inner film is poorer in nickel and iron, one might conclude from their results that iron content plays little or no significant role in the observed improved corrosion resistance of iron modified copper-nickel alloys. On the contrary, the beneficial effect of iron content in the corrosion resistance of these alloys is no longer in doubt.

Clarification of the role of iron in iron modified cupronickel alloys was approached from a different perspective at the University of Florida. P A. Parrish[72] used electrochemical hysteresis techniques, developed by Pourbaix and others,[73] to study the behavior of 90:10 cupronickel alloys containing 0.04 and 1.46% Fe. He developed the experimental potential versus pH diagrams for the alloys. The diagrams revealed that Fe content slightly contracted the potential region for general corrosion. Verink and Lee[74] also used this technique to determine the influence of soluble additions on the passive behavior of binary copper-nickel alloys in solutions with and without chloride. From their results they arrived at the following conclusions:

(a) The "immunity" potentials and the "rupture" potentials shift slightly to more noble values with optimum iron concentration in the alloys.

(b) The "rate" of formation and the relative "protectiveness" of the passive films is optimized with optimum iron concentrations in the alloys.

They determined the optimum iron content, under their experimental conditions to be 1.4 w % Fe for 90:10 cupronickel alloy, 1.2% for 80:20 cupronickel alloy and 0.8% for 70:30 cupronickel alloy.

It is evident from the foregoing discussions that iron and manganese exert definite beneficial influence on the corrosion resistance of copper-rich copper-nickel alloys, although the mechanisms by which they operate are yet to be established, and although the question of whether Fe should be in solid solution is still not satisfactorily resolved in the literature.

Questions regarding similar influence of these alloying elements on the corrosion behavior of Monel-400 have still not been conclusively dealt with. LaQue[26] has made the observation that iron, manganese, silicon and carbon in the amounts normally encountered in Monel-400 have no significant influence on the corrosion resistance of this alloy This is contrary to the observation of Shiro Sato [51] Sato found from open-circuit exposure tests that the corrosion resistance of Monel metal containing 1-24% iron to oxygen-bearing water and steam was superior to that of pure Monel alloy

Kiyoshige and Yamane[45] used potentio-dynamic method to determine the effect of tertiary alloying elements on the dissolution behavior of some nickel-copper alloys. They also reported that the polarization curves for alloys containing Fe and Mn were slightly different from those of the binary alloy They observed that Fe and Mn contents affected only cathodic polarization. This observation is similar in some respects to the reported effect of Fe content in cupronickel alloys.

Unlike situations regarding cupronickel alloys, the studies of the effect of these alloy additions on the corrosion behavior of Monel are relatively few. As a result, unambiguous determination of the role of Fe and/or Mn content either in solutionized or precipitated form in the corrosion resistance of Monel-400 alloy is yet to be determined.

2.3 Alloy Dissolution

When a single-phase alloy dissolves either by natural or electrically-induced corrosion, its mode of dissolution may be

1. The simultaneous dissolution of the component elements in proportions corresponding to their respective concentrations in the alloy; or
2. preferential dissolution of the less noble component(s) of the alloy leaving a film of the more resistant element(s) or a modified surface structure richer in the more noble metal(s).

The latter mode of dissolution, also variously known as parting, selective leaching or dealloying, has received far more attention than the former largely because of the controversy surrounding the mechanism by which the latter occurs.

The phenomenon of dealloying has been known since late 19th century when its incidence was reported by Calvert and Johnson,[75] Tilden[76] and Arnold.[77] Although some solutions were reported early in this century for specific dealloying problems,[78-83] the debate over the mechanism by which this form of corrosion occurs is still very much alive. There is a school of thought that maintains that the more electronegative element differentially leaches out, leaving a spongy mass of the more noble species on the corroding surface.[77, 83-97] Sometimes a new and stable modified alloy of intermediate composition richer in the more resistant metal(s) forms on the corroding surface. Others[76, 98-109] have expressed the opinion that the alloy dissolves as an entity followed by the redeposition of the more noble species. This mechanism, it must be noted, is rarely observed in any other alloys than those containing copper. Still others[110-120] contend that both mechanisms are operative depending on experimental or exposure conditions. It was Verink and Heidersbach[115] who defined the conditions of potential and pH under which each mechanism may operate.

Although the phenomenon of dealloying was initially associated with loss of zinc from brasses (dezincification), selective removal of other elements from their respective alloys is now known. For instance, loss of aluminum from copper alloys,[96,110,121-127] denickelization of Cu-Ni alloys,[52,56,57,84,85] loss of iron from cast iron,[128] and cobalt from stellite[129] have been observed. Also, destannization (loss of tin) of copper alloys,[130,131] loss of copper from Cu-Au alloys,[89,93,94,132-136] and more recently, selective removal of Mg from Cd-Mg alloys[86] and Mn from Cu-Mn alloys,[137] have been reported. Loss of zinc from indium-zinc alloy[138] has also been reported.

In 1967, Pickering and Wagner[93] proposed the necessary thermodynamic conditions under which preferential dissolution would occur. These conditions are that

1. The difference between the electrode potentials of the component metals in the electrolyte should be large, several times greater than RT/F;
2. the electrode potential of the dissolving alloy should be more noble than that of the more active metal and "significantly" lower than that of the more resistant element.

These authors further defined the electrochemical conditions under which the ionization-redeposition mechanism would operate. Their theoretical analysis was based on the dealloying of Cu-Zn according to the following reactions

$$\mathrm{Zn\ (Cu\text{-}Zn)} = \mathrm{Zn}^{2+}\ \mathrm{(aq)} + 2e \qquad [7a]$$

$$\mathrm{Cu\ (Cu\text{-}Zn)} = \mathrm{Cu}^{n+}\ \mathrm{(aq)} + ne \qquad [8a]$$

$$\mathrm{Cu}^{n+}\ \mathrm{(aq)} + ne = \mathrm{Cu}^{\circ}\ \text{(nearly pure)} \qquad [9a]$$

Assume, as they did, that the ionization reactions, [7a] and [8a] are not coupled and each occurs independently of the redeposition reaction [9a]. From Nernst equation the single electrode potential for the above reactions is determined thus

$$E_{\mathrm{Zn}}\ \mathrm{(Cu - Zn)} = E^{\circ}_{\mathrm{Zn}} + \frac{RT}{2F} \ln \frac{a_{\mathrm{Zn}^{2+}}}{a_{\mathrm{Zn}}\ \mathrm{(Cu\text{-}Zn)}} \qquad [7b]$$

$$E_{\mathrm{Cu}}\ \mathrm{(Cu\text{-}Zn)} = E^{\circ}_{\mathrm{Cu}} + \frac{RT}{nF} \ln \frac{a_{\mathrm{Cu}^{n+}}}{a_{\mathrm{Cu}}\ \mathrm{(Cu\text{-}Zn)}} \qquad [8b]$$

$$E_{\mathrm{Cu}}\ \text{(nearly pure)} = E^{\circ}_{\mathrm{Cu}} - \frac{RT}{nF} \ln \frac{a_{\mathrm{Cu}}\ \text{(nearly pure)}}{a_{\mathrm{Cu}^{n+}}} \qquad [9b]$$

where E° is the standard electrode potential, R is the gas constant, a, the activity, T, the absolute temperature and F is the Faraday constant. Since the activity of copper in the alloy is less than unity and that of the redeposited copper is approximately unity, the calculated electrode potential of copper according to reaction [8a] for a given Cu ion concentration is more noble than that according the redeposition reaction [9b]. Copper dissolution according to reaction [8a] must necessarily occur at potentials anodic to the equilibrium electrode potential calculated from [8b] and, to a larger degree, at potentials more anodic than the electrode potential for redeposition of copper given by equation [9a] Redeposition of the dissolving copper ions cannot, therefore, occur as long as the established electrode potential remains nobler than that given by [8b].

If, for reasons of thermodynamics, there is coupling between reactions [7a] and [9a], the equilibrium potential for the copper dissolution reaction [8a] will be shifted in the active direction and may attain values lower than the value for the cathodic deposition of copper. Consequently, any copper ions entering the solution as a result of reaction [9a] may be redeposited at copper sites according to reaction [9b]. The extent of copper adsorption and their subsequent aggregation via diffusion, driven by an activity gradient (activity of adsorbed copper > 1) determine the availability of copper sites.

This analysis has been faulted on the ground that it failed to account for the fact that dezincification of high brasses (brasses containing less than 15% zinc) had not been observed.[139] Recently, however, Finnegan[140] using differential reflectometry, provided evidence that dezincification does occur in high brasses, albeit the observation that the dezincification process in these brasses differs both in degree and kind from that in yellow brass.

It must be noted that the difference between the electrode potentials calculated from [8b] and [9b] for any given concentration of copper ions is very small except when the activity of copper in the alloy is very small (a_{Cu} (Cu-Zn) <<1). One wonders then if kinetic factors might not invalidate the argument for the occurrence or lack thereof of the ionization-redeposition process. One may also question the wisdom of labelling dissolution-redeposition process as a mechanism of dissolution since the deposition process occurs regardless of the anodic process occurring on the dissolving alloy and regardless of the source of copper ions in solution. What is required for the deposition to occur is that there be a high concentration of copper ions in solution greater than a critical value, as would occur under stagnant or slow-flowing conditions.

Of equal interest to scientists are questions regarding the transport mechanisms by which atoms of the less noble metal reach the interface and those of the noble species aggregate during selective dissolution. Two probable mechanisms have been discussed in the literature. These are

1. Aggregation of the atoms of the noble alloy constituent by surface diffusion;
2. movement of the atoms of the constituent elements in the solid phase by lattice (volume) diffusion.

The former mechanism was favored by Feller.[141] The driving force for this mechanism is activity gradient since adsorbed copper atom has an activity greater than unity while copper atoms (solid) with other nearest neighbor copper atoms have an activity of unity. While surface diffusion may account for the aggregation of the atoms of the more resistant element, it does not address the question of the transport of the dissolving species from the bulk (lattice) to the surface where they ionize. As Pickering and Wagner[93] pointed out, operation of the surface diffusion as the sole mechanism might lead to the formation of three-dimensional crystals of the more noble metal. Growth of these crystals in three dimensions could eventually result in the formation of a compact layer of the noble species. Consequently, the dissolution process would, in time, terminate.

The volume diffusion, on the other hand, was proposed by Pickering and Wagner,[93] who also provided experimental evidence for its occurrence in copper-gold alloys. These authors studied the transport mechanism operating in Cu-Au alloys during selective leaching of copper from the alloys. In their theoretical consideration, they discounted lattice diffusion via monovacancies on grounds that the diffusivity of a monovacancy at room temperature, reported to be 3 x 10^{-19} Cm^2/sec, was too low. Instead they contended that diffusion of copper probably occurred predominantly via divacancies which have much higher diffusivity, 1.3 x 10^{-12} Cm^2/sec. From their mathematical analysis of their experimental data they showed that, indeed, enhanced lattice diffusion controlled by divacancy transport was the most probable mode of transport.

One consequence of selective dissolution is that the planar solid-liquid interface becomes unstable during dissolution, resulting in local penetrations (pores) in the reacted or dealloyed layer. Pickering and Swann[142] using transmission electron microscopy resolved these local pores and put their diameters at between 200-300Å in Cu-25 a/o Au alloy. In a later publication Pickering and Kim[95] attributed the local breakdown of the planar surface to slow diffusion in the alloy. They observed that the pores were interconnecting and have composition gradients in their walls. They further observed that diffusion in the environment within the pore structure may on occasions control the rate of the dissolution process.

Frequently, multiphase alloys are employed in practical applications. Nonetheless very few publications on alloy dissolution consider heterogeneous alloy dissolution behavior.[143-146] It has been determined that for a dissolving heterogeneous binary alloy at any potential

$$i_A = i_x f_x + i_y f_y \qquad [10]$$

where i_A is the dissolution current for the alloy, i_x, i_y are partial currents for components x and y and f_x and f_y are surface area fractions for the component elements. The area fractions are assumed to be equal to volume fractions which can be calculated from weight compositions and the densities of the components. In arriving at relation [10], the phases are treated as simple galvanic couples in direct electrical contact. As in the case of homogeneous alloy discussed previously, it is assumed here also that each phase dissolves independently of the other.

The quantitative theory of heterogeneous alloy dissolution given in [10] was developed by Stern^{143} who studied the cathodic polarization on composite surfaces of known area relationships and known voltage parameters. For his experiment, he used Type 316 stainless steel and titanium couples. His results agreed well with the theoretical prediction of equation [10]. Steigerwald and Greene^{145} studied the dissolution behavior of heterogeneous Sn-Zn alloys of various compositions. They also found that their experimental results were consistent with the theoretical prediction of Stern's relation. They noted, however, that equation [10] would not apply to a heterogeneous alloy containing an active phase finely dispersed in a noble matrix. The problem is that because of rapid dissolution of the active phase, more of the matrix would be exposed and the area fraction of the matrix would be larger than calculated from weight composition of the elements. This problem is nonexistent if the active phase forms a continuous network or large isolated colonies.

CHAPTER III
EXPERIMENTAL

3.1 Equipment and Materials

Appendix 1 lists the major experimental equipment used in this study. Characterization of the alloy and details of sample preparation are discussed in Appendix 2. The description of the electrodes, the electrochemical cell and other electrochemical equipment used in this study is presented in Appendix 3. Details of electrolyte preparation and treatment before experiments are described in Appendix 4.

3.2 Experimental Procedure

3.2.1 Potentiokinetic Polarization Experiments

Potentiokinetic polarization was the principal experimental technique employed in this study. Earlier attempts to cathodically pretreat the samples in sulfate solutions before anodic polarization resulted in white chalky deposits on the electrode surface. For this reason, no cathodic treatment was carried out in Na_2SO_4 solutions. But potentiodynamic polarization was begun in the cathodic region at potentials about -100 mV lower (more negative) than the potential of zero current (rest potential). In NaCl solutions, the neutral electrode potential was held for 10 minutes at potentials 100 mV more cathodic than the rest potential before commencing potential scanning. In all cases potential scanning was not commenced until the collector electrode has attained a constant background current.

Initially, the central (Monel disc or ring) electrode potential was linearly swept through a preselected potential region while recording its current. This was followed by potentiokinetically sweeping the potential of the collector electrode while maintaining the central electrode potential at a given potential in the active dissolution region. The aim of this experiment was to determine redox potentials associated with the electroactive species (soluble reaction products of Ni, Cu, Fe and Mn) generated at the central electrode. Thereafter, the collector ring electrode potential was held at a potential in the diffusion-limited current region for the species of interest while the central electrode potential was either traversed through a predetermined potential region or potentiostated at a potential value of interest. The ideal electrode configuration would be to have as many collector ring electrode segments as there are different soluble species generated at the central electrode. This would permit simultaneous detection of each electroactive species leaving the central electrode by maintaining the potential of each collector electrode sector at potentials corresponding to the redox potential of that specie. Since the electrode used has a single collector ring it was necessary to carry out each experiment as many times as there were soluble species of interest. Preliminary experiments ruled out the presence of enough soluble iron and manganese reaction products in solution to be picked up by the collector electrode. Each experiment was, therefore, run in triplicate, one each for Ni^{++}, Cu(II) and Cu(I).

The influence of electrode rotation velocity, temperature, and chloride ion concentration on the electrodissolution of the alloy was determined both as they affected the central electrode and collector electrode currents

3.2.2 Potentiostatic Polarization

Potentiostatic polarization was employed in the following experiments:

a) Atomic Absorption Spectrophotometry (AAS)

b) X-ray Photoelectron Spectroscopy (XPS) or ESCA (Electron Spectroscopy for Chemical Analysis)

c) Auger Electron Spectroscopy (AES)

d) Scanning Electron Microscopy/Energy Dispersive X-ray Analysis (SEM/EDX)

The procedure followed in these experiments was to polarize the electrode for a predetermined time at fixed potentials in the anodic region after a quick step of the potential from a point 100 mV below the rest potential using the step function as the signal generator.

3.2.3 Atomic Absorption Spectrophotometric Experiments

The procedure used here was to potentiostatically polarize the central electrode at a fixed preselected potential in the anodic region for times ranging from 30 minutes to 2 hours. Samples of solution were taken in 50 ml aliquots for each potential investigated. The concentration of each of Ni, Cu, Fe and Mn in the aliquot was determined using an atomic absorption spectrophotometer (Perkin Elmer Model 460).

The wavelength for each element and the limit of detectability of these elements for the instrument is given as follows: Ni: 232.0 nm, 0.15 ppm; Cu: 324.8 nm, 0.09 ppm; Fe: 348.3 nm, 0.12 ppm; and Mn 279.5 nm, 0.055 ppm. Air-acetylene flame type (oxidizing) was employed in the analysis. A hollow cathode was the light source. A blank correction was determined on sample electrolyte for each suspected element and subtracted from actual measurement, where applicable.

3.2.4 ESCA Analysis of Insoluble Dissolution Products

Disc specimens of radius 0.50 cm and height 0.47 cm were degreased and polished as described in Appendix 2 before they were masked with heat-shrinkable Teflon, leaving an exposed area of 0.78 cm^3. After the final polishing, the samples were anodized potentiostatically for various times at various potentials in the manner described in section 3.2.2. The specimens were then withdrawn from the polarization cell after each experiment without turning off the applied potential until the sample was outside the electrolyte. They were then washed in deaerated demineralized water, dried in nitrogen gas and then stored in a desiccator until needed for analysis. The Teflon mask was removed before the samples were introduced into the analysis chamber of the XPS apparatus. The theory of XPS Analysis is summarized in Appendix 5.

A Kratos X-ray photoelectron spectrometer (Model X-SAM-800) equipped with sputter-etching capability was used for this experiment. The starting sample analysis chamber pressure was maintained at 1.31 x 10^{-6} Pa (1 x 10^{-8} Torr) or better. Mg-Ka X-radiation at an energy of 1253.6 eV (0.70 eV line width) from a source operated at 240 W (13 kV, 20 mA) impinged on the sample in a broad beam (low magnification mode of operation). Photoelectrons emitted at about 75° to the X-ray beam were selected by a slit system and energy analysed in a hemispherical electrostatic energy analyzer operated in the fixed retarding ratio (FRR) mode. Operation in this mode was chosen because semi-quantitative data treatment was contemplated.

The analyzer field was set to pass only electrons of energy 60 eV or less. The energy analyzed electrons were detected by a windowless channeltron electron multiplier operating in the pulse counting mode and the signal produced stored in the memory of a PDP-11/23 computer. The ESCA spectra were taken for Ni 2p, Cu 2p, Fe 2p, Mo 2p, Cl 2p, O 1s and C 1s. The binding energy scale was referenced to the impurity carbon 1s line (285.0 eV). Where applicable, sputter etching of the sample surface was accomplished at an argon pressure of 2.50 x 10^{-2} Pa (1.90 x 10^{-4} Torr) using a Perkin Elmer differential ion gun (Model PHI 04-303). Etching was done for 10 minutes at 5 KeV power with argon ion flux of 5 uA-Cm^{-2}. This ion current was chosen to minimize decomposition of the film and preferential sputtering[46]

3.2.5 Auger Electron Spectroscopic Analysis

For this experiment, the rotating disc electrode (RDE) was used. The anodic polarization was conducted as described in section 3.2.2. Following anodization, the specimen was withdrawn from the polarization cell after each experiment without turning off the applied potential. The power was turned off after the sample was outside the solution. The sample was then washed in deaerated demineralized water and dried with acetone spray. It was then immediately placed in a nitrogen atmosphere and carried to the Auger equipment

Auger analysis (see Appendix 6 for theory of analysis) was carried out using a cylindrical mirror analyzer (CMA) mounted coaxially with the electron gun (Perkin Elmer Model PHI 10-150). The analysis was coupled with argon sputtering for profile analysis of elemental composition. The analysis chamber was evacuated to a starting (base) pressure of 1.33×10^{-6} Pa (1×10^{-8} Torr) or lower. Measurements were made with the electron gun operating at 3 KeV and with a primary beam current of 37 uA. The angle of incidence was about 45 degrees from normal to the sample surface

The procedure followed was to obtain surface survey scan after which the power to the electron gun was cut off. Following backfilling of the chamber with argon to a pressure of 5.30×10^{-3} Pa (4×10^{-5} Torr), both the electron gun and ion gun (3 KeV Varian scanning ion gun Model 981-3043) were turned on. The analysis was done simultaneously with ion sputtering. The ion gun was operated at 2 KeV with an emission current of 30 mA. The spectra were recorded in differential mode. Peak-to-peak height, measured for each element of interest, was plotted as a function of sputtering time to show any changes in chemical composition as a function of film thickness

3.2.6 Scanning Electron Microscopic (SEM) Characterization of Corrosion Product Morphology

A rotating disc electrode tip modified to fit into the SEM sample holder was used for this experiment. After polishing and washing thoroughly, the electrode was polarized at OV for 24 hours to develop good corrosion morphology. The sample was taken out of the corrosion cell, dried and stored in a desiccator until it was needed for examination. A JEOL (Model JMS 35C) scanning microscope was used in the secondary electron imaging mode at 25 KV for the morphological examination. Selected areas on the specimen surface were examined at different magnifications. Micrographs of these areas were obtained.

Attached to this microscope is an EG and G EEDS II Economical Energy Dispersive X-ray System. This equipment is capable of identifying and quantifying chemical elements by means of X-ray energy spectroscopy. The solid state (SiLi) detector for this system is mounted on the electron column of the SEM.

Bombardment of the atoms of the sample by 25 KV electrons caused the atoms to emit X-rays at their respective characteristic energy levels. The X-rays were absorbed by the detector operated at a bias voltage of 1 KV. Each event sensed by the detector generated a pulse that was amplified and measured by the multi-channel analyzer. Data for this experiment were collected over a time interval of 200 seconds and stored in the analyzer as an accumulated spectrum of number of events measured. A nominal energy range of 0 to 10 KeV (resolution 10 eV/Channel) was selected corresponding directly to 1024 memory channels. Point analysis (electron beam fixed at a position) was employed.

Three data acquisition modes are possible with the EEDS II equipment. These are (1) energy spectrum acquisition; (2) elemental distribution mapping; and (3) single-element line scans. Energy spectrum acquisition was the mode employed in this study. Data were collected on the sample surface at four locations: in the pits, on the star-shaped crystals, on a brown corrosion product, and on the dendrite-like structure overlying the brown film.

The spectrum of acquired data was displayed on a color video display system as peaks corresponding to count levels for specific elements in the analyzed sample. Element identification was accomplished with the aid of a cursor line and KLM markers. The cursor line extends from the top of the display to a point just above the count level. The cursor is movable across the screen to locate any channel. The KLM markers extend from the baseline into the spectrum. These markers appear in line energies representing a given element. After element identification, the channels displayed on the screen were plotted on an x-y plotter in linear scale as number of counts as a function of energy (KeV). Data were also obtained in another form. Through the aid of a computer program, elemental ratios of elements present in a spectrum were obtained. This was accomplished by setting the cursor on the regions of interest for the reference element. The program then determined ratios of net counts in the other regions of interest to the reference region. The results were given in a tabular form.

CHAPTER IV
RESULTS AND DISCUSSION

4.1 Anodic Polarization in Deaerated Na_2SO_4 Solutions

4.1.1 Linear Sweep Voltammetry

Figure 14 is a cyclic voltammogram for Monel-400 alloy disc in deaerated 0.5 M Na_2SO_4 solution, pH ≅ 2, obtained under static conditions. The potential sweep rate was ≅ 10 mV/sec. The voltammogram exhibits active, passive and transpassive regions as is characteristic of this alloy in most aqueous solutions. The arrows on the graph indicate the direction of polarization. A cathodic current maximum is observed at about -100 mV on reversal of potential sweep. The increase in cathodic current at this point may be due to either the reduction of soluble dissolution products or the reduction of the anodic film on the sample surface.

The possible reactions occurring in the active region are the following:

$$\text{Cu (Monel)} \rightarrow Cu^{+}_{aq} + e \qquad [10]$$

$$\text{Cu (Monel)} \rightarrow Cu^{2+}_{aq} + e \qquad [11]$$

$$\text{Ni (Monel)} \rightarrow Ni^{2+}_{aq} + 2e \qquad [12]$$

$$\text{Ni (Monel)} \rightarrow NiOH^{+}_{aq} + e \qquad [13]$$

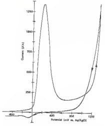

Figure 14 Anodic potentiokinetic polarization curve for Monel-400 alloy in deaerated Na_2SO_4 at 298K (25°C), pH 8.2. Sweep rate (S) = 0.33mV 1 sec; electrode rotation speed (w) = 0 rpm

$Fe\ (Monel) \rightarrow Fe^{2+}aq. + 2e$ [14]

film forming reactions (direct oxidation of component metals to compounds)

$Cu^{2+}aq. + e \rightarrow Cu^{+}aq$ [15]

Reaction [15] could occur if the following conditions are met

1) reaction [12] occurs;
2) products of reaction [12] are allowed to accumulate at the interface; and
3) the potential of the corroding sample is maintained at a potential below the redox potential for the couple Cu^{2+}/Cu^{+}

4.1.2 Characterization of Soluble Reaction Products

In the analysis of corrosion behavior of any material, it is of interest to characterize reactions in the active region with respect to reaction kinetics as well as to the nature of reaction products. There are at least two major reasons for this. The first is that reaction kinetics in this region determine the onset of passivity while the nature of the reaction product controls the degree of passivity to which many engineering materials owe their corrosion resistance. Secondly, knowledge of the products of these reactions makes it easier to infer mechanisms and thus facilitate implementation of corrosion control measures.

Incorporation of a collector ring around a central electrode which can be independently potentiostated enables in situ analysis of soluble reaction products. This electrode configuration was used in order to monitor the various soluble reaction products generated at the central Monel-400 electrode. Figure 15 shows the potentiodynamic polarization curve for a glassy carbon collector ring electrode displaying potential regions where soluble dissolution products could be monitored. The dissolving Monel-400 potential was maintained at +150 mV as the collector ring potential was scanned from +800 mV to −800 mV back to +800 mV. The figure shows that the soluble dissolution products generated at the central electrode could be monitored only by reduction at potentials below (more negative than) +100 mV. The anodic current observed on reversal of potential sweep is due to dissolution of the electrodeposited product(s).

The implication of this observation is that no species generated from Monel at +150 mV is reducible or oxidizable at potentials above +100 mV. Although this experiment has indicated that soluble species were indeed generated at the corroding Monel-400 electrode, the information from the experiment is not sufficient to permit identification of specific species. A knowledge of the redox potential for each species is needed to carry out additional experiments that will allow the establishment of its presence.

The redox potentials for possible soluble dissolution products determined in separate experiments described in Appendix 7 are reported in Table 2. With these data, the presence or absence of an electroactive species could be established by maintaining the collector electrode at a suitable potential where the species of interest could be detected either by oxidation (above the redox potential) or by reduction (below the redox potential)

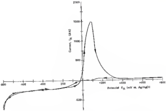

Figure 15. Potentiokinetic polarization curve for glassy carbon collector electrode showing potential regions where soluble reaction products could be monitored, Monel-400 electrode held at +150mV; Deaerated Na_2SO_4, pH 8.2, 298K (25°C) S = 0.33mV/sec; w = 1600rpm.

Table 2. Redox Potentials of Possible Soluble Anodic Corrosion Products of Monel Alloy 400

Fe^{+2}/Fe^{+3}	+ 600 mV	(AG/AGCL)
Cu^{+}/Cu^{+2}	+ 300 mV	
Cu^{+}/Cu	- 200 mV	
Ni^{+2}/Ni	- 250 mV	

*This is not pure redox potentials as they have been determined potentiakinetically from solutions containing these species in concentrations much less than 1 M.

The results of experiments in which the potential of Monel-400 central electrode was linearly swept from -800 mV to +800 mV while the collector electrode was simultaneously potentiostated at +400 mV and +800 mV, respectively, are presented in Fig. 16. By maintaining the collector electrode at +600 mV, any cuprous ions in solution would be detected by oxidation to cupric ions. Similarly, any ferric ions in solution would be reduced to ferrous ions at the same collector electrode potential. The collector electrode was potentiostated at +800 mV in order to oxidize any ferrous ions generated at the central electrode to ferric ions.

The absence of anodic or cathodic waves in Fig. 16b indicates that these ionic species (Cu^{+}, Fe^{2+} and Fe^{3+}) were not in solution. Several explanations are possible;

1) the ions were not generated at the dissolving electrode in the potential range investigated;
2) the concentrations of these species were too low to be detected by this technique ($< 10^{-7}$ M);
3) the species formed insoluble corrosion products and were retained on the surface of the dissolving electrode;
4) cuprous ions were not stable in this environment and were reoxidized to cupric ions as soon as they were generated;
5) the cuprous ions underwent disproportionation reaction to form Cu and Cu(II) ions

The disproportionation reaction(s) may be unlikely on, at least, two grounds. First, cuprous ions were not detected at all electrode

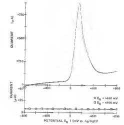

Figure 16 Potenickinetic polarization curve for Monel-400 alloy in deaerated 0.5M Na_2SO_4, pH 8 2 at 298K (25°C). a) central electrode current, b) collector ring current. S - 8 33mV/sec; w = 1600rpm. Absence of structure in collector ring current confirms absence of Cu^+, Fe^{2+} and Fe^{3+} ions.

rotation speeds investigated, up to 4000 revolutions per minute (r.p.m.). The argument is that as the rotation speed is increased the residence time of the cuprous ions in contact with copper atoms on the surface is proportionately decreased. It is conceivable that at some rotation speeds enough cuprous ions would escape the disproportionation reaction and be picked up at the collector electrode. Secondly, a Monel-400 central ring electrode is used in this study as against the traditional disc electrode to minimize the surface area of the dissolving electrode. This necessarily would minimize the extent of disproportionation reaction. Premise number 4 makes little sense in that if Cu(I) is unstable in this environment, why should it form in the first place? This is a subject of another test described later in this section. As for premises 1 to 3, each is capable of explaining the results presented in Fig. 16b.

To test for the presence of cupric ions in solution, the collector electrode potential was held at -150 mV while the central electrode potential was traversed from -800 mV to +800 mV (Fig. 17). The cathodic wave shown in Fig. 17b establishes the presence of Cu(II) in solution, and is due to the reduction reaction

$$Cu^{2+}aq. + e \rightarrow Cu^{+}aq. \qquad [16]$$

This result, however, throws very little light on the mechanism by which the Cu(II) is generated. The literature is divided on this point. Some authors[147-149] contend that the reaction proceeds via cuprous

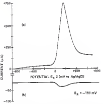

Figure 17 Potentiokinetic polarization curve for Monel-400 alloy in deaerated 0.5M Na_2SO_4, pH 8.2 at 298K (25°C): a) Monel-400 current; b) collector ring current, collector electrode -150mV. S = 8.33mV/sec; w = 1600 rpm.

ion intermediate according to the following reaction path:

$$\mathrm{Cu} = \mathrm{Cu}_{\mathrm{ads.}} = \mathrm{Cu}^{+}\mathrm{aq.} + e = \mathrm{Cu}^{2+}\ \mathrm{aq.} + e \qquad [17]$$

The argument in support of this reaction path, advanced by Mattsson and Bockris,[147] is that it is more difficult to discharge Cu(II) ions because of the greater heat of hydration of Cu(II). No experimental evidence exists today to support this reaction pathway.

Others[150-153] have favored one step reaction path involving simultaneous transfer of two electrons. Hurlen[150] investigated the anodic dissolution and cathodic deposition of copper in acidic sulfate solution by means of a slow amperostatic technique. He came up with the following mechanism of dissolution

$$2\mathrm{Cu} = 2\mathrm{Cu}^{2+}\mathrm{aq.} + 4\ e \qquad [18]$$

In another study, Hurlen and Londe[151] used radiotracer technique to determine the mechanism of dissolution of copper. They found no evidence for Cu(I) intermediate. Lorenz[152] employed impedance measurements on copper in acidified cupric solutions. He also found no evidence for intermediate generation of Cu(I).

However, results from this laboratory, Fig. 18, as well as others reported by other investigators[154-159] furnish direct voltammetric evidence for a two-step reduction of Cu(II) to Cu(0) via Cu(I) intermediate. The data presented in Fig. 18, do not, however, prove

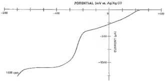

Figure 18. Cathodic reduction of Cu(II) ions on a rotating carbon disc electrode. Deaerated 0.5M Na_2SO_4 solution, pH 8.2, containing 10^{-3}M Cu^{2+} ions. S = 20mV/sec.

conclusively, as they stand, that generation of Cu(I) is an intermediate step in the reduction of Cu(II). What they show is that by linearly scanning the voltage from an anodic end to a point in the cathodic region where copper plating occurs, a potential region is traversed at which Cu(II) is reduced to Cu(I). One cannot tell from the data whether Cu(II) is not reduced directly to Cu(0) below this potential region

Confirmation of the existence of Cu(I) intermediates in the deposition to Cu(0) from Cu(II) solutions necessarily requires another test An experiment was carried out in Na_2SO_4 solution initally containing 1 x 10^{-5} M Cu^{2+} aq ions The potential of the glassy carbon disc electrode was stepped from +800 mV, where no reaction involving Cu(II) ions in solution occurs, to -500 mV, where copper plates out. The potential of the collector electrode was held at +600 mV in order to detect Cu(I) ions (by oxidation) generated at the carbon disc during the intermediate reaction step. Both the disc current and the ring current were recorded simultaneously as a function of time. The results, shown in Fig. 19, proves conclusively that Cu(I) is a reaction intermediate in the reduction of Cu(II) to Cu(0). Tindall and Bruckenstein[156] and Taylor[158] used different procedures to arrive at the same conclusion.

Whereas, the evidence from these experiments and others cited here lend support to a two-step mechanism involving intermediate reaction producing Cu(I) in the reduction of Cu(II) to Cu(0), it calls into question the suggestion that a similar reaction path

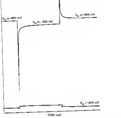

Figure 19. Current-time behavior; top: cathodic reduction of Cu(II) ions at -500mV (Ag/AgCl); bottom: oxidation of Cu(I) ions at +600mV (Ag/AgCl) w = 1600rpm

exists in the oxidation of copper in sulfate solutions. This experiment has demonstrated that the stability of cuprous ions in sulfate solutions is high enough for these ions to travel from points on the central electrode where they are generated to the collector electrode where they could undergo further reaction, such as oxidation to cupric ions. The fact that Cu(I) ions were not detected during the dissolution of Monel in sulfate solutions suggests that the intermediate reaction step, i.e., the generation of Cu(I) ions, in the ionization of Cu (Monel) may not exist in this environment. Based on the foregoing discussion, the following reaction mechanism is offered as the more probable kinetic unit reaction of Cu (Monel) dissolution in sulfate solutions containing no complexing agents:

$$\text{Cu (Monel)} \rightarrow \text{Cu}^{2+}\text{aq} + 2\text{ e} \qquad [19]$$

For the detection of nickel, the only reaction possible is the reduction of nickelous ions to elemental nickel according to the following reaction:

$$\text{Ni}^{2+}\text{aq.} + 2\text{ e} \rightarrow \text{Ni}^{0} \qquad [20]$$

This analysis was attempted at a carbon electrode maintained at -700 mV while scanning the central electrode potential from -800 mV to +800 mV as shown in Fig. 20. In view of the fact the reduction of nickel takes place at potentials cathodic to the reduction of soluble

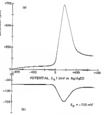

Figure 20. Potentiokinetic polarization curve for Monel-400 alloy in deaerated 0.5M Na_2SO_4, pH 8.2, at 298K (25°C); a) Monel-400 ring current, b) collector ring current. S = 8.33mV/sec, w = 1600rpm.

copper dissolution products Cu(I) and Cu(II) to Cu(0), independent analysis for nickel species is not possible using this technique because of interference from other species in solution. Since it has been shown that iron species were either not in solution or were not in sufficient concentration to be picked up by this technique, the current at -700 mV is due to the reduction of copper species and probably nickel species

An attempt was made to determine nickel current by difference, that is, subtracting twice the current due Cu(II) at -150 mV (one electron transfer) from the current at -700 mV (which involves two electron transfer). The difference is very small and cannot be assigned to nickel apriori for two reasons First, the increase in copper reduction current due to a larger over-potential (the difference in copper reduction current at -150 mV and at -700 mV) must be known. Secondly, and more importantly, the reduction efficiencies for copper and nickel depositions must be considered Although the experiment was begun initially with glassy carbon collector electrode, it was observed that within a short time of polarization the surface of the glassy carbon would be covered with deposited copper. Not only would the kinetics of reduction of copper and nickel change because of the change in the nature of the collector electrode surface (possibility of different exchange current densities for copper and nickel deposition on a carbon surface versus on a copper surface), but also hydrogen evolution reaction on the deposited copper became a possibility. These factors could account for the small difference. Because of this difficulty, the mode of dissolution, selective or simultaneous (the component elements going into solution in amounts proportional to their respective stoichiometries in the alloy), could not be established on the basis of these data alone.

To establish conclusively the presence or the lack thereof of nickel ions in solution, a separate experiment was conducted. The test involved solution analysis using atomic absorption spectrophotometry (AAS). The results, shown in Table 3, confirm that nickel ions were indeed generated during dissolution of Monel-400 alloy in sulfate solutions. In this experiment, as in the ring collection experiments, iron corrosion products could not be detected. One other interpretation that emerges from this experiment is that, nickel ions in the form generated, are difficultly reducible.

Results of an investigation conducted in a nickel sulfate ($NiSO_4$) solution (Appendix 7) suggest that reduction of nickel ions from their salt solution is much easier than has been experienced with soluble products of nickel dissolution. This is a strong indication that nickel probably goes into solution during electrodissolution in a form other than $Ni^{2+}aq$. The strongest possibility is $NiOH^+$ which has generally been regarded as a reaction intermediate in the anodic dissolution of nickel. Consequently, the following mechanism of nickel dissolution is proposed:

$$Ni\ (Monel) \rightarrow NiOH^+ + e \qquad [13]$$

As a result of the difficulty to reduce nickel dissolution products (soluble), no attempt was made to detect nickel products in subsequent experiments performed in this environment.

Table 3 Atomic Absorption Data From Potentiostatic Tests in Na_2SO_4 Solution at 298 K (25°C)

Potential of Polarization (Ag/AgCl)	Amount in Solution (PPM) Ni	Cu	Fe	Mn
Experimental Solution (blank)	nil	0.06	0.10	nil
+ 100 mV	0.10	0.08	0.10	nil
+ 250 mV	0.30	0.19	0.10	nil
+ 800 mV	nil	0.06	0.10	nil

4.1.3 Effect of Electrode Rotation Speed

In this experiment the electrode was rotated at various speeds in order to simulate different solution flow conditions and to determine the effect of flow rate on the corrosion behavior of this alloy. The importance of the influence of solution flow on the corrosion behavior of some materials has been recognized since 1910 when Heyn and Bauer[160] reported that increased solution flow velocity increased the corrosion rate of iron. This influence is strongly associated with mass transport of corrosion products away from, and reactive species to, the corroding surface. The resulting changes in interfacial concentrations may increase (concentration polarization) or decrease the over-potential requirements for anodic or cathodic reaction or both. The outcome may be an increase or a decrease of corrosion rate. Another dimension to solution flow effect is that associated with cavitation, erosion or impingement effects. The effects of these become significant when flow rate reaches a certain value which depends on solution composition and the type of metallic material.

Figure 21 demonstrates the influence of electrode rotation speed on the anodic polarization for Monel-400 alloy in 0.5 M Na_2SO_4 solution. The results show that as the electrode rotation speed is increased (increased solution flow velocity), the anodic peak current initially decreases up to 1600 rpm above which it begins to increase with increasing rotation speed. Plotted in Fig. 22 is the peak current as a function of the square root of rotation speed. The figure shows linear behavior on both sides of the minimum, indicating solution flow

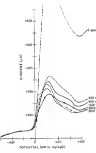

Figure 21. Potentiokinetic polarisation curves for Monel-400 in deaerated 0.5M Na_2SO_4, pH 8.2, at various electrode rotation speeds; 298K (25°C). S = 8.33mV/sec

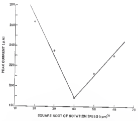

Figure 22 Anodic peak current as a function of the square root of rotation speeds. Deaerated 0.5M Na_2SO_4 solution, pH 8.2 at 298K (25°C); S = 8.33mV/sec.

dependence in both regions of rotation speed. Figure 23 demonstrates that the behavior of the current due to soluble copper reaction products follows the same trend as that of the total anodic current, hinting at the possible influence of copper dissolution kinetics on the corrosion behavior of Monel-400 alloy.

There are four possible explanations for this behavior. First is the additional cathodic reaction involving the reduction of generated cupric ions. According to the table of redox potentials (Table 2), cupric ions in solution are reducible to cuprous ions if the dissolving Monel-400 electrode is at any potential below +300 mV. This additional cathodic reaction forces more dissolution to occur in order to provide the electrons needed to maintain the reduction of Cu(II) ions. The higher the concentration of Cu(II) ions at the interface the higher the driving force for these reactions. As the rotation speed is increased the concentration of cupric ions is correspondingly decreased at the interface. The magnitude and driving force for the cathodic reaction, and hence the electron requirement, decrease. This may explain the decrease in the peak current with increasing rotation speeds.

There are many problems with this hypothesis. It cannot explain the behavior above 1600 r.p.m. Secondly, Hurlen[150] has determined that the rate of copper dissolution in acidic sulfate solutions is independent of cupric ion concentration. The most important argument against this premise is that cuprous ions, either generated directly during dissolution or as products of cupric ion reduction, were not monitored in the experiments designed to detect them (see Fig. 16b).

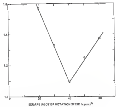

Figure 23 Normalized collector ring current as a function of electrode rotation speed; E_R = -150mV; Deaerated 0.5M Na_2SO_4, pH 8.2, at 298K (25°C); S = 8.33mV/sec.

Another possible explanation considered involves the effect of adsorption of sulfate ions on the electrode surface. Sulfate ions have been shown to adsorb at copper electrodes at potentials above (anodic to) -200 mV.[161] If similar phenomena occurs on nickel surfaces, this effect might explain the behavior at lower velocity region, since as the rotation speed is increased sulfate ions are brought to the interface faster. This hypothesis, also, cannot explain the behavior above 1600 r.p.m.

The most probable theory is the rotation speed dependence of the formation of insoluble reaction products. The formation of solid dissolution products may depend on how fast certain species in solution arrive at the interface. By increasing the rotation speed of the electrode (i.e. increasing solution flow rate) these species arrive faster, and increasing amount of solid reaction products form, covering more areas of the sample surface. The result may be the reduction of anodic current at increasing rotation speeds.

Formation of insoluble products could come about either by direct reaction of electronegative species in solution with surface atoms or by dissolution-precipitation mechanism. The probable solid reaction products are Cu_2O, CuO or $Cu(OH)_2$ and NiO, Ni_3O_4, Ni_2O_3 or $Ni(OH)_2$. Compounds of iron and manganese which are present in minor quantities may also be present. Any of these compounds could form either from H_2O or hydroxyl (OH^-) ions. Considering that the concentration of water is high and that of OH^- ions low (Ca. 10^{-6} M, pH 8.2), and that there is angular velocity dependence of transport, the OH^- ions are the more probable reactants. As for the mechanism of formation, direct oxidation cannot explain the current behavior in the high rotation speed region, unless the argument could be made that the increase in current in this region is due to another reaction step, such as transport of soluble dissolution products in the solution phase, becoming rate limiting.

A dissolution-precipitation mechanism may be used to explain the observed behavior. The model for this mechanism, proposed by Armstrong,[162] involves nucleation and growth and critical concentration of ions below which nucleation cannot occur. Not only does nucleation require concentrations higher than the critical values for the ions involved (supersaturation required for nucleation) but growth also demands steady supply of the ions involved in the precipitation. Conceivably, at the outset, because of high dissolution rate, the concentrations of these ions were above the critical values. Nucleation, therefore, would occur and the crystals would grow to critical values. Further growth of these crystals would deplete the solution surrounding the crystals. The direction of growth would be limited by transport of ions to the growth sites. Rotating the electrode would increase the supply. The faster the rotation velocity the faster is the transport of the ionic species and the higher the growth rate. This would cause larger areas on the electrode surface to be covered. This could explain the current behavior at angular velocities below 1600 r.p.m.

It should be noted, however, that increasing the flow velocity has the effect of decreasing the concentration of metallic ions at the interface because of decreased diffusion layer thickness and the increase in the concentration gradient between the anolite and the bulk solution. The tacit assumption in the foregoing argument is that the concentration of the metallic ions did not decrease below the critical value for nucleation at any rotation speed below 1600 r.p.m. Either of two things could happen at higher angular velocities to explain the increase of current in that region. Possibly, rotation speeds became so high that surface concentrations of metal cations drop below the critical concentration for nucleation. Nucleation and hence, precipitation, would not occur. Alternatively, the concentration continued to decrease at the interface, but not below the critical value even above 1600 r.p.m. Yet it became sufficiently low to limit growth rate. Either of these phenomena would cause active dissolution to occur at a higher rate.

In accordance with this theory, the following reaction scheme, omitting the transport steps, is proposed.

a) for Ni

$$Ni + OH^- \rightleftarrows NiOH_{ads} + e \qquad [1a]$$

$$NiOH_{ads} \rightarrow NiOH^+_{aq} + e \qquad [1b]$$

Accumulation of these species in excess of its solubility limit will result in precipitations according to the following reaction

$$NiOH^+_{aq} + OH^- \rightleftarrows Ni(OH)_2, \qquad [2]$$

according to Bockris et al.,[11] or

$$NiOH^{+}aq. \rightarrow NiO + H^{+} , \qquad [21]$$

according to Okamoto and Sato.[1,2,4] As admitted by both groups of workers, the final passivation film is different from the precipitated compound. Bockris et al.[11] suggested a final passive layer of composition $NiO_{1.5-1.7}$. Okamoto and Sato,[1,2,4] on the other hand, contended that either Ni_3O_4 or a duplex film of Ni_3O_4 and NiO was responsible for nickel passivation. McIntyre et al.,[46] however, with the aid of x-ray photoelectron spectroscopy technique, determined that the outermost corrosion product formed on Monel-400 alloy exposed to high temperature, high pH aqueous solutions was solely $Ni(OH)_2$. From the morphology of the film they concluded that it probably formed by dissolution-precipitation mechanism.

b] for copper, the possible precipitation reaction could be

$$Cu^{2+}aq + 2OH^{-} = Cu(OH)_2 \qquad [22]$$

Whether $Ni(OH)_2$ and/or $Cu(OH)_2$ predicted here exist in the passive region in this form or they are transformed to another form (as suggested by Bockris et al.[11] and Okamoto and Sato[1,2,4]) has been determined using an XPS technique. The results of this investigation are discussed in the next section.

Another probable theory is that the rate of anodic reaction is limited by the transport of electroactive species to, and away from, the reacting surface. It appears that the linear behavior in the low rotation velocity region is due to the transport of some electroactive species, probably OH^- ions, to the corroding surface becoming rate-limiting. This would explain the negative slope since transport is in the opposite direction. This is consistent with the hypothesis of Sato and Okamoto[17] that both the anodic dissolution and the onset and maintenance of passive condition depend strongly on the concentration of OH^- ions. In the high velocity region (above 1600 r.p.m.), transport of OH^- ions no longer controls anodic reactions since more of the ions are brought to the reacting surface faster. Instead, transport of the generated cupric ions away from the dissolving surface may limit the kinetics of anodic reactions in this region.

4.1.4 X-ray Photoelectron Spectroscopic Analysis of Passive Films on Monel-400 Alloy

The physical properties of the insoluble dissolution products (deposits) formed on the surface of the corroding metal determine whether subsequent corrosion reaction would continue with a constant or accelerated velocity or would gradually stop. The physical character of these products, therefore, is of equal significance to corrosion scientists as is the electro-chemistry of the corrosion process. In keeping with this observation, a concerted attempt has been made in this study to characterize the chemical composition of the insoluble corrosion product formed on anodized Monel-400 alloy surface. To this and, advantage is taken of the ability of the E.S.C.A. technique to provide chemical state information (i.e. oxidation state).

Presented in Figs. 24 and 25 are the photoelectron spectra for Cu ($2p_{3/2}$) and Ni (2p), respectively, obtained after anodization of Monel-400 alloy in the passive region. Spectral identification has been made on the basis of comparison of binding energy data obtained here and those in a handbook[163] and other references[46, 164-175, 178] (see Tables 4 and 5)

Shifts in binding energies for copper and its compounds are usually very small and are generally not reliable for spectral identification. However, strong satellites are always associated with Cu(II) spectra, appearing 6 - 10 eV on the low kinetic energy (high binding energy) side of the principal line energies of these compounds. These satellites have been used diagnostically to indicate the presence or absence of Cu(II). Cu(I) spectra show very weak, if any, satellite structures, while no satellite features are associated with Cu(0) spectrum.

The lack of satellite structures in Fig. 24 is strongly indicative of the absence of cupric compound on the surface of Monel-400 alloy anodized in the passive region. This is, at least, true within the depth sampled by the x-rays. The spectrum shown here (Fig. 24) therefore, belongs to either Cu(0) or Cu(I). Cu(I) is distinguishable from Cu(0) by shifts in the x-ray-induced Copper Auger LMM line, characteristic spectral features and Auger parameters.[46,163,167] Shown in Fig. 26 is the Cu $L_3 M_{4,5} M_{4,5}$ Auger electron spectrum. According to the Auger spectral data on copper and its compounds

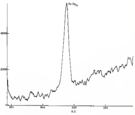

Figure 24: Cu(2p) x-ray photoelectron spectrum for Monel-400 alloy surface exposed to deaerated 0.5M Na_2SO_4, pH = 2, at 298K (25°C) for 0.5 hour

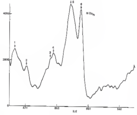

Figure 25. Ni (2p) x-ray photoelectron spectrum for Monel-400 alloy surface exposed to deaerated 0.5M Na_2SO_4, pH 8.2, at 298K (25°C) for 0.5 hour.

Table 4. Binding Energy Data for Copper and Copper Compounds

	Binding	Energy,	Ev		
Source	Cu	Cu_2O	CuO	$Cu(OH)_2$	CuCl
This work*	932.50	-	-	-	-
Reference					
46	932.40	932.40	933.70	934.20	-
164	932.50	932.50	933.50	-	-
164	-	932.70	933.60	-	-
165	-	933.00	-	-	932.50
166	-	932.20	933.60	-	-
167	932.20	932.10	933.00	-	-
168	-	932.50	-	-	-
169	-	934.70	936.20	-	-
170	932.50	932.50	933.80	934.40	-
171	932.47	932.50	933.70	934.75	-
172	-	933.10	934.50	-	-
173	-	933.00	934.30	-	-

*Datum obtained in sulfate solution.

Table 5. Binding Energy Data for Nickel and Nickel Compounds

Source	Binding Energy, Ev					
	Ni	NiO	Ni_3O_4	Ni_2O_3	NiO_2	$Ni(OH)_2$
This work*	852.60	-	-	-	-	856.10
Reference						
46	852.50	854.00	-	-	-	855.80
170	852.50	854.00	-	-	-	855.60
171	852.75	854.600	-	855.70	-	856.45
174	852.80	854.50	-	855.80	-	-
176	852.00	855.00	-	-	-	-
178	-	854.00	-	-	-	-

*Data obtained in sulfate solution.

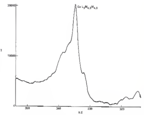

Figure 26. Cu $(L_3M_{4,5}M_{4,5})$ Auger spectrum for Monel-400 alloy surface exposed deaerated 0.5M Na_2SO_4, pH 8.2, at 298K (25°C)

published by Schon[167] and Windawi et al.,[178] the kinetic energy line at 919.0 eV in elemental copper spectrum has no correspondence in the spectra for the compounds. The principal peak at 919.9 eV (334.7 eV on the binding energy scale) in the spectrum of Fig. 26 corresponds to theirs at 919.0 eV. Additionally, the other resolvable peaks in the spectrum correspond, peak for peak, to the other peaks on their own spectra for Cu(0). On the basis of this comparison and the feature for feature correspondence, the spectrum shown in Fig. 26 has been identified as that of elemental copper. The implication of this is that, in the passive region and for the polarization time of 30 minutes, copper exists either in the film or on the surface of the anodized sample in elemental form.

The Ni(2p) spectrum presented in Fig. 25 shows a principal peak at 856.10 eV. On the basis of data in Table 5, the presence of nickelous hydroxide ($Ni(OH)_2$) on the anodized Monel-400 surface is strongly indicated. Although, the core line energy for $Ni(OH)_2$ is generally higher than that for nickel oxide (Ni_2O_3) (see Table 5), the difference is within experimental margin of error for this technique. Shifts in Ni LMM Auger (X-ray-induced) line energies and oxygen binding energies have been used to distinguish between the two compounds.[171,174] Auger spectrum for Ni was not obtained in the sulfate environment. An assignment based on shifts in oxygen line energy may be valid only when it involves a pure metal (e.g. Ni). For alloys such as Monel-400, in which both nickel and copper compounds may be involved, identification on the basis of shifts in oxygen core line energy is suspect unless shifts due to each component metal compound could be determined.

This difficulty does not exist for the work reported in this section since no copper compound exists in the film.

The $O(1S_{1/2})$ spectrum recorded in Fig. 27 has a line energy position at 532.1 eV. This value agrees with that recorded by Barr (531.55 eV)[171] for $Ni(OH)_2$, but slightly higher than that reported by McIntyre et al. (531.7 eV).[46] This also points more to the presence of $Ni(OH)_2$ than the presence of Ni_2O_3 which O(1S) line energy has been reported to be 531.7.[171] There is also a peak at 530.2 eV in the oxygen spectrum. This may be associated with weakly bound (adsorbed) oxygen resulting from exposure to laboratory atmosphere. McIntyre et al.[46] observed a similar peak at 531.7 eV and attributed it to the presence of minor concentrations of a surface oxygen species.

In addition to shifts in Auger and oxygen line energies, McIntyre et al. have used characteristic features (twin peaks 1.7 eV apart) on shake-up satellites to identify $Ni(OH)_2$ on Monel-400 alloy[46] and Inconel-600 alloy[176] corroded in high pH aqueous solutions. The principal binding energy line (arrow 5) of Fig. 25 corresponds closely to the value they reported for $Ni(OH)_2$ on Monel. A strong satellite peak (arrow 4) at 5.2 eV above the principal peak also corresponds to one of their satellites (5.1 eV above their own principal peak). Absent or not clearly distinguishable (because of high level of noise) in the spectrum shown in Fig. 25 is a second satellite structure (arrow 3) which they observed 6.8 eV above their principal line. The appearance of these satellite structures in the spectrum obtained in this study is also indicative of the presence of $Ni(OH)_2$ on the corroded sample.

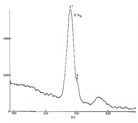

Figure 27. O (1S) x-ray photoelectron spectrum for Monel-400 alloy surface exposed to deaerated 0.5M Na_2SO_4, pH 8.2, at 298K (25°C)

A strong peak at lower binding energy (higher kinetic energy) in the spectrum (Fig. 25) is due to metallic nickel. The presence of this peak gives the appearance that the film on the alloy is very thin; less than 0.9 nm (9A$^{\circ}$) since the mean free path for 2P photoelectrons is approximately 0.7 to 0.9 nm.[176] This being the case, the x-ray was sampling the alloy substrate. A similar peak for Ni was observed by McIntyre et al.[176] during analysis of the film on Inconel-600 alloy. They attributed the presence of the peak to uneven coverage of the surface with precipitated film and the consequent exposure of metallic phase at higher rates in some areas than in others. This premise disregarded the absence of corresponding peaks for metallic chromium and iron in their respective spectra. These elements were also present in the alloy. Barr[171] also saw metallic nickel peak in the Ni (2P) spectrum he obtained. He attributed it to entrapped Ni^{0} in the oxide matrix. He, however, offered no speculation as to the mechanism by which Ni^{0} was trapped in the oxide. Either the thin film premise or the uneven coverage of surface explanation by McIntyre et al.[176] may interpret the data reported here. In either case, the presence of metallic copper recorded in this study could be accounted for.

The absence of a copper oxidation product on the surface of Monel-400 alloy polarized in the passive region does not appear to be consistent with thermodynamic consideration (Potential pH diagram, Fig. 28). McIntyre et al.[46] found no significant oxidation products in their high pH, high temperature experiments carried out under reducing conditions (0.1 MPa H_2 overpressure). Nulett and coworkers[179]

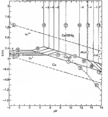

Figure 28 Potential pH equilibrium diagram for the system copper-water at 25°C [Considering the solid substances Cu, Cu_2O and $Cu(OH)_2$] [73]

observed that the XPS spectra of the passive film on 70 Ni - 30 Cu alloy in a NaCl solution at 373 K (100°C) contained primarily nickel oxide similar to the spectrum for pure nickel obtained in the same environment. This observation and the data reported in this study are in agreement with the observation of Uhlig and Osterwald[30] that the passive film of Cu - Ni alloys containing more 30% Ni obtained in 0.5 M K_2SO_4 at 298 K (25°C) was identical to that on pure nickel. However, Takasu et al.[180] analyzed the surface composition of passive film on Cu - Ni alloys using AES and XPS and revealed that the passive film contained copper and nickel in the same ratio as the alloy. Okuyama[181] also found Cu_2O in the passive film of Cu - Ni alloy containing over 50% Ni.

The XPS technique has also failed to pick up iron and manganese. This technique and those reported earlier are probably not sensitive enough to pick up these elements in the concentrations present in the alloy. All the same, the XPS results on nickel are consistent with the theoretical prediction of products of the proposed dissolution-precipitation model.

Atomic ratio of Cu to Ni on the surface was calculated from the XPS data. The ratio was determined to be 0.49 as against 0.44 in the bulk alloy. Although the difference is small and appears to be within experimental error, Castle[182] found the surface film on 50 Cu - 50 Ni alloy slightly enriched with copper during high temperature (773 K) oxidation of the alloy in 13 KPa of oxygen.

Sputtering was not employed in conjunction with E.S.C.A. experiment because the E.S.C.A. equipment was not equipped with ion gun at the time the experiment was conducted. There might well be an underlying oxide layer below the depth sampled by the x-rays. As XPS studies of Ni surfaces in 0.5 M H_2SO_4 by Dickinson et al.[183] revealed the film in the passive region was composed of NiO and $Ni(OH)_2$, with the former acting as passivating species.

4.1.5 Auger Electron Spectroscopic Analysis of Passive Films on Monel-400 Alloy

Auger electron spectroscopic analysis was used in this study to obtain composition profiles of the anodic film on the corroded Monel-400 alloy surface. The use of this technique in addition to the XPS technique appears to be a duplication of techniques. Although each technique has certain features that are superior to the other's, the decision to use both techniques was not made to take advantage of the characteristic features. The need to obtain depth profile information prompted the use of AES which, until recently, was the only available technique which had this capability.

A typical surface scan (before sputtering) Auger spectrum is shown in Fig. 29. The spectrum indicates high concentration of oxygen and carbon as depicted by their peak heights. The surface carbon could have come from the acetone used to dry the sample. It could also have come from exposure to laboratory atmosphere. Another spectrum obtained after sputtering is shown in Fig. 30. Sputtering was terminated for each sample analyzed after the oxygen peak was essentially gone (see Fig. 30). The carbon peak decreased to a constant level after a few minutes sputtering. The final peak level shown in Fig. 30 may be due to elemental carbon contained in the alloy (0.7 w/o).

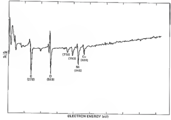

Figure 29 Typical surface scan Auger spectrum from the surface of Monel-400 alloy exposed to deaerated 0.5M Na_2SO_4 solution, pH 8.2 at 298K (25°C).

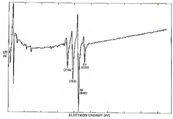

Figure 30. Typical Auger spectrum from sputtered Monel-400 alloy surface exposed to deaerated 0.5M Na_2SO_4 solution, pH 8.2 at 298K (25°C)

In determining concentration profile, peak-to-peak height of the derivative Auger spectrum has been assumed to be proportional to the concentration. Nakayama et al.[184] have determined in their Auger spectroscopic study of Cu - Ni alloys that this is, indeed, so. Since no standard was available for calibration at the time of this experiment, no attempt has been made to determine the sputter rate in terms of layers removed per unit time.

Shown in Fig. 31 are the composition profiles for copper, nickel and oxygen. There appears to be slight depletion of copper and nickel at the surface.

The calculated oxygen profile does not appear to be consistent with one of the explanations given (section 4.1.4) for the presence of observed Ni^0 peak in the XPS spectrum shown in Fig. 25. That is, that the x-ray was sampling the underlying alloy substrate because the film was very thin. If one went by the time it took the oxygen profile to level off, it would appear that the film on the surface of the alloy was between about 1×10^{-6} and 2×10^{-6} cm. It turned out that the film on the alloy was not uniform and, as will be shown later in section 4.2.8, some parts of the sample surface were covered with dendrite-like structure that was highly porous. This uneven coverage could, as explained by McIntyre et al.,[176] lead to exposure of bare alloy surface at higher rates in some areas than in others. The average thickness of the film should be much less than portrayed by the oxygen profile. Sampling of the substrate surface where the film is thin could give rise to the metallic nickel peak seen in the spectrum of Fig. 25.

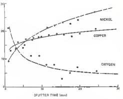

Figure 31 Auger composition profile obtained from Monel-400 alloy exposed to deaerated 0.5M Na_2SO_4, pH 8.2, at 298K (25°C).

Composition profile is also presented in terms of ratio of copper peak-to-peak height to that of nickel (Fig. 32). The figure compares the composition of a sample anodized in the passive region (open squares) to that of an unpolarized sample (solid squares). Also shown in the figure (dashed line) is the Cu/Ni composition ratio calculated from alloy composition. The sets of Auger data (for the bulk alloy and the surface) contain considerably lower concentration of copper than calculated from chemical composition of the alloy. This implies copper depletion or nickel enrichment or both. Whether electron beam effects play a role in this phenomenon is not known. Plasma sputtering, however, has been reported to produce the effect observed in this study.[183-185]

Tang and Wehner[185] using Auger electron spectroscopy in combination with argon ion sputtering have studied the composition changes at Constantan (55 Cu - 45 Ni) target surface as a function of bombarding ion energy. They found that at all bombarding energies, Ni becomes enriched at the target surface. They attributed the surface nickel enrichment to preferential sputtering of copper. They reported that copper was sputtering at a rate 1.6 times that of nickel. Shimizu et al.[186] reported copper sputtering yield 1.5 times larger than that of nickel in their AES study of various ratios of Cu/Ni. The data for Monel-400 alloy reported here indicates a copper sputtering yield 1.4 times larger than that of Ni.

The preferential sputtering effect, however, does not, in any way, diminish the significance of the point illustrated in Fig. 32. The data from polarized specimen show somewhat higher concentration of

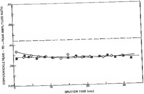

Figure 32. Auger composition profile in terms of Cu/Ni peak-to-peak ratio. Deaerated 0.5M Na_2SO_4, pH 8.2 at 298K (25°C)

of copper at the interface. Copper concentration fell to the level present in the bulk after about 5 minutes of sputtering. The surface enrichment indicated by this technique agrees with the data obtained from the E.S.C.A. technique. The only difference in treatment between the two Auger samples was that one was anodized and the other was not. The difference in surface composition could, therefore, have come only from chemical or electrochemical (anodic) processes. Selective dissolution of nickel (denickelization) or precipitation of a copper compound from solution that was not yet saturated with respect to nickel may account for the observed copper enrichment. The results of E.S.C.A. study on samples treated in the same way as the AES samples indicated that no copper oxidation products were present in the passive film. This casts doubts on the latter hypothesis. Considering that the electron probe was small in comparison with the sample size, the possibility of the observed phenomenon being a local effect was considered. The experiment was repeated two more times to confirm this view. The results were essentially the same, suggesting denickelization probably occurred to some extent.

As with the other techniques described previously, peaks for iron and manganese were prominently absent in the Auger spectra shown.

In summary, the dissolution of copper from Ni - Cu alloys in Na_2SO_4 solution proceeds directly to Cu(II) species without the intermediate formation of cuprous ions. A dissolution-precipitation model has been used to explain the mass transport dependence of Monel-400 alloy dissolution in this environment.

No copper oxidation products were found in the passive film obtained after 10 minutes polarization. It could not be determined from the xps data presented here whether the Cu peak observed came entirely from surface of the alloy (below the film) or partly from redeposited copper in the film. Both the xps and AES results have shown slight enrichment of Cu on the anodized Monel-400 alloy surface.

4.2 Anodic Polarization in Deaerated 0.5 M NaCl Solution

4.2.1 Linear Sweep Voltammetry

A rotating Monel-400 electrode potentiokinetic curve is measured in deaerated 0.5 M NaCl solution (pH 8.2) is presented in Fig. 33. The polarization curve was obtained at a potential scanning rate of 5 mV/sec. Data obtained in chloride environments has been presented on a semi-logarithmic scale in order to accommodate the large variation in the magnitude of the current densities (0.01 $\mu A/cm^2$ to 432 $\mu A/cm^2$). A Tafel (linear) region is observed between the potential of -300 mV and +50 mV vs Ag/AgCl. Unknown cathodic process may have contributed to the non-linear behavior in the low over potential region. Above +50 mV the curve deviates from linearity and tends toward a limiting current behavior.

The slope of the anodic Tafel line is

$$b = \left(\frac{\partial E}{\partial \log i}\right) = 119 \text{ mV/dec.}$$

A Tafel slope of 75 mV/dec. has been reported for Ni in 0.5M NaCl (pH 0),[18] while 60 mV/dec. has generally been reported for Cu in chloride environments.

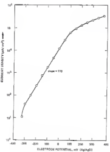

Figure 33. Potentiokinetic polarization curve for Monel-400 alloy in deaerated 0.5M NaCl, pH 8.2, at 298K (25°C) S = 5mV/sec, w = 1600rpm.

In addition to the possible reactions listed in section 4.1.1, the following reactions are considered possible in the anodic region.

$$\mathrm{Cu\ (Monel)} + \mathrm{Cl}^- = \mathrm{CuCl} + e \qquad [23]$$

$$\mathrm{CuCl} + \mathrm{Cl}^- = \mathrm{CuCl}_2^- \qquad [24]$$

$$\mathrm{CuCl}_2^- + \mathrm{Cl}^- = \mathrm{CuCl}_3^{2-} \qquad [25]$$

Braun and Nobe[187] have reported that for $[\mathrm{Cl}^-] < 0.7\mathrm{M}$, CuCl_2^- is the main complex, while at higher concentrations, the complex CuCl_3^{2-} is dominant. Hurlen[188] and others,[189-193] have observed that the anodic copper dissolution shows a reaction order of 2 with respect to chloride ions at concentrations < 1M and a reaction order of 3 at concentrations > 1M, suggesting the formation of CuCl_2^- and CuCl_3^{2-} complex ions, respectively.

4.2.2 Characterization of Soluble Reaction Products

With the electrode rotated at 1600 r.p.m., the central electrode potential was swept at a controlled rate of 5 mV/sec from -500 mV to +400 mV to produce the results shown in Fig. 34 for three ring potentials. The potential scan was stopped at +400 mV because pitting was observed to occur beyond this potential value at the potential sweep rate used.

Operation of the ring at +600 mV where Cu(I) ions or its complexes are oxidized to Cu(II) ions produced curve (a) [Fig. 34a]. This establishes the existence of Cu(I) products in solution. It is well known that Cu(I) ions form complexes with chloride ions. As pointed

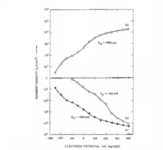

Figure 34. Collector ring current density as a function of applied potential in deaerated 0.5M NaCl solution, pH 8.2 at 298K (25°C). S = 5mV/sec , w = 1600rpm.

out above, and considering the concentration of chloride ions used (0.5M) in this study, the more probable complex ion is $CuCl_2^-$. This complex has been identified in chloride solutions by many other investigators [188-193]. It has been determined that transport of complex ions towards the bulk solution control copper anodic dissolution.[187,191,195-197]

Operation of the ring at -150 mV produced curve (b) which is due to the reduction of Cu(II) ions to Cu(I) ions. This indicates strongly that Cu(II) ions are present in solution and could have been generated from any of these reactions,

$$Cu\ (Monel) \rightarrow Cu^{2+}aq + 2\ e \qquad [11]$$

$$2\ Cu^{+}aq \rightarrow Cu + Cu^{2+}aq \qquad [26]$$

$$CuCl \rightarrow Cu^{2+}aq + Cl^{-} + e \qquad [27]$$

$$4\ Cu^{+}aq + O_2 + 2H_2O = 4\ Cu^{2+}aq + 4\ OH \qquad [28]$$

$$Cu^{+}aq \rightarrow Cu^{2+}aq + e \qquad [29]$$

Reaction [26] can only occur if the concentration of free Cu^{+} ions in solution exceed 10^{-7}M. The stability constant for this reaction is given[100] to be 10^{-7}. From the reaction

$$CuCl_2^{-} = Cu^{+}aq + 2Cl^{-} \qquad [30]$$

the stability constant, K, the value of which is given by

$$K = \frac{[Cu^+_{aq}] [Cl^-]^2}{[CuCl_2^-]} = 1.58 \times 10^{-6} \qquad [31]$$

(value taken from reference No. 158), the concentration of Cu in solution can be determined. Using the value of partial current density for Cu(I) at OV (477.99 μA/cm^2), the concentration of $CuCl_2^-$ was estimated from the plot of [$CuCl_2^-$] vs. current density for pure copper electrode (Fig. 27 of reference 195) to be 8.00 x 10^{-4} mol /l. This curve was determined, however, on the assumption that copper dissolves solely via Cu(I) ions. Substituting the values of K and [$CuCl_2^-$] into [31], one has

$$1.58 \times 10^{-6} = \frac{[Cu^+_{aq}] [Cl^-]^2}{[8 \times 10^{-4}]}$$

The estimated value of the concentration of free Cu(I) ions in solution from this relation is 5.00 x 10^{-9} mol /l. This is about two orders of magnitude less than the stability constant for reaction [26]. This reaction, therefore, cannot occur under these conditions. Moreover, reaction [26] does not depend on the applied potential but curve (b) (Fig. 33) shows dependence on applied potential.

The standard potential for reaction [27] has been reported to be +250 mV (+536 SHE) [100]. This reaction is unlikely to account for Cu(II) current sensed at -100mV. It takes Cu(II) ion concentration as low as 1.60 x 10^{-10}M to sense its current at -100mV. The collector electrode is not sensitive enough to sense currents for concentrations as low as 10^{-10} M. The concentration of Cu(II) ions in solution must have been much higher than 10^{-10}M, implying that the over-potential for reaction (27) was at a much higher anodic value. Reaction (27) could not have accounted for the Cu(II) current in the potential region around -100 mV.

Another possible reaction considered is the oxidation of Cu^+aq. by any oxygen in solution to Cu(II) ions. This reaction is doubtful in that, as argued earlier, this reaction also is homogeneous and should not show any dependence on potential. More importantly, data in Fig. 34 were obtained in deaerated solution. An estimation of the charge from the area under the curve in Fig. 35 (plotted on linear scale) gives a charge of 107.50 Coul. This translates to 1.11 x 10^{-3} moles Cu(I) oxidized to Cu(II). Based upon the volume of solution used (150 ml) it would have required 59 ppm of oxygen to account for the current shown in Fig. 35. Assuming even the worst case, that is, that the solution was saturated with air (8 ppm max),[201] reaction (26) still cannot account for all the Cu(II) current below about +350 mV.

Based on the foregoing analysis, only reaction (II) has the greatest probability of giving rise to the Cu(II) current in the low over-potential region. The implication of this observation is enormous if one considers the fact that many data interpretations and conclusions thereof have been made based on the assumption that copper dissolves in chloride ions and in the potential region considered (-100 to +100 mV) via cuprous ion complexes. Although the applied potential dependence of the distribution of Cu(I) and Cu(II) species is such that Cu(I) species predominate in this region (compare

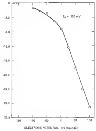

Figure 35. Cu II current density as a function of applied Monel-400 electrode potential. Deaerated in 0.5M NaCl solution, pH 8.2 at 298K (25°C) S = 5mV/sec., w = 1600rpm.

Figs. 36-38), the amount of Cu(II) ions generated may be of sufficient quantity to render suspect any conclusions which are based on the assumption that they are not generated.

As illustrated in Fig. 37, and more vividly in Fig. 38, there is a sudden increase in Cu(II) current above about +100 mV. It has been reported that CuCl film starts growing at the instant the anodic current is turned on.[192] Many other investigators have reported observing a CuCl film on dissolving copper electrodes.[190,195,198,200] Above +100 mV, the dissolution of the CuCl according to reaction (27) becomes possible, and occurs in parallel with reaction (11).

Curve (c) (Fig. 34) was obtained with the collector electrode potential maintained at -600 mV to reduce all soluble species, including nickel species. The figure is almost a mirror reflection of curve (e) and about equal in magnitude. This shows that nickel's contribution is very small, if any, to this curve. This supports the observation reported in section 4.2.2. The presence of nickel in the solution has, however, been established by solution analysis using AAS technique (Table 6). Iron and manganese could also not be picked up here.

The ratios of ring currents to the total anodic current are plotted as a function of applied potentials as shown in Figs. 36 and 37 for two reasons. The first is that, since one experiment is repeated two or three times, one for each soluble species in solution, normalizing ring current with respect to the total anodic current ensures that no "artificial" fluctuation in the central electrode current and, hence, in the collector ring current, leads to misinterpretation of data when two or more sets of data are compared. This is especially critical when the effects of certain

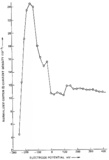

Figure 36 Normalized Cu(II) current density as a function of applied Monel-400 electrode potential in deaerated 0.5M NaCl solution, pH 8.2 at 298K (25°C)
S = 5mV/sec , w = 1600rpm

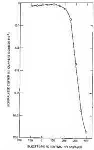

Figure 37. Normalized Cu(II) current density as a function of applied Monel-400 electrode potential. Deaerated 0.5M NaCl solution, pH 8.2 at 298K (25°C). S = 5mV/sec, w = 1600rpm.

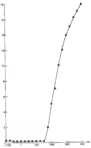

Figure 38. Ratio of Cu(II) current density to Cu(I) current density as a function of applied Monel-400 electrode potential 0.5M (deaerated) solution, pH 8.2 at 298K (25°C) S = 5mV/sec., w = 1600rpm.

Table 6 Atomic Absorption Data From Potentiostatic Tests in 0.5M NaCl Solution at 298 K (25°)

Potential of Polarization (Ag/AgCl)	Amount in Solution (PPM)			
	Ni	Cu	Fe	Mn
− 50 mV	1.00	0.40	0.20	nil
0 mV	3.80	1.40	0.20	nil
+ 50 mV	4.80	2.40	0.10	nil
+ 100 mV	5.80	2.80	0.10	0.10

parameters or soluble dissolution products are investigated. Secondly, the changes in the collector ring current with respect to the total anodic current can be used to indicate where the effects of other competing anodic processes such as film forming reactions are predominant as can be seen from Fig. 39 which is the curve for normalized total copper current.

As Fig. 39 shows, the proportion of soluble copper dissolution product rises with increasing total anodic current after which it falls to a constant level between -50 mV and about +100 mV. Beyond this point the proportion of copper current rises again with increasing total anodic current. Either the copper currents decrease or the total anodic current increases much faster than the current due to copper dissolution in the region of minimum normalized current. As Fig. 40 shows, the total copper current within the potential region where current minimum is observed rises steadily with increasing over-potential. The minimum is, therefore, due to a faster increase in the total anodic current in that potential region. The possibility of increased nickel dissolution current was considered. As Table 6 shows, the amount of nickel and copper in solution from an experiment done within the potential range being considered are close to their respective stoichiometries in the alloy. Nickel, therefore, could not account for the behavior in this region. It is most probable that increased total anodic current largely due to formation of insoluble reaction products accounts for the behavior in this region.

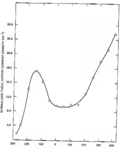

Figure 39. Normalized total copper current density as a function of Monel-400 applied potential Deaerated 0.5M NaCl, pH 8.2, at 298K (25°C) S = 5mV/sec., w = 1600rpm

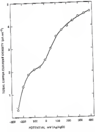

Figure 40 Total copper current density as a function of applied Monel-400 electrode potential. Deaerated NaCl, pH 8.2 at 298K (25°C). S = 5mV/sec., w = 1600rpm

On the basis of the data presented here and their analysis, the following reaction scheme is proposed for Monel dissolution in this environment:

a] for Cu

up to about -100 mV the following reactions occur:

$$\mathrm{Cu\ (Monel)} \rightarrow \mathrm{Cu^{+}\,aq.} + e; \qquad [10]$$

$$\mathrm{Cu^{+}aq.} + 2\mathrm{Cl^{-}} \rightarrow \mathrm{CuCl_2^{-}} \qquad [30]$$

Occurring in parallel with reactions [10] and [30] is the reaction of surface copper with chloride ions as follows

$$\mathrm{Cu\ (Monel)} + \mathrm{Cl^{-}} \rightarrow \mathrm{CuCl} + e; \qquad [23]$$

The following reaction occurs in parallel with reactions [10] and [30] in the potential region between -100 and +150 mV:

$$\mathrm{Cu\ (Monel)} \rightarrow \mathrm{Cu^{2+}aq.} + 2\,e \qquad [11]$$

Above about +100 mV, the following reactions are possible:

$$\mathrm{Cu\ (Monel)} \rightarrow \mathrm{Cu^{+}aq} + e \qquad [10]$$

$$\mathrm{Cu^{+}aq} + 2\mathrm{Cl^{-}} \rightarrow \mathrm{CuCl_2^{-}} \qquad [30]$$

$$\mathrm{CuCl} \rightarrow \mathrm{Cu^{2+}aq.} + \mathrm{Cl^{-}} + e \qquad [27]$$

$$\text{Cu (Monel)} \rightarrow \text{Cu}^{2+}_{\text{aq.}} + 2\,e \qquad [11]$$

b) for nickel, the dissolution reactions is as proposed in the sulfate solution, i.e.:

$$\text{Ni (Monel)} + \text{OH}^- = \text{NiOH}_{\text{ads.}} + e^- \qquad [1a]$$

$$\text{NiOH}_{\text{ads.}} \rightarrow \text{NiOH}^+ + e^- \qquad [1b]$$

$$\text{NiOH}^+ + \text{NiOH}^+ \rightarrow \text{Ni}^{2+} + 2\,\text{OH}^- \qquad [32]$$

Formation of $NiCl_2$ either by dissolution-precipitation mechanism according to equation [33] or

$$\text{Ni}^{2+}_{\text{aq.}} + 2\text{Cl}^- \rightarrow \text{NiCl}_2 \qquad [33]$$

$$\text{Ni (Monel)} + 2\text{Cl}^- \rightarrow \text{NiCl}_2 + 2\,e \qquad [34]$$

or by solid state mechanism according to equation [34] may also take place

4.2.3 Effect of Electrode Rotation Speed

The influence of solution flow rate on the anodic polarization in NaCl solution is very different from its effect in Na_2SO_4 solution. Polarization curves measured at different angular velocities are shown in Fig. 41. There is little dependence on rotation speeds. The slopes (Tafel) obtained in the linear region vary from 117 mV/dec. to

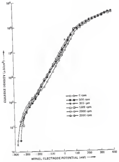

Figure 41. Anodic potentiokinetic polarization curves for Monel-400 alloy in deaerated 0.5M NaCl, pH 8.2, at various rotation speeds; 298K (25°C) S = 5mV/sec

122 mV/dec. in no particular order, indicating the slopes are rotation speed independent. What appears to be diffusion limited current density region in the high overpotential region is, as evident from the figure, not a diffusion limited current region since it does not show any dependence on electrode rotation velocity. The levelling off of current density in this region may be due to an anodic process such as film formation controlling the reaction in the region or change in reaction mechanism. IR drop as result of the presence of film and/or high current density may also have a similar effect.

The effect of solution flow rate on the soluble dissolution products of copper was investigated with a view to determining its effect on the distribution of reaction products with respect to applied potential as well as the magnitudes of their respective currents. The curves for Cu(I) and Cu(II) are shown in Figs. 42 and 43, respectively. There is no trend in the curves for Cu(I) (Fig. 42) except at the peak current densities where the behavior resembles what was observed in the Na_2SO_4 (see Fig. 21). That is, the normalized peak current decreases with increasing electrode rotation speed up to 1600 r.p.m. above which it rises with rotation velocities. However, unlike in the Na_2SO_4 environment, a plot of normalized peak current density as function of the square root of angular velocity (not shown) does not show linear dependence. This suggests that diffusion of soluble reaction products does not control the behavior in NaCl solution, as is the case with a pure copper electrode.

The normalized peak current plotted for Cu(II) (Fig. 43) reveal the same trend at the high overpotential region except for the curve

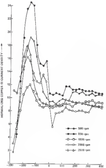

Figure 42. Normalized copper(I) current density as a function of applied Monel-400 electrode potential at various electrode rotation speeds. Deaerated 0.5M NaCl, pH ≈ 2 at 298K (25°C) S = 5mV/sec.

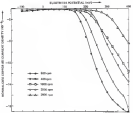

Figure 43. Normalized copper(I) current density as a function of applied Monel-400 electrode potential at various electrode rotation speeds. Deaerated 0.5M NaCl, pH 8.2 at 298K (25°C). S = 5mV/sec.

at 2500 r.p.m. The distribution of the copper dissolution products is shown in Fig. 44. The curves exhibit exactly the same behavior as that described for Cu(II) in the high overpotential region confirming the dominance of this species in this region.

Figure 45 is the algebraic sum of Figs. 42 and 43. The conclusion from the set of data on the effect of solution velocity is that, within the potential range and angular velocities studied, there is little effect of solution transport on both the magnitude of the currents and the distribution of soluble copper dissolution products.

4.2.4 Effect of Chloride Ion Concentration

The effect of chloride ion concentration was investigated from 10^{-5}M to 6M. The polarization curves exhibit active/passive/transpassive transitions similar to what was observed in Na_2SO_4 solution (Fig. 15) for concentrations up to 1.0×10^{-2}M. Also, as in sulfate solution, the only copper ionic species detected in chloride concentrations up to 10^{-2}M were Cu(II) ions in agreement with the observation of Braun and Nobe.[187] Similar behavior was observed for pure copper electrode in sodium bicarbonate solution containing chloride ion concentration up to 10^{-2}M.[204] Not only does the alloy lose its ability to passivate in chloride concentrations above 5×10^{-2}M, but also one begins to sense Cu(I) species on the collector electrode in addition to Cu(II) ions (Figs. 46 and 47). The proportions of Cu(I) products detected increase therefrom with increasing chloride ion concentration (Fig. 46). Whether there is any correlation between inability of the alloy to sustain passivity and the presence of Cu(I) species in solution

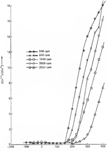

Figure 44. Ratio of Cu(II)/Cu(I) current densities as a function of electrode potential at various rotation speeds. Deaerated 0.5M NaCl, pH 8.2 at 298K (25°C) S = 5mV/sec.

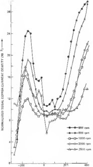

Figure 45 Normalized total copper current density as a function of Monel 400 electrode potential, at various electrode rotation speeds. Deaerated 0.5M NaCl, pH 8.2 at 298K (25°C). S = 5mV/sec

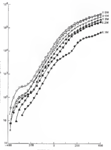

Figure 46 Anodic potentiokinetic polarization curves for Monel-400 alloy at various chloride ion concentrations, pH 8.2, 298K (25°C); S = 5mV/sec; w = 1600rpm

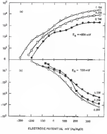

Figure 47 Collector ring current density as a function of Monel-400 electrode potential at various chloride ion concentrations pH 8.2 at 298K (25°C). S = 5mV/sec , w = 1600rpm

is not yet known. It is possible that the observation of the two phenomena at the same chloride ion concentration is purely coincidental.

The ratio of cupric ion concentration to cuprous ion concentration is plotted in Fig. 48 to show the effect of chloride ion concentration on the distribution of these species. The only concentration that shows a distinct effect is 0.1M which shows considerable amount of Cu(II) ions in the low over-potential region. The logarithmic plot of current density (obtained potentiostatically at a constant over-potential) is shown in Fig. 49. The curve has a sigmoid shape with a linear portion in the middle. The slope of the linear portion is

$$\left(\frac{\partial \log i}{\partial \log[\mathrm{Cl}^-]}\right)_{\phi = 0} = -2.49$$

suggesting a reaction order with respect to chloride ion concentration of 2.49.

Copper dissolution in chloride solutions has a reaction order of 2 with respect to chloride ion concentration, signifying dissolution via $CuCl_2^-$. Nickel has been reported to show a reaction order of 0.5 in acidic chloride concentrations < 1M and a reaction order of 1.1 in chloride concentrations > 1M.[19] The fact that the reaction order determined in this study is much closer to that of pure copper is another support for the observation that copper dissolution kinetics control the corrosion behavior of Monel-400 alloy.

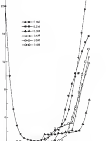

Figure 48 Ratio of Cu(II)/Cu(I) current densities as a function of chloride ion concentration. pH = 2 at 298K (25°C). S = 5mV/sec , w = 1600rpm

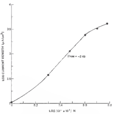

Figure 49 Logarithmic plot of Monel-400 dissolution current as a function of chloride ion concentration pH = 2 at 298K (25°C). S = 5mV/sec., w = 1600rpm.

4.2.5 Effect of Temperature

Anodic polarisation curves were obtained at different temperatures (Fig. 50). A general increase in the current density with increasing temperature is observed. Many chemical and electrochemical reactions can be predicted by Arrhenius relation given by the following equation

$$K = K_o \exp\ (-Q/RT) \qquad [35]$$

where K is the rate of chemical or electrochemical reaction. K_o is a constant that does not depend on temperature, Q is activation energy in calories per mole, R is the gas constant and T is absolute temperature (K). Shown in Fig. 51 is the log i versus the reciprocal of temperature. The slope of the curve is

$$\left(\frac{\partial \log i}{\partial T^{-1}}\right) = -1.86$$

at $E_{appl} = 0$ V

If metal dissolution kinetics can be represented by equation [35], then the activation energy for dissolution of Monel-400 can be determined from the slope of log i vs. $\frac{1}{T}$. Thus using the slope of Fig. 51, the activation energy for Monel-400 is found to be 8.5 KCal/mole. This is about one-half as much as was reported by Krohenberg et al.[18] for

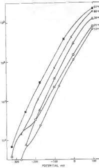

Figure 50 Anodic polarization curves for Monel-400 alloy in deaerated 0.5M NaCl, pH 8.2, at various temperatures. S = 5mV/sec ; w = 1600rpm.

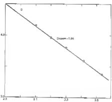

Figure 51 Arrhenius plot of Monel-400 alloy current in deaerated 0.5M NaCl, pH 8.2 S = 0mV/sec., w = 1600rpm

nickel in chloride solution (15 Kcal). The activation energies for copper ranging from 5.1 - 7.0 Kcal/mole depending on flow conditions has been determined in chloride solution[136]. Again, that of Monel-400 alloy determined here is close to the values obtained for copper.

Figure 52 shows a corresponding Arrhenius plot for a ring current obtained at +600 mV. The slope of the curve is -2.24. The value of activation energy calculated from this slope is 10.2 Kcal/mole of cuprous ions. This is a little higher than obtained for total anodic current but close enough to indicate the influence of copper on the anodic behavior of Monel-400 alloy.

4.2.6 Behavior in the Presence of Oxygen

The anodic polarization for Monel-400 alloy was measured in air-saturated 0.5M NaCl solution. Figure 53 compares the curves obtained in deaerated and air-saturated solutions. A striking difference is the shift of the curve for air-saturated solution to more noble potentials. The two curves converge at a potential about +200 mV above which, it appears, the processes occurring are no longer influenced by the presence of oxygen. Pitting processes are more likely to occur at the high over-potential region where oxygen appears to have no influence. This casts doubts on the role of oxygen in the pitting reactions (initiation and/or propagation).

The lower current density obtained in the presence of oxygen in the potential region below +200 mV points to the presence of

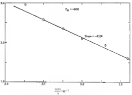

Figure 52 Arrhenius plot of collector ring current in deaerated 0.5M NaCl pH 8.2 S = 0mV/sec , w = 1600rpm

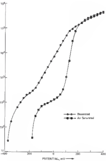

Figure 53 Comparison of anodic polarization curves for Monel-400 alloy in deaerated and air-saturated NaCl, pH 8.2, at 298K (25^{o}C), S = 5mV/sec w = 1600rpm

possibly a more resistant film on the electrode surface in the air-saturated solution. The Tafel slope obtained in the presence of oxygen varies from 32 mV/dec. to 39 mV/dec. As in the deaerated solution, the electrode remains active throughout the potential range investigated.

Comparison of the normalized ring current densities for the two solutions show that the behavior of Cu(I) currents resembles that of the total anodic current. There is little difference between behavior for Cu(II) currents in both environments (Fig. 54). In contrast to behavior in deaerated solution (Fig. 34), evidence is presented here (Fig. 55) to show that both cupric and cuprous species are simultaneously generated at all potentials investigated. More importantly, the distribution of both species with respect to applied potential are reversed (Fig. 56). Cupric ions are predominant in the low over-potential region while cuprous species are slightly dominant in the middle to high over-potential region. There is no doubt that the distribution of soluble copper dissolution products are affected by the presence of oxygen. Oxygen definitely affects the concentration of cuprous ions, and hence, that of cupric ions in the solution. But as the analysis in section 4.2.2 has shown, the amount of oxygen this solution can dissolve is not more than 8 ppm at 298 K (25°C). Oxygen, therefore, accounts but for a small portion of the cupric ions detected.

The effect of angular velocity was determined in the presence of oxygen (Fig. 57). As in the deaerated solution, there is little dependence on solution flow rate. This is surprising in that the

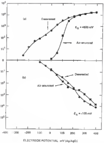

Figure 54 Comparison normalized collector ring current densities obtained in deaerated and air-saturated 0.5M NaCl pH 8.2, at 298K (25°C) S = 5mV/sec , w = 1600rpm.

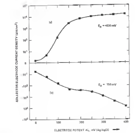

Figure 55 Collector electrode current density as a function Monel-400 electrode potential in air-saturated 0.5M NaCl, pH 8, at 298K (25°C). S = 5mV/sec., w = 1600rpm.

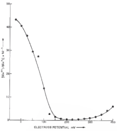

Figure 56. Ratio of Cu(II) - Cu(I) current densities as a function of Monel-400 electrode potential in air-saturated 0.5M NaCl, pH 8.2, at 298K (25°C). S = 5mV/sec., w = 1600rpm

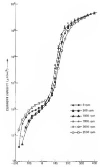

Figure 57 Anodic polarization for Monel-400 alloy in air-saturated 0.5M NaCl, pH 8.2, at various rotation speeds. S = 5mV/sec

corrosion of Monel-400 alloy in natural seawater is strongly dependent upon solution flow rate; the alloy becoming susceptible to pitting attack under stagnant or low velocity conditions. One possible explanation is that all the electrode rotation speeds used correspond to linear velocities in the low velocity flow regime. This being the case, it would require much higher range of flow velocities than is possible with the speed generator used in this study to observe any dependence.

As the curve for air-saturated solution shows (Fig. 53), the Tafel line falls in the potential region where cupric ion is dominant. If Tafel slope is any use on its own (without knowledge of transfer coefficient and electrochemical order) in determining dissolution mechanisms, as often practiced by many investigators, the slope of 34 mV/dec obtained for Monel-400 in air-saturated solution seems to agree with the proportion of cupric ions (much larger) in this region. The reservation expressed earlier in connection with assumptions that copper dissolves solely via cuprous ion species in chloride solution appears to have found stronger support in the data shown in Figs. 55 and 56. That is, that a much larger amount of these Cu(II) ions is generated in potential region than had been thought. Figure 58 shows the influence of flow rate on collector ring currents. The current behavior in the low over-potential region shows some dependence on fluid flow rate, the behavior resembling that observed in Na_2SO_4

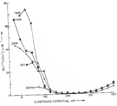

Figure 58 Ratio of Cu(II) to Cu(I) current densities as a function of Monel-400 electrode potential in air-saturated 0.5M NaCl, pH 8.2, at various electrode rotation speeds S = 5mV/sec.

Table 7 Binding Energy Data for Ni (2p) Obtained in 0.5 M NaCl pH 8.2, 298 K (25°)

Sample Treatment		Binding Energy, eV				
		Ni	NiO	Ni_3O_4	NiO_2	$Ni(OH)_2$
Deaerated Solution	Surface	-	-	-	-	856.60
	Sputtered	-	-	853.10	-	-
Air-saturated Solution	Surface	-	-	-	-	855.60
	Sputtered	852.70	-	-	-	-

Table 8. Binding Energy Data for Cu (2p) Obtained in 0.5 M NaCl, pH 8.4, [illegible]

Sample Treatment		Binding Energy, eV					
		Cu	Cu_2O	CuO	$Cu\ (OH)_2$	CuCl	$Cu(L_3M_{4,5}M_{4,5})$
Deaerated Solution	Surface	–	–	933.30	–	–	337.20
	Sputtered	–	933.0	–	–	–	337.30
Air-saturated Solution	Surface	–	–	932.80	–	–	336.30
	Sputtered	–	932.60	–	–	–	336.30

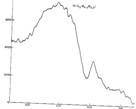

Figure 59 Ni ($L_3M_{4,5}M_{4,5}$) Auger spectrum for Monel-400 alloy surface exposed to deaerated 0.5M NaCl, pH 8.2, at 298K (25°C).

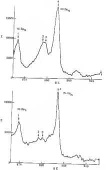

Figure 60 Ni (2p) X-ray photoelectron spectrum for Monel 400 alloy surface exposed to deaerated 0.5M NaCl, pH 8.2, at 298K (25°C), $E_{appl.}$ = 0V.

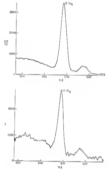

Figure 61 O (1s) x-ray photoelectron spectrum obtained from the surface of Monel-400 alloy exposed to deaerated 0.5M NaCl, pH 8.2, at 298K (25°C) E_{appl} = 0V

4.2.7 E.S.C.A. Analysis of Insoluble Dissolution Products

The insoluble dissolution products formed on samples polarized in NaCl solution were analyzed using an E.S.C.A. technique. Two samples were used in this experiment. One was polarized in deaerated solution at the potential of 0 V for 2 hours while the other was polarized in air-saturated solution for 24 hours at the same potential. The binding energy data from these analyses are reported in Tables 7 and 8 for Ni ($2p_{3/2}$) and Cu ($2p_{3/2}$), respectively. X-ray-induced Auger spectra for Ni and Cu were obtained. Data for Cu are included in Table 8. Nickel Auger spectra were too broad to provide accurate shifts in line energy (Fig. 59). They are, therefore, not used in the assignment of spectra to nickel compounds.

Figure 60 show Ni (2p) spectra. The top spectrum was recorded before sputtering while the bottom spectrum was measured after sputtering. The top spectrum has been assigned to Ni $(OH)_2$ on the basis of binding energy and satellite structures discussed in section 4.1.4. Identification of the bottom spectrum is not as straightforward. The binding energy of the main peak falls between those of elemental Ni and NiO (Table 5). Because of the presence of oxygen spectrum after sputtering (bottom of Fig. 61), this spectrum cannot be assigned to NiO. However, the satellites are much weaker than has been reported for NiO.[46, 170] Besides, the principal line is much narrower than have been recorded for NiO. The energy difference between the satellite peaks (arrows 2 and 3, bottom figure) is 1.70 eV as against 0.70 eV measured by McIntyre and et al.[170] On the basis of this analysis, NiO is ruled out. The compound underlying the $Ni(OH)_2$ is probably Ni_3O_4 or NiO_2. This cannot be confirmed because no xps data could be found in the available literature on Ni_3O_4 and NiO_2.

Shown in Fig. 62 are the Cu ($2p_{3/2}$) spectra obtained from the same sample. The top spectrum is assigned to a cupric compound on the basis of the strong satellite band and peak energy. Comparison with data in Table 4 suggests CuO. This was corroborated by the Auger data (Fig. 63) both by the spectral features and the principal line energy as recorded by Schon.[167] The bottom spectrum obtained from sputtered surface does not have satellite structures. Cupric compounds are, therefore eliminated. The principal peak energy of 933.0 eV is a little too high for elemental copper but within the range for a cuprous compound (Table 4). Assignment cannot be made on the basis of oxygen or chloride peaks because of unknown contribution by nickel to these spectra. Comparison of Auger parameter calculated from the data obtained in this study and those reported in an XPS handbook[163] strongly favore Cu_2O.

Figure 64 presents Ni (2p) spectra obtained from the sample polarized in air-saturated solution. The topmost film (top spectrum) has features similar to those of the spectrum assigned to $Ni(OH)_2$. The shifts in binding energy and the structural features of the satellite band favor $Ni(OH)_2$. Examination of the spectrum sputtered from sample (bottom figure) strongly suggests the presence of Ni^0. This is surprising since the presence of both oxygen and chlorine are indicated by their strong peaks as depicted obtained after sputtering.

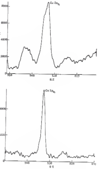

Figure 62- Cu (2p) x-ray photoelectron spectrum for Monel-400 alloy exposed to deaerated 0.5M NaCl, pH 8.2, at 298K (25°C); E_{appl} = 0V

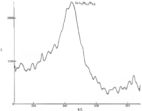

Figure 63 Cu ($L_3M_{4,5}M_{4,5}$) Auger spectrum for Monel-400 alloy surface exposed to deaerated 0.5M NaCl, pH ≅ 2, at 298K (25°C); $E_{appl.}$ = 0V.

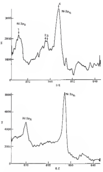

Figure 64 Ni (2p) x-ray photoelectron spectrum for Monel-400 alloy surface exposed to air-saturate 0.5M NaCl pH 8.2, at 298K (25°C) E_{appl} CV-

Shown in Fig. 65 are Cu ($2p_{3/2}$) spectra. The analysis of the top figure has indicated the presence of both Cu^0 peak (arrow 5) and a peak for a Cu(II) compound (arrow 4). The specific cupric compound cannot be identified. But $Cu_2(OH)_3Cl$ has been identified on Cu-Ni alloy polarized in air-saturated solutions by a conventional x-ray diffraction technique. There is a strong possibility that this compound gave rise to the top spectrum of Fig. 65 since oxygen and chlorine spectra have also been recorded from the same sample surface (see Fig. 66 for chlorine spectrum). The bottom spectrum has been assigned to Cu_2O on the basis of the analysis of the spectral data.

Chlorine spectra have been obtained from sputtered and unsputtered sample surfaces. Although no specific chloride compound has been positively identified, the presence of chlorine peaks on all sample surfaces treated in chloride solutions suggests that in addition to the hydroxides and oxides, chlorides ($NiCl_2$, $CuCl_2$, CuCl or basic copper chloride) might also be present.

4.2.8 SEM/EDX Analysis of the Corroded Monel-400 Alloy Surface

Figure 67 displays the photomicrographs obtained at the surface of a Monel-400 alloy sample polarized at 0 V for 24 hours in air-saturated 0.5M NaCl solution. Figure 67a was obtained before the sample was washed. Shown in fig. 67b is the micrograph obtained after the sample was washed. The white debris seen in Fig. 67a disappeared after washing. This suggests that the white material was a salt precipitate. White dendrite-like structures which did not dissolve on washing can be seen at the top of Fig. 67b. Numerous pits formed on the sample surface (Fig. 67a & b). The pits formed mainly within the grains.

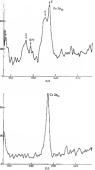

Figure 65. Cu (2p) x-ray photoelectron spectrum for Monel-400 alloy exposed to air-saturated 0.5M NaCl, pH 8.2, at 298K (25°C); $E_{appl.}$ = 0V

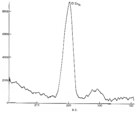

Figure 66. Cl (2p) x-ray photoelectron spectrum exposed to air-saturated 0.5M NaCl, pH 8.2 at 298K (25°C); E_{appl} = 0V.

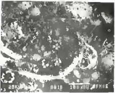

Figure 67a. Scanning electron micrograph of a corroded Monel-400 alloy sample exposed to air-saturated 0.5M NaCl, pH 8.2 at 298K (25°C) for 24 hours at 0V (Ag/AgCl). Micrograph obtained before washing the sample

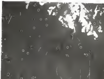

Figure 67b. Scanning electron micrograph of a corroded Monel-400 alloy sample exposed to air-saturated 0.5M NaCl pH 8.2 at 298K (25°C) for 24 hours at 0V (Ag/AgCl). Micrograph obtained after washing the sample

Figure 68 shows the micrographs obtained at a higher magnification. Figure 68a was obtained before washing. The white residue described in Fig. 67a can be seen here to have star-like crystal structure. These crystals dissolved during washing as shown by their absence in Fig. 68b. The pit morphology can be clearly seen in the high magnification micrographs. They are not the shallow type of pits. The micrographs of the dendrite-type structure was obtained at 10,000X as shown in Fig. 69. The structure appears to have grown crystallographically as depicted by what appears to be crystallographic lines radiating from one point. The structure also appears to have shallow pores probably terminating at the underlying corrosion products.

EDX spectra were obtained from the four locations - star-like crystals, the underlying corrosion film, the dendrite structures and inside the pits. Figures 70-73 display the representative spectra. The analysis of the white crystals has shown that they contain large amounts of sodium and chloride, confirming the earlier speculation that they are salt crystals (Fig. 70). The small amounts of Ni and Cu shown probably came from the underlying crystals.

Figure 71 shows the spectrum obtained from the inner corrosion products. In addition to Cu and Ni, Fe and Mn peaks are present. This is the only technique able to show the presence of Fe and Mn. The dendrite structures found on some parts of the sample surface (see Fig. 69) were also analyzed. Figure 72 is the spectrum obtained from these structures. Cu, Ni, Fe and Mn are also present in this film. The spectrum obtained inside the pit is displayed in Fig. 73. The four

Figure 68 shows the micrographs obtained at a higher magnification. Figure 68a was obtained before washing. The white residue described in Fig. 67c can be seen here to have star-like crystal structure. These crystals dissolved during washing as shown by their absence in Fig. 68b. The pit morphology can be clearly seen in the high magnification micrographs. They are not the shallow type of pits. The micrographs of the dendrite-type structure was obtained at 10,000X as shown in Fig. 69. The structure appears to have grown crystallographically as depicted by what appears to be crystallographic lines radiating from one point. The structure also appears to have shallow pores probably terminating at the underlying corrosion products.

EDX spectra were obtained from the four locations - star-like crystals, the underlying corrosion film, the dendrite structures and inside the pits. Figures 70-73 display the representative spectra. The analysis of the white crystals has shown that they contain large amounts of sodium and chloride, confirming the earlier speculation that they were salt crystals (Fig. 70). The small amounts of Ni and Cu shown probably came from the underlying crystals.

Figure 71 shows the spectrum obtained from the inner corrosion products. In addition to Cu and Ni, Fe and Mn peaks are present. This is the only technique able to show the presence of Fe and Mn. The dendrite structures found on some parts of the sample surface (see Fig. 69) were also analyzed. Figure 72 is the spectrum obtained from these structures. Cu, Ni, Fe and Mn are also present in this film. The spectrum obtained inside the pit is displayed in Fig. 73. The four

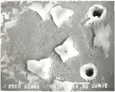

Figure 68a Scanning electron micrograph of a corroded Monel 400 alloy sample exposed to air-saturated 0.5M NaCl, pH 8.2 at 298K (25°C) for 24 hours at 0V (Ag/AgCl). Micrograph obtained at higher magnification and before washing. Star-like crystals are NaCl crystals.

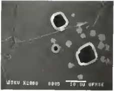

Figure 68b Scanning electron micrograph of a corroded Monel-400 alloy sample exposed to air-saturated 0.5M NaCl, pH 8.2 at 298K (25°C) for 24 hours at 0V (Ag/AgCl) Micrographs showing pits was obtained at higher magnification after washing the sample

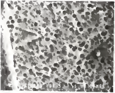

Figure 69 Scanning electron micrograph of a corroded Monel-400 alloy sample exposed to air-saturated 0.5M NaCl, pH 8.2 at 298K (25°C) for 24 hours at 0V (Ag/AgCl). Micrograph obtained after washing

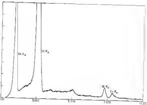

Figure 70 EDX spectrum for the star-like crystals found on the surface or corroded Monel-400 alloy

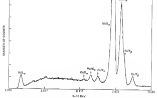

Figure 71 EDX spectrum obtained from the surface of a corroded Monel-400 alloy

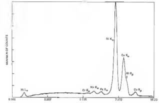

Figure 72 EDX spectrum of the dendrite-like structure on the surface of a corroded Monel-400 alloy.

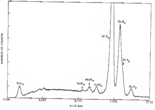

Figure 73 EDX spectrum obtained inside a pit on a corroded Monel-400 alloy.

elements found in the corrosion films are also shown in the spectrum. From the peak heights and the comparison of Cu/Ni ratios obtained in the pits and other locations (Table V), it can be seen that the concentration of copper is higher in the pit than at other locations. This is in agreement with the results reported by Urgansky et al.[56] and Bird and Moers[57] who found higher concentrations of copper in the pits of Monel-400 alloy parts that failed in service. This observation and the others referred to above point to possible role of copper in the pitting corrosion of Monel-400 alloy. It appears that a high concentration of copper ions builds up inside the pit which, after reaching a critical concentration, redeposits to provide copper-rich layer in the pit.

In summary, the effects of copper on the behavior of the alloy as reported here is somewhat different from what has been widely reported in the literature for the chloride concentration (0.5M) used in this study. In deaerated solutions, copper (II) ions have been generated at a much lower potential (-100 mV) than has been widely reported. Both Cu(II) and Cu(I) ionic species have been monitored at all potentials investigated in air-saturated NaCl solution with the proportion of Cu(II) species considerably larger than that of Cu(I) species in the low over-potential region.

The open-circuit steady state potential (determined after 24 hours exposure) in air-saturated solution is -58 mV. Since Cu(II) species dominates at the low over-potential region, it can be logically concluded that during natural corrosion, the soluble dissolution products of copper from the alloy are predominantly Cu(II) ionic species. Assuming

Table 9 Semiquantitative Elemental Ratios Obtained at Three Locations On Anodized Monel 400 Alloy Surface Air-saturated 0.5M NaCl

Location	Cu/Ni	Fe/Ni	Mn/Ni
Pits	0.42	0.02	0.02
Surface	0.33	0.02	0.03
Dendrite-like Structure	0.32	0.02	0.03

this to be the case, the role of copper in the pitting behavior of Monel-400 alloy becomes clearer.

If the generated cupric ions accumulate at the interface, as one would expect under slow fluid flow or stagnant conditions, a concentration will be reached such that the solubility product of basic copper chloride ($CuCl_2 \cdot 3\ Cu(OH)_2$) (atacamite) is exceeded. This green compound then precipitates out. As Evans[113] postulated, growth of the precipitated crystal nuclei depletes the concentration of Cu(II) ions at the growth sites. The decreased Cu(II) ion concentration makes the sites anodic to the surrounding areas. The ensuing increased anodic dissolution at these points produces pits. Further growth of the pits may be sustained by autocatalytic mechanism proposed by Galvele[205]. That is, hydrolysis of Cu(II) and Ni^{2+} ions inside the pits causes acidification of the electrolyte at the bottom of the pits. The increased acidity prevents the formation of a passive film at the bottom of the pits, thus sustaining metal dissolution in the pits.

On the other hand, higher concentration of copper dissolution products in the pits than in the surrounding bulk solution, as evidenced by the data shown in Table 9, can sometimes lead to metal ion concentration cells. Since, in the case of copper, the area with low concentration of metal ions becomes anodic, and as speculated in Chapter II, increased metal dissolution occurs at the periphery of the pits while dissolution inside the pits slows down or stops completely. This causes widening of the pits leading to shallow trenched structures sometimes observed on pitted Monel-400 alloy and some copper base alloy surfaces. Green gelatinous precipitate has been found hanging from the surface of the sample polarized for 24 hours in the air-saturated solution. This probably is the atacamite. This hypothesis may be used to explain the various forms of pit morphology found on Monel-400 alloy.

Now that the probable mechanisms by which pits initiate and propagate on Monel-400 alloy have been proposed, attention can be directed at measures necessary to control pitting in this alloy. As the foregoing discussion has elucidated, any effective control measures will have to focus on reducing or preventing the build up of cupric ions at the corroding surface/liquid interface. This may not be an easy task if one considers exposure to seawater under slow flowing and/or stagnant conditions. For exposure under these conditions, the only logical step is to reduce the amount of copper in the alloy (and substitute it with another alloying element possibly iron) addition without impairing the beneficial effects of copper in the alloy such as making the alloy nobler.

For closed systems such as in heat exchange tubes or where a small body or volume of salt water is needed, other measures such as addition of inhibitors that will act to tie down cupric ions and thus prevent the attainment of critical concentration of this cations for the formation of atacamite may help. Moreover, since critical concentrations of Cl^- and OH^- are also required and the presence of oxygen is needed to form atacamite, reducing the concentration of any of O, Cl and OH^- ions may prevent the formation of atacamite.

Another question raised in this study is the concept of a critical pitting potential which was a topic of a recent debate between LaQue and Uhlig[206]. As reported earlier, potential scanning was stepped at +400 mV because pits developed on the working electrode beyond +400 mV at a potential scanning rate of 5 mV/sec. Holding the electrode potential at 0 V overnight, however, led to the formation of pits as shown in Figs. 66 and 67. If, as it appears from these results, the critical pitting potential is dependent on the potential traverse rate, then its engineering application is questionable and risky.

CHAPTER V
CONCLUSIONS

On the basis of the analysis of data generated in this study, it can be concluded that:

1. Pitting corrosion of Monel-400 alloy in seawater under slow flowing and/or stagnant conditions is associated with the build-up of cupric ions at the corroding surface/solution interface. The pitting behavior of this alloy under the above conditions has hitherto been linked to oxygen starvation which hindered the self-healing ability of the passive film. Oxygen does not participate directly in the formation of passivating films. What it does is that its reduction produces OH⁻ ions which stabilize the film. In seawater, which is highly buffered and which dissolves but very little oxygen because of its high salt content, reduction of oxygen should not cause any significant change in pH. Oxygen starvation, therefore, may not be the only cause of pitting in seawater.

2. Pitting corrosion of Monel-400 alloy may be controlled by preventing a buildup of cupric ions at the corroding surface/solution interface. This may be accomplished by reducing the amount of copper in the alloy and/or alloy additions. For closed systems or exposure involving a small body of solution, inhibitor additions to tie the cupric ions down or reducing the concentration of Cl^- or OH^- ions or both may help.

3. The anodic dissolution of Monel-400 alloy is strongly mass transport dependent in Na_2SO_4 solution. The behavior is associated with mass transport dependence of the formation of insoluble reaction products.

4. Electrochemical evidence has confirmed that Cu(I) ions are stable long enough in Na_2SO_4 solution to be detected on a collector electrode. That they are not detected during dissolution of Monel-400 alloy is proof that the dissolution of copper in the alloy is directly to Cu(II) ions.

5. Dissolution of Monel-400 alloy does not show significant mass transport dependence in NaCl solutions under the flow conditions studied.

6. Contrary to the widely held opinion, Cu(II) ions are generated in the presence of high concentrations of chloride ions at much lower overpotentials than have been reported hitherto. This finding renders suspect any conclusions from data interpreted on the basis of the assumption that only Cu(I) species are generated.

7. Comparison of data obtained in both deaerated and air-saturated solutions strongly indicates that a more resistant film exists on the sample polarized in the presence of oxygen. The inner film formed in air-saturated solution is NiO while indications are that the film formed in deaerated solution is Ni_3O_4. The suggestion is that NiO may be more protective than Ni_3O_4.

8. Indications from data analysis are that Monel-400 alloy corrosion behavior is associated with the dissolution kinetics of copper in the alloy.

CHAPTER VI
RECOMMENDATIONS FOR FURTHER STUDIES

The behavior of materials in pure NaCl solutions may be different from their behavior in natural seawater because of the presence of other chemicals and biological activities in seawater. It is, therefore, recommended that the experiments reported here be repeated in natural seawater before studying pitting corrosion in seawater.

The static pitting experiment described has produced only the deep pit type morphology. There is likelihood that the shallow type of pit morphology is associated with fluid flow conditions. It is recommended that pitting studies be done under different flow conditions in order to define flow conditions that promote this type of pit morphology. This study should be coupled with systematic study of the evolution of corrosion morphology to see if there is any relationship between surface corrosion morphology and the location and type of pit morphology.

The failure of the RRDE technique to characterize the nickel soluble reaction products is a major shortcoming of this study. Further experiment is needed to produce data on nickel to augment the data reported here. A more systematic potentiostatic experiment in conjunction with solution analysis using AAS should provide such data.

In situ analysis of insoluble reaction products is still an area of great interest. Following the formation of these products at different stages of development would provide additional insight into the mechanisms of surface reactions. Sample transfer and handling problems have reduced the ability of the XPS technique used in this study (as is currently setup) to provide such information. The possibility of acquiring a corrosion cell that could be used in the sample treatment chamber of the spectrometer for future studies should be pursued vigorously.

In the light of the observation recorded here, that the corrosion behavior of Monel-400 alloy is closely associated with copper dissolution kinetics, and considering that reduction of the amount of copper in the alloy has recommended as a measure for controlling pitting corrosion in Monel-400, it is recommended that the concentration of copper be varied up to approximately 20 w/o below the concentration normally encountered in the alloy. This would provide more information on the influence of copper and what effect the reduction in its contents would have on the overall corrosion performance of the alloy. Such a study should include long time exposure to natural seawater environments under different flow conditions to know whether reduced copper content would worsen the susceptibility of the modified alloy to biofouling and/or reduce its resistance to impingement attack.

The effect of iron content on the corrosion behavior of this alloy is not well known. Iron content, both in solid solution and in precipitated form need to be thoroughly investigated since it has been shown that in the same concentration present in Monel-400 alloy, iron is very beneficial to the corrosion resistance of copper base Cu-Ni alloys

The precipitation of atacamite has been linked to pit initiation The techniques used in this study could not identify the presence of this compound on or in the corrosion film Longer exposure time might provide sufficient corrosion product for conventional x-ray diffraction analysis which has been successfully used to identify atacamite[71]

BIBLIOGRAPHY

1. G. Okamoto and H. Sato, Trans. Japan Inst. Metals, Vol. 1, 16 (1980)

2. N. Sato and G. Okamoto, J. Electrochem. Soc., Vol. 110, No. 6, 605 (1963).

3. J. L. Weininger and M. W. Breiter, J. Electrochem. Soc., Vol. 110, No. 6, 484 (1963).

4. N. Sato and G. Okamoto, Trans. Japan Inst. Metals, Vol. 2, 113 (1961)

5. E. Kunze and K. Schwabe, Corrosion Science, Vol. 4, 109 (1964).

6. B. MacDougall and M. Cohen, J. Electrochem. Soc., Vol. 121, No. 9, 1152 (1974)

7. B. MacDougall and M. Cohen, J. Electrochem. Soc., Vol. 123, No. 2, 191 (1976).

8. B. MacDougall and M. Cohen, J. Electrochem. Soc., Vol. 123, No. 12, 1783 (1976).

9. B. MacDougall, D. F. Mitchell and M. J. Graham, Corrosion, Vol. 38, 85 (1982).

10. R. L. Cowan and R. W. Staehle, J. Electrochem. Soc., Vol. 118, No. 4, 557 (1971).

11. J. O'M. Bockris, A. K. N. Reddy and B. Rao, J. Electrochem. Soc., Vol. 113, No. 11, 1133 (1966)

12. G. W. D. Briggs and W. F. K. Wynne-Jones, Electrochim. Acta, Vol. 7, 241 (1962).

13. T. E. DeGromoboy and L. L. Shreir, Electrochim. Acta, Vol. 11, 895 (1966).

14. D. E. Davis and W. Barker, Corrosion, Vol. 20, 47 (1964).

15. M. Turner, G. E. Thomson and P. A. Brook, Corrosion Science, Vol. 13, 895 (1973)

16. W. J. Muller, Monatsh. Chem., Vol. 48, 426 (1927).

17. N. Sato and G. Okamoto, J. Electrochem. Soc., Vol. 111, 897 (1964)

18. M. L. Kronenberg, J. C. Banter, E. Yeager and F. Hovorka, J. Electrochem. Soc., Vol. 110, No. 9, 1007 (1963).

19. A. Bengali and Ken Nobe, J. Electrochem. Soc., Vol. 122, No. 7, 1118 (1975).

20. M. B. Ives and M. Ramin, J. Electrochem. Soc., Vol. 121, No. 9, 1141 (1974).

21. J. V. Petrocelli and G. A. DiBari, J. Electrochem. Soc., Vol. 112, No. 1, 99 (1965).

22. "The Corrosion Handbook", H. H. Uhlig ed., John Wiley and Sons, New York, 1948.

23. W. Z. Friend, "Corrosion of Nickel and Nickel-Base Alloys", John Wiley and Sons, New York, 1980.

24. C. R. Southwell, and A. L. Alexander, Materials Protection, Vol. 8, No. 3, 39 (1969).

25. F. W. Fink and W. K. Boyd, "The Corrosion of Metals in Marine Environments", Bayer & Co., Inc., Columbus, Ohio, 1970.

26. F. L. LaQue, J. Amer. Soc. Naval Engrs., Vol. 53, 29 (1949)

27. P. M. Thomas and H. A. Humble, Corrosion, Vol. 8, 50 (1952).

28. J. B. Naylor, Anticorrosion, July 1978, p. 3

29. H. H. Uhlig, Record of Chemical Progress, Vol. 7, 56 (1946)

30. H. H. Uhlig and J. Osterward, J. Electrochem. Soc., Vol. 108, No. 6, 515 (1961)

31. H. H. Uhlig and T. Koizumi, J. Electrochem. Soc., Vol. 121, No. 9, 1132 (1974).

32. F. Mansfeld and H. H. Uhlig, Corrosion Science, Vol. 9, 377 (1969).

33. H. H. Uhlig, Record of Chemical Progress, Vol. 3, 3 (1946).

34. H. H. Uhlig and J. Wulff, Transaction of the American Institute of Mining, Metallurgical and Petroleum Engineers, Vol. 135, 494 (1939).

35. F. Mansfeld and H. H. Uhlig, J. Electrochem. Soc., Vol. 115, 900 (1968).

36. N. Stolica and H. H. Uhlig, J. Electrochem. Soc., Vol. 110, 1215 (1963).

37. H. H. Uhlig, F. Mansfeld and M. Kesten, Z. Physic. Chem., N. F., Vol. 74, 216 (1971).

38. H. H. Uhlig, Electrochim. Acta, Vol. 16, 1939 (1971).

39. F. Mansfeld and H. Uhlig, J. Electrochem. Soc., Vol. 117, 427 (1970).

40. R. Landau and C. S. Oldach, Trans. Electrochem. Soc., Vol. 81, 521 (1942).

41. G. Trabanelli, F. Zucchi and L. Felloni, Corrosion Science, Vol. 5, 211 (1965).

42. S. Hettiarachchi and T. P. Hoar, Corrosion Science, Vol. 19, 1059 (1979).

43. C. J. Semino, P. Pedeferri, G. T. Burstein and T. P. Hoar, Corrosion Science, Vol. 19, 1069 (1979).

44. D. W. Rahoi, R. C. Scarberry, R. J. Crum and P. E. Morris, Journal of Engineering for Power, Transactions of the American Society of Mechanical Engineers, January, 1973, p. 27.

45. M. Kiyoshige and T. Yamane, Z. Metal, Vol. 70, 392 (1979).

46. N. S. McIntyre, T. E. Rummery, M. G. Cook and D. Owen, J. Electrochem. Soc., Vol. 123, No. 8, 1164 (1976).

47. M. Cohen, "Modern Techniques in Corrosion Research, Basic and Applied Research, NACE, Houston, Texas, 1969.

48. F. M. Reinhart and J. F. Jenkins, Proceedings, Third International Congress on Marine Corrosion and Fouling, Gaithersburg, Maryland, p. 536 (1972).

49. L. L. Shreir, "Corrosion 1, Metal/Environment Reactions", 2nd Edition, 1977, Newnes-Butterworths, London,

50. C. V. Brouillette, Corrosion, Vol. 14, 16 (1958).

51. Siro Sato, J. Japan Inst. Metals, Vol. 27, No. 3, 134 (1963).

52. Y. Takase, J. Shimizu, S. Maru, M. Tomori and Y. Matsuda, Corrosion Science, Vol. 16, 159 (1976).

53. F. M. Reinhart, Naval Civil Engineering Lab., Port Hueneme, California, Technical Note N-915 (August, 1967)

54. R. May, Trans. Inst. of Marine Engineers, Vol. 49, No. 8, 1937

55. C. F. Nixon, Trans. Electrochem. Soc., Vol. 42, 1924 (297)

56. G. M. Ugiansky and G. A. Ellinger, Corrosion, Vol. 24, 134 (1968).

57. D. B. Bird and K. L. Moore, Materials Protection Vol. 1, No. 10, 70 (1962)

58. "Cupro-Nickel Condenser Tubes Effect of Minor Constituents (Iron and Manganese)", British Non-Ferrous Metals Research Association, Publication D-31, January, 1939.

59. F. L. LaQue, Discussion on Corrosion of Copper-Nickel Alloys in Seawater, Proc. ASTM, Vol. 45, 613 (1945).

60. A. W. Tracy and R. L. Hungerford, Effect of the Iron Content of Cupro-Nickel on Its Corrosion Resistance in "Sea Water", Proc. ASTM, Vol. 45, 591 (1945)

61. G. L. Bailey, J. Inst. Metals, Vol. 79, 243 (1951)

62. W. C. Stewart and F. L. LaQue, Corrosion, Vol. 8, 259 (1952).

63. L. J. Swartzendruber and L. H. Bennett, Scripta Metallurgia, Vol. 2, 93 (1968)

64. R. F. North, "The Protection of Copper by Ferrous Sulfate Additions", NRL-67-PR-22, Olin Mathieson Chemical Corporation, New Haven, Connecticut (July, 1967).

65. R. F. North and M. J. Pryor, Corrosion Science, Vol. 8, 149 (1968)

66. R. F. North and M. J. Pryor, Corrosion Science, Vol. 9, 509 (1969)

67. R. Gasparini, C. Della Roke and E. Ioannilli, Corrosion Science, Vol. 10, 157 (1970).

68. R. F. North and M. J. Pryor, Corrosion Science, Vol. 10, 297 (1970).

69. J. M. Popplewell, R. J. Hart and J. A. Ford, Corrosion Science, Vol. 13, 295 (1973).

70. H. W. Pickering, C. Kato, J. E. Castle and H. G. Ateye, J. Electrochem. Soc., Vol. 127, No. 9, 1890 (1980).

71. H. W. Pickering, C. Kato, J. E. Castle and H. G. Ateye, J. Electrochem. Soc., Vol. 127, No. 9, 1897 (1980).

72. P. A. Parrish, Master's Thesis, University of Florida, 1970.

73. M. Pourbaix, L. Klimzack-Mathieu, C. Mertens, J. Meunier, C. Vanleugenhaghe, L. de Munck, J. Laureys, L. Neelemans and M. Warzee, Corrosion Science, Vol. 3, 239 (1963).

74. E. D. Verink, Jr. and T. S. Lee, III, "Influence of Minor Alloy Additions on the Passive Behavior of Binary Cu-Ni Alloys", Proc., Third International Congress on Marine Corrosion and Fouling, P. 241 (1972); T. S. Lee, III, Master's Thesis, University of Florida, 1972.

75. Calvert and Johnson, J. Chem. Soc., Vol. 19, 436 (1886).

76. W. A. Tilden, J. Chem. Ind., Vol. 5, 84 (1888).

77. J. O. Arnold, The Engineer, Vol. 85, 363 (1898).

78. G. D. Bengough and R. M. Jones, J. Inst. Metals, Vol. 6, 279 (1911).

79. O. B. Desch and S. Whyte, J. Inst. Metals, Vol. 10, 304 (1913).

80. W. E. Gibbs, R. B. Smith and G. D. Bengough, J. Inst. Metals, Vol. 15, 37 (1916).

81. G. D. Bengough, R. M. Jones and R. Pirret, J. Inst. Metals, Vol. 23, 65 (1920).

82. Discussion by G. D. Bengough and R. May of Paper by R. B. Abrams, Trans. Amer. Electrochem. Soc., Vol. 42, 39 (1922).

83. G. D. Bengough and R. May, J. Inst. of Metals, Vol. 32, 169, (1924).

84 F. Taylor and J. W. Wood, Engineering, Vol. 149, 58 (1940). referenced by No.

85 R. G. Shindy and M. J. Pryor, Corrosion Science, Vol. 12, 65 (1972).

86 J. I. Gardiazabal and J. R. Galvele, J. Electrochem. Soc., Vol. 127, No. 2, 259 (1980).

87 W. H. Bassett, Chemical and Metallurgical Engineering, Vol 27, 340 (1922).

88 J. M. Bialosky, Corrosion and Metal Protection, Vol. 4, 15 (1947).

89 H. Gerischer and R. Rickert, Z. Metal, Vol. 46, 681 (1955)

90. L. E. Tabor, Transactions of the Water Works Association, Vol. 48, 239 (1963)

91. S. S. Gastev, Izvest. Akad. Nauk. SSR. Metally , Vol. 3, (1965

92. B. T. Rubin, Ph.D. Dissertation, university of Pennsylvania, 1969

93. H. W. Pickering and C. Wagner, J. Electrochem. Soc., Vol. 114, No. 7, 698 (1967)

94 H. W. Pickering and P. J. Byrne, J. Electrochem. Soc., Vol. 118, No. 2, 209 (1971).

95 H. W. Pickering and Y. S. Kim, Corrosion Science, Vol. 22, No. 7, 621 (1982).

96. M. J. Pryor and Kar-Kheng Giam, J. Electrochem. Soc., Vol 129, No. 10, 2157 (1982).

97. M. J. Pryor, J. Electrochem. Soc., Vol. 130, No. 7, 1625 (1983)

98. E. S. Dixon, Bulletin ASTM, No. 102, p. 21 (1940)

99 F. L. Rhead, J. Inst. Metals, Vol. 2, 73 (1909)

100 W. R. Evans, In Discussion of the Paper by A. Philip, Trans. Faraday Society, Vol. 11, 244 (1915)

101. G. D. Bengough and O. F. Hudson, J. Inst. Metals, Vol. 21, 37 (1919)

102. H. C. Abrams, Trans. Amer. Electrochem. Soc., Vol. 42, 39 (1922).

103. C. F. Nixon, Trans. Amer. Electrochem. Soc., Vol. 45, 237 (1924)

104. F. H. Rhodes and J. T. Carly, Industrial and Engineering Chemistry, Vol. 17, 909 (1925)

105. W. Lynes, Proceedings of the ASTM, Vol. 49, 859 (1941).

106. K. Hashimoto, W. Ogawa and S. Shimodaria, J. Japan Inst. Metals, Vol. 26, 160 (1963)

107. R. M. Horton, Corrosion, Vol. 26, 160 (1970)

108. V. F. Lucey, British Corrosion Journal, Vol. 1, 9 (1965).

109. H. Sugawara and H. Ebiko, Corrosion Science, Vol. 7, 513 (1967)

110. S. C. Britton, J. Inst. Metals, Vol. 67, 119 (1941)

111. C. W. Stillwell and E. S. Turnipseed, Industrial and Engineering Chemistry, Vol. 2, 740 (1934)

112. F. W. Fink, Trans. Electrochem. Soc., Vol. 75, 441 (1939)

113. V. R. Evans, "The Corrosion and Oxidation of Metals," Edward Arnold and Co., London, 1946.

114. G. T. Colegate, Metal Industry, Vol. 73, 531 (1948).

115. L. Kenworthy and W. G. O'Discoll, Corrosion Technology, Vol. 2, 247 (1955)

116. L. Piatti and R. Grauer, Werkstoffe und Korrosion, Vol. 14, 551 (1963)

117. H. G. Feller, Corrosion Science, Vol. 8, 259 (1968).

118. E. D. Verink, Jr. and P. A. Parrish, Corrosion, Vol. 26, 5 (1970).

119. R. H. Heidersbach, Jr. and E. D. Verink, Jr., Corrosion, Vol. 28, No. 11, 397 (1972).

120. E. D. Verink, Jr. and R. H. Heidersbach, Jr., Special Technical Publication 516, ASTM, Philadelphia, 1972.

121. A. H. Heese, E. T. Myskowski and B. M. Loring, Trans. Amer. Foundrymen's Association, Vol. 51, 821 (1944)

122. M. Schussler and D. S. Napolitan, Corrosion Vol. 12, 107 (1956).

123. A. W. Tracy, ASTM STP, Vol. 175, 67 (1956).

124. A. C. Hamstead, Industrial and Engineering Chemistry, Vol. 50, 87A (1958).

125. L. W. Gleekman and R. K. Swandby, Corrosion, Vol. 17, 144t (1961).

126. B. F. Peters, J. A. K. Carson and R. D. Barer, Materials Protection, Vol. 4, 24 (1965).

127. J. Serre and J. Lawreys, Corrosion Science, Vol. 2, 135 (1965).

128. L. M. Lesdoe, Journal of the American Water Works Association, Vol. 38, 1352 (1946).

129. M. G. Fontana, Industrial and Engineering Chemistry, Vol. 39, 87A (1947).

130. W. D. Clark, J. Inst. Metals, Vol. 73, 263 (1947).

131. P. Trautzel and W. D. Treadwell, Helvetica Chimica Acta, Vol. 34, 1723 (1951).

132. J. I. Fisher and J. Halpern, J. Electrochem. Soc., Vol. 103, 282 (1956).

133. H. W. Pickering, J. Electrochem. Soc., Vol. 115, No. 2, 143 (1968).

134. R. Bakish and W. D. Robertson, Trans. AIME, Vol. 206, 1278 (1956).

135. L. Graf, Metallwirtschaft, Vol. 11, 77 (1932); referenced from No. 93.

136. L. Graf, Korrosion u. Metallschutz, Vol. 11, 34 (1935); referenced from No. 135.

137. D. S. Keir and M. J. Pryor, J. Electrochem. Soc., Vol. 127, No. 10, 2138 (1980).

138. Y. Sicuratnik, Soviet Electrochemistry, Vol. 13, 8 (1978).

139. W. C. Fort, III, Ph.D. Dissertation, University of Florida, 1975.

140. J. E. Finnegan, Ph.D. Dissertation, University of Florida, 1981.

141 W. G. Feller, Habilitationsschrift, Technische Universitat Berlin (1965).

142 H. W. Pickering and P. R. Swann, Corrosion, Vol. 19, 373t (1963)

143 M. Stern, Corrosion, Vol. 14, No. 7, 329t (1958).

144. M. Prazak, Collec. Czech. Chem. Comm., Vol. 25, 1126 (1960)

145 R. F. Steigerwald and N. D. Greene, J. Electrochem. Soc., Vol. 109, No. 11, 1026 (1962)

146. J. C. Scully, "The Fundamentals of Corrosion," 2nd Edition, Pergamon Press, Oxford, 1975.

147 E. Matteson and J. O'M. Bockris, Transactions Faraday Society, Vol. 55, 1586 (1959),

148 J. O'M. Bockris and B. E. Conway, Journal of Chemical Physics, Vol. 28, 707 (1956).

149 O. R. Brown and H. R. Thirsk, Electrochim. Acta, Vol. 10, 383 (1965).

150 Tor Hurlen, Acta Chemica Scandinavica, Vol. 15, 630 (1961)

151 T. Hurlen and G. Lunde, Electochim. Acta, Vol. 8, 340 (1961).

152. W. Z. Lorenz, Physik. Chem. N. F., Vol. 19, 377 (1959).

153 M. C. Petit, Electrochim. Acta, Vol. 10, 291 (1965)

154. L. M. Nekrasov and M. Berezina, Dokl. Akad., Nauk SSSR, Vol. 142, 855 (1962)

155 D. T. Napp, D. C. Johnson and S. Bruckenstein, Analytical Chemistry, Vol. 39, No. 4, 481 (1967)

156 G. W. Tindall and S. Bruckenstein, Analytical Chemistry, Vol. 40, No. 7, 1051 (1968).

157 J. Jacq, B. Cavalier and O. Bloch, Electrochim. Acta, Vol. 13, 1119 (1968)

158. A. H. Taylor, J. Electrochem. Soc., Vol. 118, 854 (1971)

159 M. E. Walton and P. A. Brook, Corrosion Science, Vol. 17, 317 (1977).

160 Heyn and Bauer, Mitteilungen Koniglichen Materialprüfungsamt, Vol. 28, 93 (1910).

161 D. Armstrong, N. A. Hampson and R. J. Latham, J. Electroanal. Chem., Vol. 23, 361 (1969)

162 R. D. Armstrong, Corrosion Science, Vol. 11, No. 10, 696 (1971)

163 C. D. Wagner, W. M. Riggs, L. E. Davis and J. F. Moulder, "Handbook of X-ray Photoelectron Spectroscopy", G. E. Muilenberg (editor), Perkin-Elmer Corporation, Eden Prairie, Minnesota, 1979.

164 Stephen Evans, The Journal of Chemical Society, Faraday Transactions II, 71 (5), 1055 (1975)

165 T. Novakov and R. Prins, in 'Electron Spectroscopy", ed. D. A. Shirley (North Holland, Amsterdam, 1972), P. 821, also; Solid State Communication, Vol. 9, 1975 (1971).

166 T. Robert, M. Bartel and G. Offergeld, Surface Science, Vol. 33, 123 (1972).

167. Gunnar Schon, Surface Science, Vol. 35, 96 (1973).

168 D. Chadwick and T. Hashemi, Corrosion Science, Vol. 18, 39 (1978)

169. D. C. Frost, A. Ishitani and C. A. McDowell, Molecular Physics, Vol. 24, 861 (1972)

170 N. S. McIntyre and M. G. Cook, Analytical Chemistry, Vol. 47, No. 13, 2208 (1975)

171 Tery L. Barr, The Journal of Physical Chemistry, Vol. 82, No. 16, 1801 (1978).

172 K. S. Kim, Journal of the Electron Spectroscopy, Vol. 3, 217 (1974).

173. R. F. Roberts, Journal of the Electron Spectroscopy, Vol. 4, 273 (1974).

174. K. S. Kim and N. Winograd, Surface Science, Vol. 43, 625 (1974).

175 Yoshio Takasu, Shun-ichi Maru, Yoshiharu Matsuda, and Hazime Shimizu, Bulleting of the Chemical Society of Japan, Vol. 46, No. 1, 219 (1973).

176 N. S. McIntyre, D. G. Zetaruk and D. Owen, J. Electrochem. Soc. Vol. 126, No. 5, 750 (1979)

177 'Methods of Surface Analysis', A. W. Czanderna, editor (Elsevier Scientific Publishing Company) 1975

178 Hassan Windawi and Floyd F. L. Ho, "Chemical Analysis," P. J. Elving and J. D. Winefordner, editors, John Wiley and Sons, New York, 1982, P 89

179 L. D. Hulett, A. L. Bacarella, L. Lidonnici, and J. C. Griess, J. Electron Spectrosc. Vol. 1, 169 (1972/73)

180 Y. Takasu, S. Maru, Y. Matsuda and H. Shimizu, Bull. Chem. Soc. Japan, Vol. 48, No. 1, 219 (1975)

181 S. Okuyama, "The 41st Conference of the Electrochem. Soc. of Japan, Chiba, 1974

182 J. E. Castle, Nature, Vol. 234, 93 (1971)

183 T. Dickinson, A. F. Povey and P. M. Sherwood, J. Chem. Soc. Faraday Trans. 1, Vol. 73, 327 (1977)

184 K. Nakayama, M. Ono and H. Shimizu, J. Vac. Scand. Tech., Vol. 9, No. 2, 749 (1972)

185 M. Tarng and G. K. Wehner, J. Applied Physics, Vol. 42, 2449 (1971)

186 M. Shimizu, M. Ono and K. Nakayama, Surface Science, Vol. 36, 817 (1973)

187 M. Braun and Ken Nobe, J. Electrochem. Soc., Vol. 126, No. 10, 1666 (1979)

188 T. Hurlen, Acta Chem. Scand., Vol. 15, 1231 (1961)

189 St. V. Naray-Szabo and Z. Szabo, Z. Phys. Chem., Vol. 166A, 228 (1933)

190 M. Turner and P. A. Brook, Corrosion Science, Vol. 13, 973 (1973)

191 H. Lal and K. R. Thirsk, J. Chem. Soc., 2638 (1953)

192 L. Stephenson and J. H. Bartlett, J. Electrochem. Soc., Vol. 101, No. 11, 571 (1954)

193 R. S. Cooper, J. Electrochem. Soc., Vol. 103, No. 6, 307 (1956)

194 A. B. Taylor, J. Electrochem. Soc., Vol. 118, 854 (1971)

195. C. M. Benfiglio, N. C. Albaya and O. A. Lahn, Corrosion Science, Vol. 13, 717 (1973).

196. J. O'M. Bockris, B. T. Rubin, A. Despic and B. Lovrecek, Electrochim. Acta, Vol. 17, 973 (1972).

197. A. L. Bacarella and J. C. Griess, Jr., J. Electrochem. Soc., Vol. 120, No. 4, 459 (1973).

198. M. E. Walton and P. A. Brook, Corrosion Science, Vol. 17, 317, 593 (1977).

199. P. A. Lush and M. J. Carr, Corrosion Science, Vol. 19, 1079 (1979).

200. W. M. Latimer, 'The Oxidation States of the Elements and Their Potentials in Aqueous Solutions,' 2nd. ed., (Prentice-Hall), 1952, p. 185.

201. L. L. Shreir, "Corrosion 2, Corrosion Control," 2nd. ed., 1977, Newnes-Butterworths, London.

202. K. K. Platt and P. A. Brook, Corrosion Science, Vol. 11, 185 (1971).

203. R. S. Cooper and J. H. Bartlett, J. Electrochem. Soc., Vol. 105, 109 (1958).

204. M. Akkaya, Master's Thesis, University of Florida, 1982.

205. J. R. Galvele, J. Electrochem. Soc., Vol. 123, No. 4, 464 (1976).

206. F. L. LaQue and H. H. Uhlig, Materials Performance, Vol. 22, No. 8, 34 (1983).

207. "Metals Handbook", 1948 edition, p 1198, American Society for Metals, Metals Park, Ohio.

208. "Metals Handbook", Vol. 10, 8th edition, American Society for Metals, 1975, Metals Park, Ohio.

209. W. M. H. Sachtler and R. Jongepier, J. Catalysis, Vol. 4, 665 (1965).

210. W. M. H. Sachtler and G. J. H. Dorgelo, J. Catalysis, Vol. 4, 654 (1965).

211. T. Takeuchi, M. Sakaguchi and I. Miyoshi, Bull. Chem. Soc., Japan, Vol. 35, 1390 (1962).

212 F. M. Ryan, E. W. Pugh and R. Schmoluchoski, Phys. Rev., Vol. 116, 1106 (1959)

213 J. G. Ambaschian, private Communication

214 V. G. Levich, Acta Physicochim., U.R.S.S., Vol. 17, 257 (1942)

215 A. C. Riddiford, in "Advances in Electrochemistry and Electrochemical Engineering," Vol. 4, P. 47, P. Delahay, editor, Interscience Publisher, Inc., New York (1966)

216 J. A. Ali and J. R. Ambrose, Paper presented at National Association of Corrosion Engineers Conference, 1982 Corrosion Research Symposium, Houston, Texas

217 M. Akkaya and J. R. Ambrose, Paper No. 309, National Association of Corrosion Engineers Conference, 1983, Anaheim, California.

218 N. S. McIntyre and F. W. Stanchell, J. Vacuum Sic. and Tech., Vol. 16, 798 (1979).

219 C. J. Powell in "Quantitative Surface Analysis of Materials", N. S. McIntyre, editor, ASTM-STP-643, ASTM, Philadelphia (1978)

220 M. P. Seah, Surface Interface Anal., Vol. 2, 222 (1980).

APPENDICES

APPENDIX 1
LIST OF EQUIPMENT

1. Tacussel Ring and Disc Electrode Model EAD 400.
2. Tacussel Electronique Asservitex 4000 Speed Controller.
3. Tacussel Electronique Bipotentiostat Model Bi-PAD 3.
4. Tacussel Electronique Function Generator Model GSTP 3.
5. Princeton Applied Research Universal Programmer Model 175.
6. Hewlett-Packard X-Y Recorder Model 7005B
7. Soltec X-Y1Y2 Recorder Model VP-6432S
8. Keithley Digital Multimeter Model 160.
9. Orion Research Digital Ionalyzer Model 801A
10. Haake Constant Temperature Circulator Model NK22.
11. Perkin Elmer Atomic Absorption Spectrophotometer Model 140.
12. Kratos X-ray Photoelectron Spectrometer Model X-SAM-800.
13. Perkin Elmer Differential Ion Gun Model PHI 04-303
14. Perkin Elmer Cylindrical Mirror Analyzer Model PHI 10-150
15. Varian Scanning Ion Gun Model 981-2043.
16. JEOL Scanning Microscope Model JSM35C.
17. EG and G EEDS II Economical Energy Dispersive X-ray System
18. Carl Zeiss Metallograph Model IM 405

APPENDIX 2
SAMPLE CHARACTERIZATION AND [illegible]

The Monel-400 alloy used in this study was supplied by International Nickel Company (INCO). The composition of the alloy determined spectrochemically appear in Table 10. The collector electrode was fabricated out of a glassy carbon block supplied by Astro Scientific International, Inc.

A sample for metallographic analysis was cut from the block of Monel-400 alloy and mounted in epoxy resin. The face perpendicular to the rolling direction (transverse section) was prepared as follows:

a) Successive hand-grinding on silicon carbide (SIC) papers though 240, 320, 400 and 600 grit using water as lubricant and coolant.

b) Successive polishing on Microcloth* through 6μm, 1μm and 0.25μm diamond paste using automatic polishing wheel. Lapping oil was used as lubricant.

The sample was ultrasonically cleaned in soap solution, rinsed in running water and dried between each polishing step. After the final polishing, the sample was thoroughly cleaned ultrasonically in soap solution, rinsed in running water and dried before etching. Etching was done in a solution of 1 part nitric acid (concentrated) and 1 part glacial acetic acid.

---

* Trade name of Buehler Ltd.

Table 14: Composition of Monel-400 Alloy

Ni	66.20% by weight
Cu	31.50% by weight
Mn	1.14% by weight
Fe	0.70% by weight
C	0.17% by weight
Others	0.29% by weight

The microstructure obtained at a magnification of 200X appears in Fig. 74. According to the phase diagram (top of Fig. 75) the alloy is single-phase. But a more recent diagram (bottom of Fig. 75) shows a miscibility gap below 595 K (322°C). The area of the diagram where the miscibility gap exists encompasses the composition of copper and nickel in Monel-400 alloy. Sachtler and R. Jongepier[209] also showed that a miscibility gap existed in Cu-Ni system at low temperatures. They reported that equibrated films of the alloy consisted of crystallites which contained a kernel of almost pure nickel enveloped by copper rich alloy. This observation agrees with earlier reports of the existence of a miscibility gap in Cu-Ni systems.[210-212] Whether the composition of the surface of Monel-400 alloy differs considerably from that in the interior of the alloy cannot be said from the micrograph shown in Fig. 74.

There is a great disparity in the size of the grains in the micrograph. The large grains are said to have probably evolved from strain-induced growth (discontinuous growth).[213] As is typical of the microstructures of most Cu-Ni alloys, numerous twins are seen in this microstructure.

Average grain diameter was determined from line intercept count, P_L. This parameter (P_L) was obtained by superposing a square grid upon the microstructure and counting the number of interceptions with grain boundaries. The counts were taken at 30 randomly selected areas. P_L was calculated by dividing the average number of counts (48.29 ± 4.14) by the total length of the line (0.14 cm). Surface area per unit volume, S_V, is twice the value of the line intercept count ($2\ P_L$), and the

Figure 74. Microstructure of Monel 400 alloy 200X

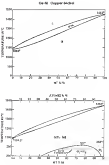

Figure 75 Copper-nickel equilibrium phase diagrams: top (207), bottom (208).

average grain diameter, $\bar{D}$, is $1/P_L$. The following are the values obtained from the microstructure of Fig. 74:

$$P_L = 333.26 \text{ cm}^{-1}$$

$$S_V = 666.52 \text{ cm}^{-1}.$$

$$\bar{D} = 3 \times 10^{-3} \text{ cm}$$

The average grain size (in terms of average distance across the grain) is 3×10^{-3} cm.

The alloy was used as received. The final surface preparation after the electrode had been fabricated was to hand-grind through successive grades of SiC paper down to 400 grit using soap solution as both coolant and lubricant. Then it was degreased in acetone and thoroughly washed in demineralized water, dried and stored in a desiccator. Except for samples for XPS analysis, the final surface finish was 600 grit. The final grinding was done just before polarization. A special polishing surface was used for polishing the electrodes. The schematic of the polishing disc is shown in Fig. 76. The polishing technique involved rotating the electrode (mounted on the rotating spindle) while polishing on a fixed disc surface. This technique was selected over the conventional polishing technique, in which the sample is polished on a rotating polishing surface, in order to minimize transfer of materials between the central electrode and the collector ring electrode.

During preliminary XPS studies it was found that the signals for Fe and Mn were too weak to provide information on their oxidation states and concentration at the surface. In order to improve the sensitivity of the technique, a final surface finish of $6 \mu m$ was used. In addition, the number of scans (sweeps) was increased from 20 cycles to 50 cycles

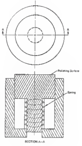

Figure 76 Schematic drawing of the sectioned polished jig.

APPENDIX 3
ELECTROCHEMICAL EQUIPMENT

Development of rotating disc electrode (RDE), the basic theory of which was published by Levich[214] in 1942, has evolved into a versatile technique for the study of many electrode processes. Its use in conjunction with a ring collector electrode, which surrounds it and isolated from it, represented a major breakthrough for study of metal dissolution kinetics. With this configuration, in-situ measurement of dissolution rates for alloy constituents becomes possible. Knowing the fraction of overall anodic current going into the generation of soluble reaction products, the anodic partial current for film formation can be inferred Being able to separate overall corrosion process into its component parts not only puts the mechanism of propagation into perspective but also can be used to identify those components which control the process and toward which remedial action can be directed. In addition to providing information on the concentration of soluble reaction products and indirectly on charge for the formation of insoluble reaction products, it also provides information on the dependence of an electrochemical process on relative fluid flow velocity. An excellent review on the theory of this technique can be found in reference 215.

Two rotating electrode configurations, the ring-ring (RRE) and the ring-disc (RDE), were used. In the ring-ring configuration, the use of which was first reported by Ali and Ambrose,[216] a glassy carbon ring electrode is positioned concentrically outside the Monel-400 alloy specimen ring under a separate potential control (Fig. 77). The other configuration is the conventional ring-disc system in which the central disc electrode is of Monel-400 alloy.

The major reason for selecting the ring-ring electrode configuration is to minimize disproportionation reaction or any other effect which results from soluble reaction products generated at the center of a disc electrode effecting reactions occurring at the outer edge of the disc. Other advantages of this configuration over the conventional ring-disc configuration have been discussed elsewhere.[217]

The electrode used was Tacussel Ring and disc electrode Model EAD 400 (Fig. 78). The electrode consist of two sections - the motor section and a rotating shaft. The motor, housed in a compact anodized aluminum body, is a direct drive type propelled by a servo system. The motor is capable of rotational speeds up to 4000 rpm with a resolution of ± 4 rpm and an accuracy of speed control of ± 10 rpm. Tacussel Electroniques Asservitex 4000 Speed Controller was used to control the rotation speeds of the electrode.

The rotating shaft was housed in Kel-F body which also contains a motor coupling and two contact brushes. The active electrodes are located at the tip of the shaft outside the Kel-F housing. The shaft was modified to suit the needs of this laboratory. The modified shaft

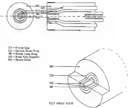

Figure 77. Schematic drawing of the tip section of the rotating ring-ring electrode

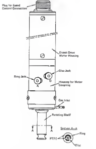
ELECTRODE E.A.D.
Plug for Speed Control Connection
Direct Drive Motor Housing
Disc Jack
Ring Jack
D
A
Housing for Motor Coupling
Gas Inlet
Rotating Shaft
A
A
Section A–A
Ring
PTFE
Disc

Figure 78 Rotating ring-disc electrode assembly attached to the motor drive.

consists of two sections - the rotating shaft coupled to the drive motor and the tip which contains the active electrodes. The electrode tip is coupled to the shaft using 316 stainless steel lock nut. Figure 79 displays the original rotating shaft and the modified shaft and the tip. The experimentally determined collection efficiencies for the two electrodes (ring-ring and ring-disc electodes) are as shown in Tables 11 and 12, respectively. The areas of the electrodes are: Monel-400 alloy ring 0.059 cm^2, carbon ring 0.060 cm^2, Monel-400 alloy disc 0.14 cm^2 and carbon ring 0.17 cm^2.

The potentiostat used for this study is Tacussel Electronique bipotentiostat model Bi-PAD 3 which consists of two circuits for independent potential control of two electrodes (central and collector electrodes). The circuitry eliminates electrical interaction between the two working electrodes and the reference and counter (auxillary) electrodes by providing two completely independent feedback loops. One of the circuits is capable of controlling either potential or current (used for the central electrode) with a maximum potential output of ± 20 V. The other circuit, used for the collector ring electrode, is capable of controlling only potential and has a maximum potential output of ± 10 V.

Two signal generators - Tacussel Electronique function generator model GSTP 3 and PAR Universal Programmer model 175 - were used at one time or the other during the course of the investigation. Two X-y recorders, Hewlett-Packard X-Y recorder model 7005 B and Soltec $X\text{-}Y_1Y_2$ two-pen recorder model VP-6432S, were used in the experiments.

The electrochemical cell used (Tacussel Electronique model XLRC) shown in Fig. 80 is of double wall borosilicate glass construction

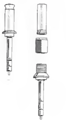

Figure 73 Original and modified rotating ring-ring electrode.

Table 11. Diffusion Currents for the Reduction of $Fe(CN)_6^{-3}$ at the Monel-400 Inner Ring (I_{R1}) and the Oxidation of $Fe(CN)_6^{-4}$ at the Glassy Carbon Outer Ring and the Collection Efficiency N, for the Ring-Ring Electrode

Rotation Speed (rpm)	Inner Ring Current (I_{R1}) μ A	Outer Ring Current (I_R) μ A	I_R/I_{R1} (N)
400	8,583	4,125	0.4800
900	10,950	5,250	0.4795
1200	11,625	5,650	0.4860
1600	12,750	6,250	0.4902
2000	13,725	6,750	0.4918
2500	14,650	7,250	0.4949
2800	15,020	7,500	0.4992
3200	15,700	7,900	0.5032
3600	16,250	8,000	0.4922
4000	16,775	8,220	0.4900

Table 12. Diffusion Currents for the Reduction of $Fe(CN)_6^{-3}$ at the Disc (I_D) and the Oxidation of $Fe(CN)_6^{-4}$ at the Ring (I_R) and the Collection Efficiency, N, for the Glassy Carbon Ring – Monel-400 Disc Electrode

Rotation Speed (rpm)	Disc Current (I_D) μ A	Ring Current (I_R) μ A	I_R/I_D (N)
200	6,187.50	3,550.00	0.5737
400	8,437.50	4,797.00	0.5685
800	10,125.00	5,725.00	0.5654
1200	10,875.00	6,175.00	0.5678
1800	11,562.50	6,500.00	0.5622
2000	12,137.50	6,827.00	0.5623
2400	12,625.00	7,125.00	0.5644
2800	13,025.00	7,375.00	0.5662

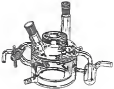

Figure 80. Electrochemical cell.

permitting circulation of temperature regulated fluid between the walls for controlled atmosphere experiments. The working volume of the cell is about 150 ml. The reference electrode, positioned in a separate compartment, mounts parallel to the axis of rotation of the electrode. The Luggin capillary whose tip terminates on the rotation axis of the electrode connects the reference electrode compartment to the cell. On the opposite side (from the reference electrode compartment) of the cell, a side arm, serving as a socket for the counter electrode is angled so as to position the tip of the counter electrode within about 5 cm of the working electrode. An optional sintered glass diaphragm which could be used to chemically isolate the counter electrode from the working electrode compartment was available. This facility was, however, not used in this study.

Both the counter electrode and reference electrode have ground joints to make air-tight seals. An O-ring situated at the neck of the cell, provides an air-tight seal between the electrode and the cell. The cell incorporates gas inlet/outlet ports. The inlet has two ports, one at the bottom of the cell terminating in a gas diffuser which enables gas bubbling through the solution. The second inlet port terminates at the shoulder of the cell above the solution allowing control of the atmosphere above the electrolyte during experiment. A y-joint with a two-way valve permits the selection of which port to use. On the opposite side of the cell is the outlet port which terminates in a solution trap.

APPENDIX 4
TEST SOLUTIONS AND PREPARATION

This study has been conducted in 0.5 M Na_2SO_4 and 0.5M NaCl solutions. All electrolytes were prepared in demineralized water with conductivity 1 x 10^{-6} Ω^{-1} cm^{-1}. The pH of the solutions was adjusted using 0.1M H_2SO_4, 0.1M HCl or 0.1M NaOH. The initial pH used throughout the study was 8.2. All chemicals used were of the analytical grade and were used without further purification. Experiments were performed in both deaerated and air-saturated solutions.

Deaeration of the solution, where applicable, was accomplished in a separated container using standard (prepurified) nitrogen of impurity levels reported in Table 13. The nitrogen was not purified before use. It was, however, dried by passing through Indicating Drierite Laboratory Gas and Air Drying Unit, specified to dry air to a dew point of 200K (100F). This unit was also used to dry air during aeration of the solutions. Deaeration in a separate container was necessary to enable continual adjustment of pH. The solutions were not buffered and their pH changed with time. In all cases, the solutions were deaerated for 1 hour or longer before use. Solution was transferred to the electrochemical cell under nitrogen atmosphere after the final pH adjustment and just before the experiment was begun.

Table 13. Impurity Levels of Prepurified Nitrogen

Water	20 ppm
Oxygen	1 ppm
Argon	35 ppm
H_2	2 ppm
Neon	10 ppm
$C_o + CO_2$	25 ppm
Total Hydrocarbons	0.5 ppm

Circulation of temperature-regulated water between the walls of the electrochemical cell using Haake Constant Temperature Circulator (Model NK22) allowed experiment to be performed at constant solution temperature. Except in cases where the effect of temperature was investigated, all experiments were run at 298 K (25°C).

APPENDIX 5
X-RAY PHOTOELECTRON SPECTROSCOPY

Among the relatively newcomers to the field of surface analysis is the technique of x-ray photoelectron spectroscopy (XPS). It is a highly surface-sensitive technique. The ability to provide information on elemental composition and the chemical nature of surfaces has led to application of this technique in many areas of materials research including corrosion and oxidation, catalysis, lubrication and analysis of organic, ceramic and glass surfaces, to name but a few applications in this field.

The fundamental basis for XPS can be explained with the aid of Fig. 81 (top). When a nearly monoenergetic beam of x-ray photons, hν, strikes an atom in its path, the primary process of interest in this technique is the ejection of electron for each absorption event. All electrons from the orbitals of an atom which have binding energies, E_B, less than the x-ray energy are excited. In accordance with the principle of conservation of energy, the kinetic energy, K.E., of the electron plus the energy needed to remove it from its ground state in the orbital to the vacuum level is equal to the x-ray energy. The kinetic energy is the measured parameter. Knowing the x-ray energy, the binding energy of the electron can be calculated according to the following relation

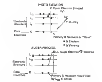

Note. KLL Indicates That The Primary Vacancy Was In the K Shell and That This Was Filled by an L Electron Leading to the Ejection of a Second L Electron

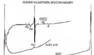

Figure 81 Energy level diagrams and energy distribution N (E) and dN/dE for a silver target

$$EB = \text{[illegible]} - \Delta E + \phi_s$$

where ϕ_s is the spectrometer work function, a correction factor

Figure 82 displays the basic elements of an x-ray photoelectron spectrometer.

Measurement of electron line positions permits identification of an element because of the distinct nature of atomic structure of each element. The binding energies of the core electrons are altered when the number of outer orbital electrons is increased or decreased as a result of chemical reactions. This change in the number of electrons causes a shift in binding energies. The difference in the binding energies of the oxidized state and the reduced or the elemental state is called the chemical shift. This chemical shift is the basis for distinguishing between different oxidation states of elements. This ability of XPS technique to provide chemical state information is its most important feature in its application in corrosion studies.

In addition to the emission of photoelectrons, deexcitation processes also takes place (middle of Fig. 81) leading to the ejection of Auger electrons which can also be measured to provide additional information. This Auger process is different from the conventional Auger process, described in Appendix 6, only in the sense that in the latter case the input probe is a beam of electrons.

Another advantage of XPS technique is that semi-quantitative and quantitative analysis are possible. The quantitative analysis is based on the conversion of intensities to relative compositions. One approach is to use standards[216] and the other relates intensity to composition using electron mean free path and photoelectron cross-section [217, 218]

APPENDIX 6
AUGER ELECTRON SPECTROSCOPY

Auger electron spectroscopy is another surface-sensitive analytical technique widely used in materials science and engineering for applications such as catalysis, corrosion and oxidation, thin film analysis and impurity segregation. Its greatest advantage over XPS technique is its relatively high lateral resolution.

The principle behind the technique consists of bombarding an atom with a beam of electrons (called primary electrons) causing the loss of an electron from the inner K shell of the atom as shown in Fig. 81 (middle). The loss of an electron in the K shell leaves the atom in an excited state. The atom seeks to relieve this excited state by filling the K shell vacancy with an electron from a higher energy shell, say from L_{iii} subshell. In doing so, the L_{iii} electron emits an energy equal to the difference between the energies of the two states. The energy released is either emitted as a photon or transferred to another electron in the same level, another level or another sublevel. In the case illustrated in the middle of Fig. 82, the energy was transferred to an electron in sublevel L_1. The L_1 electron therefore, acquired sufficient energy to be ejected as Auger electron. The transition described here is called $KL_{iii}L_1$ Auger transition, indicating that the

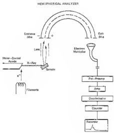

Figure 82. Operation of XPS spectrometer. (From class note.)

primary vacancy was in the K shell. The vacancy was filled by L_{111} electron leading to the emission of L_1 electron. Several transition possibilities, such as KL_1L_{11} or KL_1L_1, etc. can occur with various transition probabilities.

The Auger electron energies are measured and are equal to

$$E_K - E_{L_{111}} - E_{L_1} - \phi_A$$

where ϕ_A is the work function of the analyzer material. Each element has a unique Auger electron energy. This is the basis for elemental identification using this technique. Figure 83 presents the schematic of a cylindrical mirror analyzer. The energy spectrum (NE) shown in Fig. 81 (bottom) stemmed from four different types of emitted electrons from a silver target. Elastically scattered primary electrons give rise to the high intensity peak at 1000 eV. The large background signal in the high energy end of the scale emanated from inelastically scattered primary electrons. The broad energy peak between 0 eV and 100 eV is caused by emitted secondary electrons. Auger spectra are, in practice, presented in differential form ($\frac{dN(E)}{dE}$). This is accomplished electronically to improve signal-to-noise ratio.

The technique is not readily amenable to quantitative analysis. Variation of peak-to-peak amplitude is generally used as a rough estimate of concentration. Ratios of peak-to-peak heights are also used to indicate relative concentrations. Combination of this technique and ion sputtering provides a powerful technique for showing changes in composition as a function of distance from the surface to the bulk.

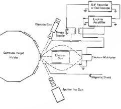

Figure 23. Operation of a cylindrical mirror analyzer as an Auger spectrometer (177)

APPENDIX 7

DETERMINATION OF 'REDOX' POTENTIALS FOR NICKEL, COPPER AND IRON SOLUBLE REACTION PRODUCTS

These are not redox potentials in the true sense of the term since they have been determined potentiodynamically. The procedure used was to make Na_2SO_4 solutions each containing 10^{-3} M Ni^{2+}, Cu^{2+} and Fe^{2+} ions. The solutions were deaerated as described in Appendix 4 and their pH adjusted to 5.2.

For this series of experiments, glassy carbon ring-glassy carbon disc electrode was used. After holding the electrode at an anodic end for a time determined by the attainment of steady-state conditions, the polarization was begun at an anodic end where the current was zero. The potential was scanned to a cathodic end in the diffusion-limited current region. This experiment was repeated at different rotation speeds and for each of Ni^{2+}, Cu^{2+}, Cu^{+}, Fe^{3+} and Fe^{2+}. The results are shown in Figs. 84-88. The potentials of zero currents are referred to here as redox potentials. Potential scanning to the diffusion-limited current region was carried out to determine, especially in the case of copper, where intermediate reactions might take place. Moreover, it was necessary to determine the diffusion-limited plateau region since for ring collection experiment the ring potential had to be maintained

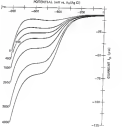

Figure 54. Reduction of nickel on a rotating glassy carbon disc electrode at various rotation speeds. Deaerated 0.5M Na_2SO_4 solution, pH 6.2 containing 10^{-3}M Ni^{2+} ions at 298K (25°C).

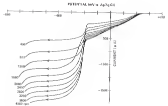

Figure 85 Reduction of copper on a rotating glassy carbon disc electrode at various rotation speeds. Deaerated 0.5M Na_2SO_4, pH 8.2 containing 10^{-3}M Cu^{2+} ions at 298K (25°C).

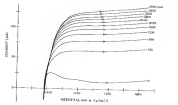

Figure 86 Oxidation of Cu(I) ions on a rotating glassy carbon ring electrode at various rotation speeds. Deaerated 0.5M Na_2SO_4, pH 8.2 at 298K (25°C).

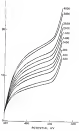

Figure 87 Oxidation of ferrous ions on a rotating glassy carbon disc electrode at various rotation speeds. Deaerated Na_2SO_4 solution, pH 6.2 containing 10^{-3}M Fe^{2+} ions at 298K (25°C).

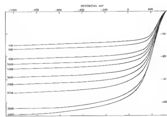

Figure 88. Reduction of ferric ions on a rotating glassy carbon ring electrode at various rotation speeds. Deaerated 0.5M Na_2SO_4, pH 8.2 at 298K (25°C).

at a potential in the diffusion limited region to avoid IR effects and/or other factors shifting the ring potential to a point where current varies with potential.

Copper(I) curves (Fig. 86) were obtained by holding the disc potential at -150 mV to reduce Cu(II) ions at the disc while re-oxidizing the generated Cu(I) ions back to Cu(II) at a linearly swept ring electrode potential. Similar procedure was followed for the determination of F(III) curves (Fig. 88).

BIOGRAPHICAL SKETCH

Joseph Abuna Ageje Ali was born October 27, 1950, at Afah, Benue State Nigeria. He attended private elementary school at Idah, Benue and public secondary school at Dekina, Benue, Nigeria. He attended Western Michigan University for one and one-half years and was graduated from the University of Missouri-Rolla 1978, with the degree of Bachelor of Science in Metallurgical Engineering. He has since attended the University of Florida. He received the degree of Master of Science in Metallurgical and Materials Engineering in 1980. He has pursued the degree of Doctor of Philosophy in the Department of Materials Science and Engineering since that date.

Joseph Abuna Ageje Ali is married to the former Lucy Igo Opeluwa. He is the father of three children, Shaibu Unekuejo, Omitenwuaje Ajanigo and Eigojo Unubi. He is a member of the American Institute of Mining, Metallurgical and Petroleum Engineers, the American Society for Metals, the National Association of Corrosion Engineers, the Electrochemical Society, the American Vacuum Society and Alpha Sigma Mu.

I certify that I have read this study and that in my opinion it conforms to acceptable standards of scholarly presentation and is fully adequate in scope and quality, as a dissertation for the degree of Doctor of Philosophy.

John J. Ambrose, Chairman
Professor of Materials Science
and Engineering

I certify that I have read this study and that in my opinion it conforms to acceptable standards of scholarly presentation and is fully adequate in scope and quality, as a dissertation for the degree of Doctor of Philosophy.

Ellis D. Verink
Professor of Materials Science
and Engineering

I certify that I have read this study and that in my opinion it conforms to acceptable standards of scholarly presentation and is fully adequate in scope and quality, as a dissertation for the degree of Doctor of Philosophy.

Paul H Holloway

Paul H. Holloway
Professor of Materials Science
and Engineering

I certify that I have read this study and that in my opinion it conforms to acceptable standards of scholarly presentation and is fully adequate in scope and quality, as a dissertation for the degree of Doctor of Philosophy.

Robert T. DeHoff

Robert T. DeHoff
Professor of Materials Science
and Engineering

I certify that I have read this study and that in my opinion it conforms to acceptable standards of scholarly presentation and is fully adequate in scope and quality, as a dissertation for the degree of Doctor of Philosophy.

Chris Batich for Reed-Hill
Robert E. Reed-Hill
Professor of Materials Science
and Engineering

I certify that I have read this study and that in my opinion it conforms to acceptable standards of scholarly presentation and is fully adequate in scope and quality, as a dissertation for the degree of Doctor of Philosophy.

Gerhard M Schmid
Gerhard M. Schmid
Associate Professor of Chemistry

This dissertation was submitted to the Graduate Faculty of the College of Engineering and to the Graduate School, and was accepted as partial fulfillment of the requirements for the degree of Doctor of Philosophy.

December 1983

Herbert A Bevis
Dean, College of Engineering

Dean for Graduate Studies and
Research